Machine Learning Algorithms for Multi-objective Design Optimization of Switched Reluctance Motors (SRMs)

MACHINE LEARNING ALGORITHMS FOR MULTI-OBJECTIVE DESIGN OPTIMIZATION OF SWITCHED RELUCTANCE MOTORS (SRMs)

BY

MOHAMED OMAR, B.Sc., M.Sc.

A THESIS

SUBMITTED TO THE DEPARTMENT OF ELECTRICAL & COMPUTER ENGINEERING

AND THE SCHOOL OF GRADUATE STUDIES

OF MCMASTER UNIVERSITY

IN PARTIAL FULFILLMENT OF THE REQUIREMENTS

FOR THE DEGREE OF

DOCTOR OF PHILOSOPHY

Doctor of Philosophy (2024) McMaster University

(Electrical & Computer Engineering) Hamilton, Ontario, Canada

TITLE: Machine Learning Algorithms for Multi-objective Design Optimization of Switched Reluctance Motors (SRMs)

AUTHOR: Mohamed Omar

M.Sc.

Electrical Engineering

Cairo University, Giza, Egypt

SUPERVISORS: Dr. Mohamed Bakr and Dr. Ali Emadi

NUMBER OF PAGES: xxiii, 153

To my Parents, Wife, and Family

Abstract

Switched Reluctance Motors (SRMs) are gaining recognition due to their robust design, cost-effectiveness, fault tolerance, and reliable high-speed performance, positioning them as promising alternatives to traditional electric motors. However, SRMs face high torque ripples, vibration, acoustic noise, and nonlinear modeling complexities. Through careful geometry design optimization, these drawbacks can be mitigated. Design optimization for SRMs is a multi-objective and nonlinear problem that requires an accurate finite element analysis (FEA) model to relate designable parameters to output objectives. The geometric design process follows a multi-stage and iterative approach, leading to prohibitive computational time until the optimal design is reached.

Machine learning algorithms (MLAs) have recently acquired attention in electric machine design. This study introduces an extensive analysis of various MLAs applied to SRM modeling and design. Additionally, it presents a robust framework for a comprehensive evaluation of these MLAs, facilitating the selection of the optimal machine learning topology for SRM design. Existing research on the geometry optimization of SRMs using MLAs has focused only on the machine's static characteristics.

This thesis introduces an advanced optimization method utilizing an MLA to act as a surrogate model for both static and dynamic characteristics of the SRM. The dynamic model incorporates conduction angles optimization to enhance the torque profile. The proposed MLA is applied to map out the SRM geometrical parameters, stator and rotor pole arc angles and their dynamic performance metrics, such as average torque and torque ripples. The optimal design improves the average torque and significantly reduces the torque ripples.

Radial forces constitute a critical objective that should be considered alongside average torque, efficiency, and torque ripple in the design optimization of SRMs. Accurate modeling of radial forces is a prerequisite for optimizing motor geometry to mitigate their adverse effects on vibrations and acoustic noise. This work presents an MLA-based surrogate model for the most influential radial force harmonic components, facilitating the integration of radial force reduction into a multi-objective optimization framework.

The proposed optimization framework employs two MLA-based surrogate models: the first correlates SRM pole arc angles with average torque and torque ripples, while the second models the most significant radial force harmonics. A genetic algorithm leverages these surrogate models to predict new geometrical parameters that enhance the SRM's torque profile and reduce radial forces. The optimization framework significantly reduced torque ripples and radial forces while slightly increasing average torque. The optimal design candidates were verified using FEA and MATLAB simulations, confirming the effectiveness of the proposed method, which offers significant computational time savings compared to traditional FEA techniques.

Acknowledgements

First and foremost, I would like to express my sincere gratitude to my supervisors, Dr. Mohamed Bakr and Dr. Ali Emadi, for their invaluable guidance, support, and mentorship throughout this research. Their knowledge, feedback, and encouragement have been instrumental in shaping this thesis and fostering my growth as a researcher. I am deeply grateful to Dr. Bakr for the countless hours spent in discussions and constructive comments that helped refine my work continuously. I also extend my appreciation to Dr. Emadi for the opportunity to be part of his leading research programs on transportation electrification. His professional character and dedication to work have been inspiring.

I would also like to express my sincere gratitude to the esteemed members of my supervisory committee, Dr. Berker Bilgin and Dr. Jennifer Bauman, for their valuable contributions and insights. Dr. Bauman's comments and guidance have aligned me with high-quality research standards, while Dr. Bilgin's suggestions have broadened my perspectives and strengthened my research.

My gratitude extends to the industry-sponsored project team members, especially Dr. Alan Callegaro and Dr. Giorgio Pietrini, for their visionary leadership and support. I also thank team members Dr. John Ramoul, Dr. Haomin Li, Kyle Kozielski, Dr. Yizhi Zhang, Korawege Nimesh, David Gyasi, Bridget Marfo, and Linke Zhou for the insightful discussions and shared experiences.

I am sincerely grateful to Dr. Ehab Sayed and Dr. Mohamed Abdalmagid for their mentorship and feedback and to my colleagues Parsa Beheshti, Rachit Pradhan, Dr. Mohamed Ibrahim, and Dr. Omar Zayed for their support and enriching my experience.

I would also like to extend my deepest gratitude to my mother, Ragaa Omar, and my father, Samir Omar, as well as my brothers and sister, for their unwavering love and support. A special thanks to my wife, Gehad Omar, who has been a constant source of strength and support during the ups and downs of this journey. Of course, I cannot forget to mention my lovely children, Ziad, Laila, and Sarah, who have been the source of inspiration and motivation throughout this endeavor.

Above all, I believe that everything I have achieved so far and will achieve throughout my life is due to Allah's help and guidance.

This research was undertaken, in part, thanks to funding from the Canada Research Chair in Transportation Electrification and Smart Mobility, and the Natural Sciences and Engineering Research Council of Canada (NSERC). I also gratefully acknowledge Powersys Solutions for their support of JMAG software in this research.

Nomenclature

Abbreviations:

2D	Two-Dimensional
3D	Three-Dimensional
ABC	Artificial Bee Colony
AI	Artificial Intelligence
ANFIS	Adaptive Neuro-Fuzzy Inference System
ANN	Artificial Neural Network
BEM	Boundary Element Method
BPNN	Backpropagation Neural Network
CNN	Convolutional Neural Network
CV	Cross-Validation
DE	Differential Evolution
FEA	Finite Element Analysis
FFT	Fast Fourier Transform
FNN	Feedforward Neural Network
FOA	Fruit Fly Optimization Algorithm
GA	Genetic Algorithm

GDA	Gradient Descent Algorithm
GDS	Grid Diamond Search
GRNN	Generalized Regression Neural Network
IM	Induction Machine
KKT	Karush-Kuhn-Tucker
LM	Levenberg Marquardt
LSSVM	Least Square Support Vector Machine
LUT	Look-up Tables
LWSQR	Locally Weighted Smoothing Quadratic Regression
MAE	Mean Absolute Error
MEC	Magnetic Equivalent Circuit
MLA	Machine Learning Algorithm
MLP	Multilayer Perceptron
MRE	Mean Relative Error
MSE	Mean Squared Error
PMSM	Permanent Magnet Synchronous Motor
PSO	Particle Swarm Optimization
R	Linear Regression Correlation Coefficient
RBF	Radial Basis Function
RBFNN	Radial Basis Function Neural Network
RELU	Rectified Linear Unit

RNN	Recurrent Neural Network
RMSE	Root Mean Square Error
SSE	Sum Squared Error
SRM	Switched Reluctance Motor
SM	Space Mapping
SVR	Support Vector Regression
SVM	Support Vector Machine
Tanh	Hyperbolic Tangent

Symbols:

b	Bias
B_t	Tangential Component of The Flux Density
B_r	Radial Component of The Flux Density
C	Kernel Regularization
D_1	Diode 1
D_s	Stator Outer Diameter
D_{sh}	Shaft Diameter
E_b	Back EMF
F_d	Radial Force Density
$f_{f(u,v)}$	Forcing Frequency of Radial Force Harmonic

f_{mech}	Mechanical Frequency of Rotor
f_{obj}	Objective Function
$g(z)$	Activation Function
H	Hessian Matrix
h_r	Rotor Pole Height
h_s	Stator Pole Height
i	Phase Current
I_m	Magnetization Current
I_{ph}	Instantaneous Phase Current
I_{ref}	Peak Reference Current
I_{RMS}	Phase RMS Current
k	Discrete Step
L	Inductance
L_g	Air Gap Length
L_{st}	Stack Length
m	Number of Phases
N_r	Number of Rotor Poles
N_s	Number of Stator Poles
P_g	Air Gap Power
R	Phase Resistance
RPM	Machine Base Speed

S_1	Power Switch 1
T	Complete Electrical Period
t	Time
T_{avg}	Average Torque
T_e	Electromagnetic Torque
T_s	Sampling Time
$T(\theta)$	Instantaneous Phase Torque
u	Stator Radial Force Temporal Order
v	Stator Radial Force Circumferential Order
V	Phase Voltage
Vdc	DC-Link Voltage
W	Neurons Weight
W_c	Co-Energy
X	Input Vector
y	Labelled Output
y_s	Stator Back Iron Thickness
y_r	Rotor Back Iron Thickness
ΔT_{RMS}	RMS Value of The Torque Ripple
β_s	Stator Pole Arc Angle
β_r	Rotor Pole Arc Angle
τ_s	Stator Taper Angle

τ_r	Rotor Taper Angle
θ	Position of Rotor
θ_{elec}	Electrical Angle
θ_{on}	Turn-on Conduction Angle
θ_{off}	Turn-off Conduction Angle
σ^2	Kernel Width
σ_i	Feature Width of RBF
$\varphi(X)$	Kernel Function
λ	Flux Linkage
ω	Rotational Speed
μ_o	Air Permeability

Contents

List of Tables

List of Figures

Chapter 1

Introduction

1.1 Background and Motivation

Switched reluctance motors (SRMs) are gaining popularity due to their uncomplicated and robust structure, which does not include any magnets or windings in the rotor [1]. The absence of permanent magnets and rotor windings enables the SRM to operate efficiently at high temperatures and speeds [2]. This design feature also results in a lighter rotor, leading to a higher torque-to-inertia ratio and improved dynamic performance as compared to induction machines (IMs) and permanent magnet synchronous motors (PMSMs) [3]. Furthermore, the SRM's lack of rare-earth material makes it a cost-effective alternative to PMSMs. The volatile prices and supply challenges of permanent magnets have prompted researchers to explore the application of SRMs in various industrial fields, including HVAC systems [4], renewable power systems [5], and electrified transportation [6].

However, SRMs face challenges such as significant torque ripples, acoustic noise, and vibrations due to their salient pole configuration [7]. The acoustic noise primarily originates from radial forces exerted on the stator poles [8], while torque ripples predominantly result from harmonics of the rotor tangential force. Effectively addressing these challenges involves optimizing the SRM's geometrical design and control parameters.

The process of designing electric machines entails the fine-tuning of machine parameters, typically accomplished through a combination of experience and heuristic approaches. This often involves using finite element analysis (FEA) software to simulate the effects of different parameter adjustments [9]. However, this approach does not ensure the attainment of the optimal design [10]. Additionally, utilizing a time step FEA within an optimization procedure for electric machines results in prohibitive execution time [11],[12].

Generally, the conventional design process for the electromagnetic aspect of SRMs is an iterative and multi-stage process. Initially, a static analysis using FEA is conducted to create look-up tables that map the characteristics of flux linkage and static torque with respect to various rotor positions and currents. Subsequently, dynamic analysis is conducted via MATLAB simulations using the generated look-up tables. The optimization of conduction angles is then performed for each geometry design candidate to enhance the dynamic performance. This process is repeated until an optimal design is achieved [9], resulting in a significant execution time for both static (FEA) and dynamic (MATLAB) analyses [13].

Developing an accurate surrogate model to replace FEA simulations would significantly save repetitive effort and execution time [13]. Recently, Machine Learning algorithms (MLAs) have gained significant attention in the field of motor design due to their ability to learn from data and generate accurate predictions. MLAs excel in modeling the nonlinear relationships between the geometrical machine parameters and the machine performance. In [14], a generalized regression neural network (GRNN) was developed to optimize the pole arc angles of 12/8 SRM. An FEA model was implemented to analyze the static characteristics, and the GRNN was utilized as a surrogate model to represent these static characteristics [14]. In [15], another study introduced the utilization of GRNN for modeling a 12/8 SRM. The aim was to capture the nonlinear correlations between motor performance against rotor yoke and pole arc angles. Notably, these studies relied solely on sample data derived from FEA static analysis, ignoring the effect of the control and dynamic analyses on enhancing motor performance.

Additionally, the MLAs employed in motor design have primarily focused on enhancing the average torque and mitigating torque ripples. However, in the case of SRMs, addressing acoustic noise and vibrations is imperative to establish them as a robust alternative to conventional motors. These undesirable effects predominantly originate from radial forces acting on the stator. Modeling these radial forces is complicated and necessitates heavy time-consuming FEA and dynamic analysis simulations. Therefore, developing a surrogate model for radial forces is crucial to establishing an efficient multi-objective optimization framework for SRM enhancement.

1.2 Novelty and Contributions

The objective of this research is to introduce an efficient approach for multi-objective design optimization of SRMs utilizing MLAs. Initially, a static FEA model was constructed to capture the static characteristics of the 6/14 SRM while varying pole arc angles. These static properties were then utilized to develop a dynamic Simulink model aimed at optimizing conduction angles to enhance motor torque. Subsequently, the outputs from the FEA model and the dynamic model were employed to construct the first surrogate model, which represents the average torque and RMS value of torque ripples in response to adjustments in geometrical parameters. Additionally, we utilized the developed FEA and Simulink models to characterize the radial force density acting on the stator. These calculated radial forces, alongside changes in various geometrical parameters, were employed to develop another MLA-based surrogate model. Finally, a genetic algorithm was applied to utilize both MLA surrogate models in the search for optimal SRM performance. The main contributions of this research are outlined as follows:

1. A review of MLAs applied to the modeling and design of SRMs.
2. Introduction of a new approach using MLA to develop a surrogate model for both static and dynamic characteristics of SRMs. The dynamic characteristics incorporate the optimization of conduction angles at each variation of geometric parameters, specifically pole arc angles.
3. Development of a framework for effective MLA selection and evaluation.

4. Improvement of average torque and minimization of torque ripples for the considered 6/14 SRM using the developed approach.
5. Introduction of a new approach using MLA-based surrogate model for modeling the most influential radial force density components, simplifying their integration into the geometry optimization process.
6. Introduction of a multi-objective optimization framework to search for the optimal SRM geometrical parameters that enhance torque profile and reduce the most significant radial forces density components.

Mechanical design, vibrations, and acoustic noise will not be addressed in this thesis.

1.3 Outline

Chapter 2 introduces the fundamental principles of SRMs and explores key electromagnetic characteristics, including flux linkage, electromagnetic torque, and stored energy. Furthermore, the Chapter provides a concise overview of the operational and control principles of SRMs.

Chapter 3 reviews various numerical and analytical techniques used for modeling SRMs. It then categorizes the MLAs into their main types. Finally, the Chapter presents a comprehensive review of the MLAs employed in the electromagnetic modeling of SRMs and discusses their application in geometry optimization to enhance motor performance.

Chapter 4 introduces a framework for effective MLA selection and evaluation, conducting a comprehensive comparison of supervised machine learning algorithms applied to SRM design to choose the optimal MLA for the thesis.

Chapter 5 utilizes the optimal MLAs developed in Chapter 4 to improve the torque profile of the 6/14 SRM. This MLA is employed as a surrogate model to map out the relationship between the SRM pole arc angles and motor performance, resulting in increased average torque and minimized torque ripples.

Chapter 6 presents a novel method using MLA to model the radial force density components. This approach is crucial for reducing the most influential radial force components acting on the stator, a key objective of this thesis.

Chapter 7 proposes a multi-objective optimization algorithm utilizing the MLA-based surrogate models developed in Chapter 5 and Chapter 6 to optimize the geometrical parameters of the considered 6/14 SRM. A genetic optimization algorithm is employed to search for the SRM design candidate that minimizes torque ripples and the most influential radial force density harmonics without decreasing the average torque.

Finally, **Chapter 8** provides a summary and conclusion of the thesis's work and outlines potential future research.

Chapter 2

Switched Reluctance Motors (SRMs): Fundamentals and Operating Principles

2.1 Key Features and Challenges of SRMs

Switched reluctance motors (SRMs) feature a simple and robust construction. The stator and rotor consist of a stack of laminated ferromagnetic material. The stator has concentrated windings. The rotor does not have permanent magnets or windings. This makes SRMs easier and less expensive to manufacture with a secure and stable supply chain [16]. Besides, they can run at high temperatures. The SRM phases require independent excitation, which enables programming of the shape of the phase current for performance improvement and fault tolerance capability of the motor drive [17].

On the other hand, the double saliency structure of SRMs brings some challenges, such as high torque ripples and windage losses, especially at high-speed operation. Depending on how the motor is designed and controlled, SRMs might also suffer from lower power density and torque density compared to PMSMs [18]. Acoustic noise and vibration are the most well-known challenges in SRMs. Another primary concern is the complexity of modeling SRMs because of their highly nonlinear characteristics. Also, the need for uncommon converters to drive this motor is another challenge. However, much research has been conducted to tackle these issues and improve motor performance [19]- [22].

2.2 Operating Principles of SRMs

The structure of a switched reluctance motor is double salient. It consists of a stator and rotor featuring salient poles. The number of stator and rotor teeth defines the number of phases and torque pulsations. They also dictate the motor configuration and the operational characteristics of the motor. Fig. 2.1 shows a typical structure of a three-phase 12/8 SRM. There are eight rotor poles and twelve stator poles in this motor arrangement.

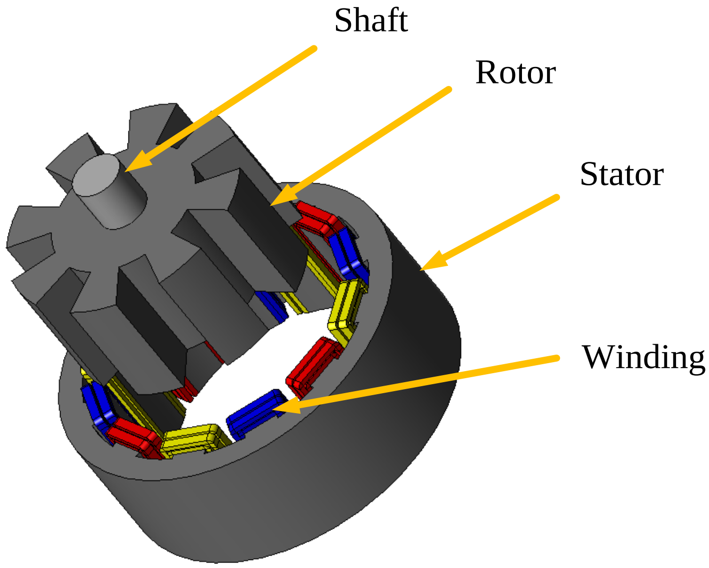

Fig. 2. 1. A typical structure of a three-phase 12/8 SRM.

The stator teeth are surrounded by concentrated coils, also known as short-pitched coils. Due to these concentrated windings, the number of coils in SRMs matches the number of stator teeth. These coils within a phase can be linked in series, parallel, or a combination of both, according to the stator pole count. Balanced torque is achieved in each phase when stator poles with identical electrical positions are equally distributed across the stator. Continuous torque production is maintained by having a phase shift between the electrical angles of stator poles from various phases.

Similar to the torque characteristics, the flux linkage of the SRM depends on the position of the rotor. An ideal flux linkage profile with respect to rotor position is shown in Fig. 2.2 for one electrical cycle. There are three central regions based on the rotor position: aligned, partial-overlap and unaligned [23]. The SRM rotor pole overlaps the energized stator pole at the aligned position, as depicted in Fig. 2.3 (a). In contrast, there is no overlap between the stator and rotor poles in the unaligned position, as depicted in Fig. 2.3 (b). At the unaligned positions, the relative distance between the stator and rotor poles is the largest. Thus, the resulting air gap is the largest, and flux linkage is the lowest. In contrast, flux linkage is the highest at the aligned position.

The profile of the phase inductance follows an identical pattern to the flux linkage. The inductance rises as the rotor pole moves from unaligned to aligned. It should be indicated that as the phase current increases, the flux linkage increases. Fig. 2.4. shows the flux linkage profiles versus the current at three different rotor positions. At high current levels, the rate of change of flux linkage decreases due to the saturation of the magnetic core [1]. To achieve high torque density, SRMs work in saturation regions [24]. Thus, phase flux linkage exhibits a nonlinear relationship with stator phase current and rotor position [23], [24]. In addition, the airgap periphery is inconsistently distributed due to the salient construction of the stator and rotor poles. These reasons make modeling of SRMs challenging.

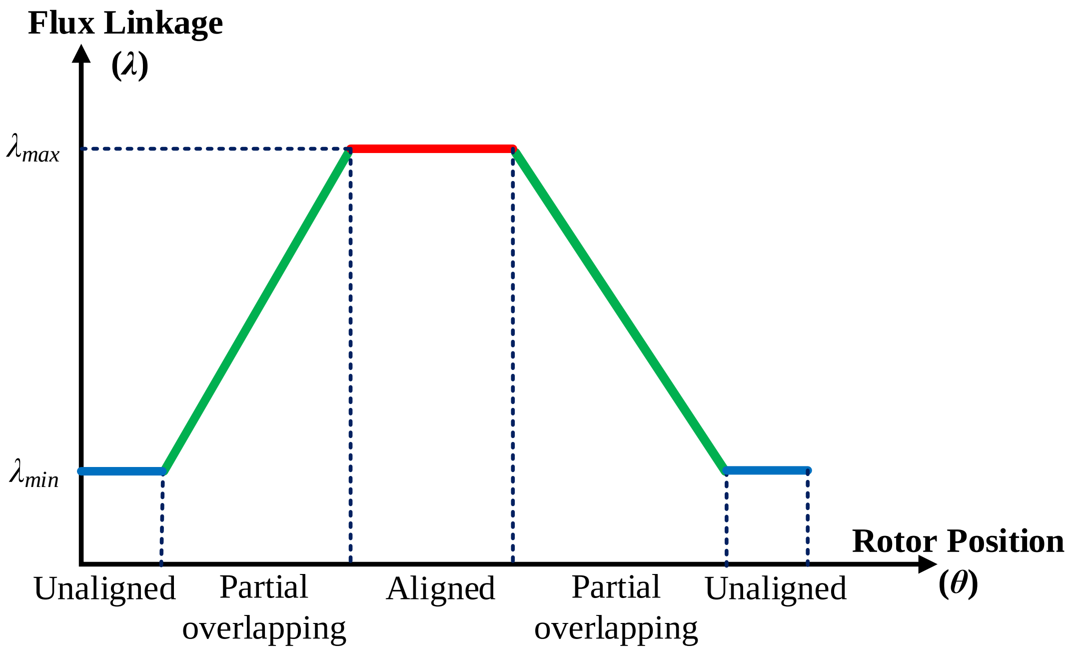

Fig. 2. 2. Ideal profile of flux linkage versus rotor position.

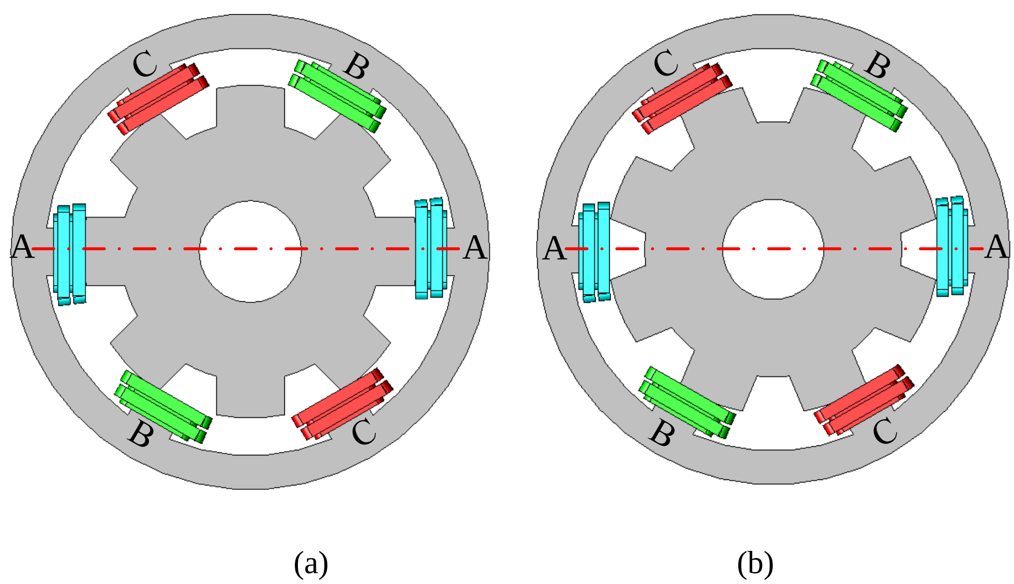

Fig. 2. 3. Ideal SRM rotor positions with respect to phase A shown on an 6/8 SRM (a) aligned position and (b) unaligned position.

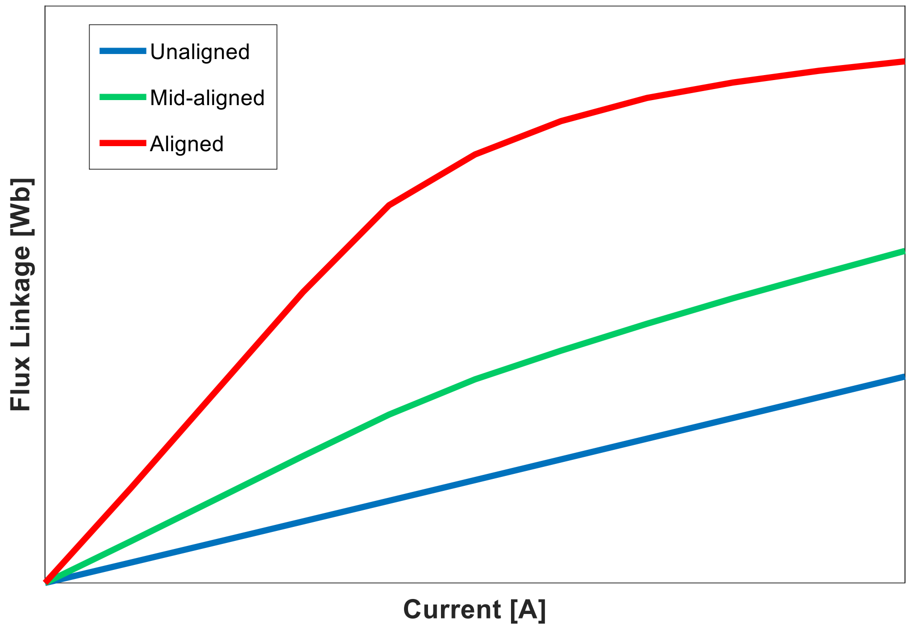

Fig. 2. 4. The flux linkage profiles versus phase current at three different rotor positions.

2.3 Modeling of SRMs and Equivalent Circuit

As mentioned in the previous section, the inductance, L changes with the position of the rotor and the current. Therefore, the flux linkage, λ can be expressed as a function of the position of the rotor, θ and coil current, i,:

$$\lambda = L(\theta, i)i \tag{2.1}$$

The SRM voltage equation, neglecting mutual coupling between phases and based on Faraday's law, is expressed as follows [25]-[27]:

$$V = iR + \frac{d\lambda(\theta, i)}{dt} \tag{2.2}$$

where V and R are the phase voltage and phase resistance, respectively. By substituting equation (2.1) into equation (2.2), the phase voltage can be expressed as:

$$V = iR + \frac{d(L(\theta,i)i)}{dt} \tag{2.3}$$

Expanding the phase voltage equation using the chain rule, we have:

$$V = iR + L(\theta,i)\frac{di}{dt} + i\frac{dL(\theta,i)}{d\theta}\frac{d\theta}{dt} \tag{2.4}$$

The rotational speed can be utilized in equation (2.4) to represent the position and time.

$$V = iR + L(\theta,i)\frac{di}{dt} + i\frac{dL(\theta,i)}{d\theta}\omega \tag{2.5}$$

The last term in equation (3.5) represents the back EMF of the machine, signifying the power of the airgap that will be converted to the machine's mechanical power. The terminal voltage of the SRM can thus be rewritten as:

$$V = iR + L(\theta,i)\frac{di}{dt} + E_b \tag{2.6}$$

Therefore, the equivalent circuit of an SRM per phase can be visualized as depicted in Fig. 2.5.

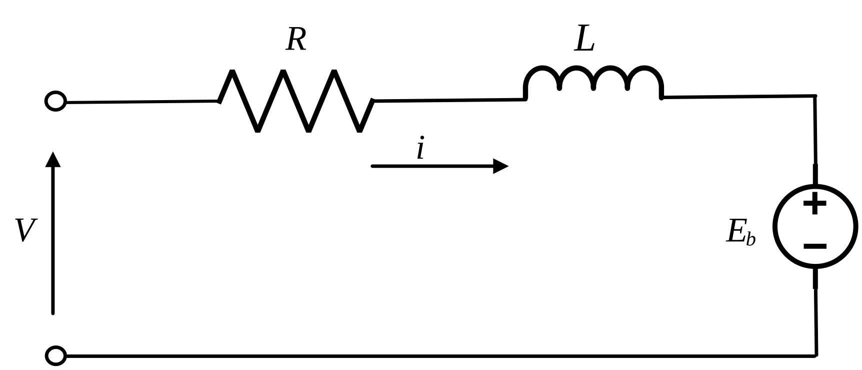

Fig. 2. 5. Equivalent circuit of an SRM per phase.

The magnetic energy stored in the airgap is defined as the magnetic field energy, graphically represented by the area above the flux-current relationship. Co-energy, on the other hand, is the complement of the magnetic energy stored in the machine airgap, represented by the area under the curve of the flux-current characteristics. Fig. 2.6 illustrates the magnetic field energy and co-energy in terms of the flux linkage and current. The formula for the co-energy W_c at constant current can be defined as:

$$W_c = \frac{1}{2} L(\theta) i^2 \tag{2.7}$$

The electromagnetic torque is directly proportional to the rate of change of co-energy at different rotor positions:

$$T_e = \left.\frac{\partial W_c}{\partial \theta}\right|_{i=constant} = \frac{1}{2}\frac{dL(\theta)}{d\theta} i^2 \tag{2.8}$$

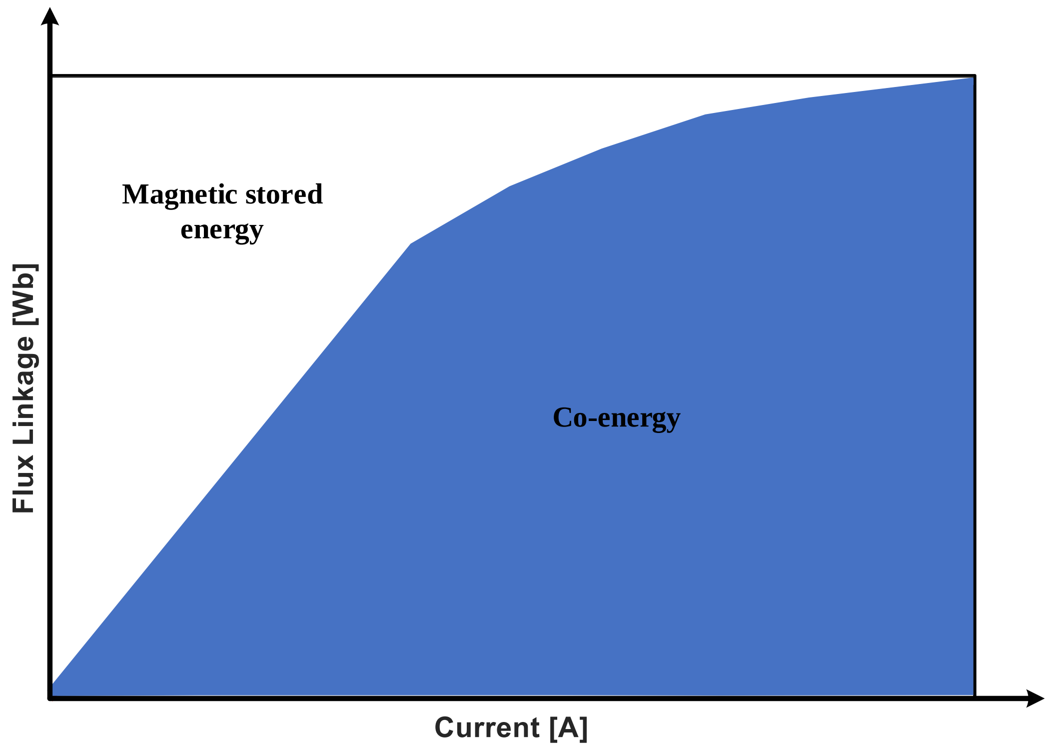

Fig. 2. 6. A graphical representation of magnetic field co-energy and stored energy of an SRM.

To calculate the instantaneous power, we multiply the voltage equation presented in equation (3.5) by the corresponding current, as demonstrated below:

$$Vi = i^2R + iL(\theta,i)\frac{di}{dt} + i^2\frac{dL(\theta,i)}{d\theta}\omega \tag{2.9}$$

Simplifying this instantaneous power equation yields:

$$Vi = i^2R + \frac{d}{dt}(\frac{1}{2}i^2L(\theta,i) + \frac{1}{2}i^2\frac{dL(\theta,i)}{d\theta}\omega \tag{2.10}$$

Finally, the air gap power, P_g can be deduced as:

$$P_g = \frac{1}{2}i^2\frac{dL(\theta,i)}{d\theta}\omega \tag{2.11}$$

It is evident from equations (2.8) and (2.11) that both the air gap power and the torque are functions of the phase current and rate of change of inductance with respect to the rotor position.

2.4 Control of SRMs

The switched reluctance motor phases are excited by the rotation of the rotor teeth, ensuring continuous torque generation. The power converter required to excite these phases and control the conduction angles for each phase is an asymmetric bridge converter. The term "asymmetric" is derived from its configuration, which consists of two diagonal switches and diodes, as illustrated in Fig. 2.7. In this figure, three asymmetric bridge converters are employed to control a three-phase SRM, with each phase having its dedicated power converter. This arrangement is necessary because the phases in SRMs are electrically isolated.

The electrical isolation of SRM phases enhances the machine's fault tolerance capability. If one phase fails, the remaining phases can still operate, allowing for continued operation with reduced performance. Another advantage is that the mutual coupling of the magnetic flux can be neglected when one phase is triggered, as the magnetic flux linking to other phases is minimal. This benefit can significantly reduce the simulation time required for the FEA static analysis of SRMs, which will be explored in the upcoming Chapters.

A crucial aspect of current control in SRMs is that these asymmetric converters produce a unidirectional current flow. This characteristic is advantageous because the torque generated by an SRM is proportional to the square of the phase current, and therefore, it is not affected by the direction of the current. Consequently, the unidirectional current flow simplifies the control strategy and ensures efficient torque production [28]-[29].

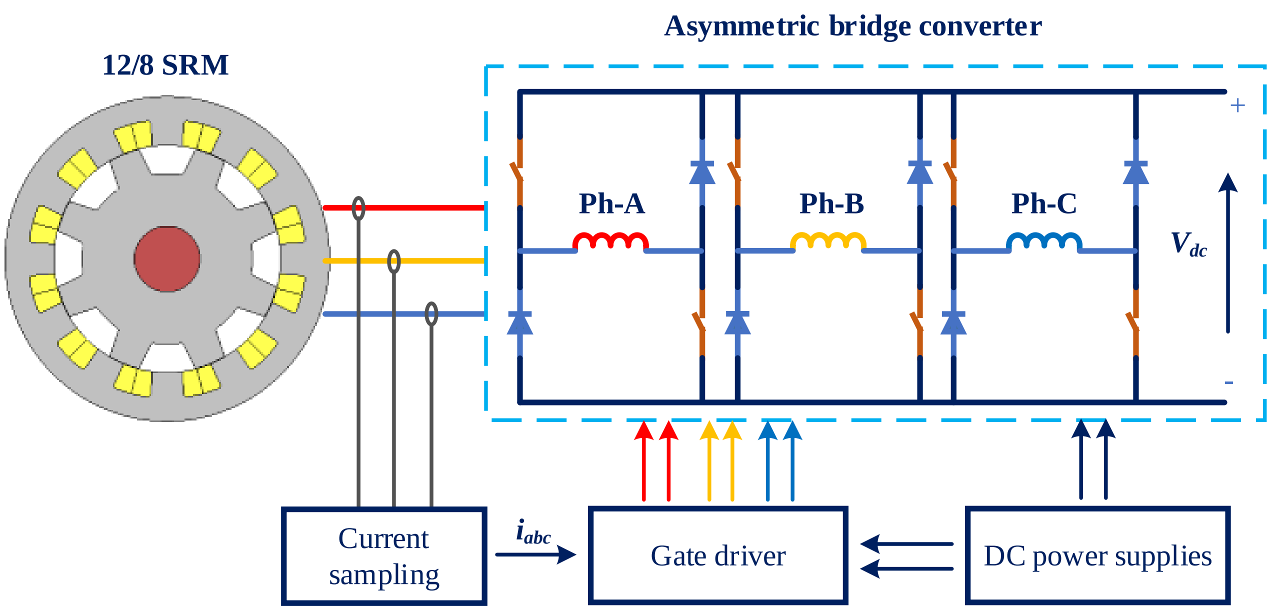

Fig. 2. 7. A schematic diagram of a three-phase asymmetric bridge converter controlling a 12/8 SRM.

Depending on the control approach, the asymmetric bridge converter employs various switching states to regulate the phase current in SRMs. There are three main modes of operation. As shown in Fig. 2.8(a), the first operating mode occurs when both controllable switches are turned on. The voltage across the phase windings equals the DC-link voltage, leading to an increase in the phase current.

In the second operating mode, illustrated in Fig. 2.8(b), both controllable switches are turned off. Under these conditions, both diodes become actively biased, resulting in the voltage across the phase winding becoming the negative DC-link voltage. This causes the current in the coils to decrease until it reaches zero.

The third operating mode, known as the freewheeling mode, is depicted in Fig. 2.8(c). In this mode, one switch and one diode are active. There is no energy transfer back to the DC-link, and the current decreases at a slower rate compared to the previous switching mode due to the coil's internal resistance.

The asymmetric bridge converter facilitates these three switching states, enabling precise control over the phase current, thereby enhancing the overall performance and efficiency of the SRM drive system. Once both controllable switches are turned on and the current reaches the predefined reference value, the freewheeling mode is activated during the conduction period. This mode regulates the phase current, preventing it from exceeding the reference value. If the current decreases below the reference current by a specific hysteresis threshold, the first operating mode (illustrated in Fig. 2.8(a)) is reactivated by turning both switches on, consequently increasing the current. This cyclical process, known as the hysteresis control, is repeated to maintain the SRM phase current within a narrow band around the reference value, ensuring optimal torque production and minimizing torque ripple. Finally, the second operating mode (Fig. 2.8(b)) is activated to demagnetize the phase winding rapidly.

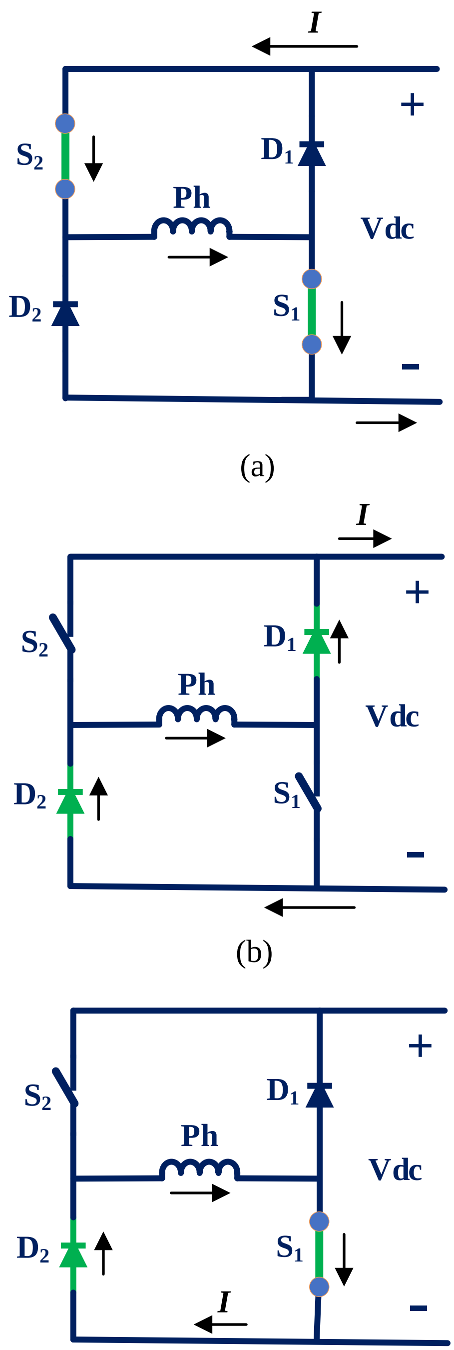

Fig. 2. 8. Different operating modes for a per-phase asymmetric bridge converter: (a) both controllable switches are on, (b) both controllable switches are off, and (c) freewheeling mode.

Chapter 3

Overview of Machine Learning Algorithms for Modeling and Design of SRMs

Switched reluctance motors (SRMs) are receiving more attention owing to their simple and robust construction, low cost, and fault tolerance capability. SRMs also offer reliable performance and stable operation at high speeds [30], [31]. These advantages make SRMs a promising alternative to conventional electric motors, such as induction motors and permanent magnet synchronous motors (PMSMs). The challenges in SRMs are the high torque ripples, vibration, acoustic noise, and high-level nonlinearity in modeling.

However, extensive research has been conducted to address those issues. SRMs have recently been used in many applications, such as propulsion, machinery, mining, pumps, and domestic appliances [1],[32].

Each application of SRMs requires a set of specific requirements. For example, electric machines in EVs and HEVs should have high torque and power densities, a wide operating speed range, and high efficiency at different operating conditions [33], [34]. Design optimization of SRMs helps significantly in fulfilling these requirements. Design optimization is a multi-objective and nonlinear problem [35]. The design optimization process requires an accurate electromagnetic model that relates the designable parameters to the output objectives [36], [37]. The machine model provides various electromagnetic characteristics such as induced electromotive force, flux density and electromagnetic torque. It also helps calculate the machine losses and assesses its performance.

Several nonlinear modeling techniques were developed in the literature. These techniques can be categorized as numerical and analytical techniques. Numerical modeling methods include the finite element analysis (FEA) and the boundary element method (BEM). FEA is a widely adopted numerical modeling technique [38], [39]. Although FEA provides accurate results, it is computationally expensive [40]. On the other hand, the BEM approach has attracted interest in electromagnetic analysis due to its high accuracy and reduced computational burden compared to FEA [41].

Analytical techniques derive approximate analytical relationships between the designable parameters of the machine and the performance characteristics [42], [43]. The most known analytical modeling methods are based on curve fitting, Maxwell's equations, and magnetic equivalent circuit techniques. Unlike numerical methods, analytical approaches are much less expensive computationally [44]. However, the key challenges of analytical methods are modeling core saturation and end-winding inductance and calculating eddy current and hysteresis losses [45].

Machine Learning Algorithms (MLAs)-based modeling methods are classified as curve fitting techniques. They became more popular due to the emergence of many advanced Artificial Intelligence (AI) algorithms. They offer a good generalization capability for modeling nonlinear characteristics. MLAs-based modeling techniques provide good accuracy at a reasonable computational cost. This Chapter presents a comprehensive literature review of the various techniques applied in modeling and designing SRMs. It emphasizes the use of MLAs in SRM modeling and design, which is the central focus of this thesis.

3.1 Modeling Techniques for SRMs

Undoubtedly, the accurate electromagnetic modeling of SRMs is the basis for design optimization, performance prediction, and current control. Numerous studies have focused on modeling the electromagnetic characteristics of SRMs. These approaches are commonly classified into two main categories: numerical and analytical methods. Fig. 3.1 summarizes the most common modeling methods for SRMs.

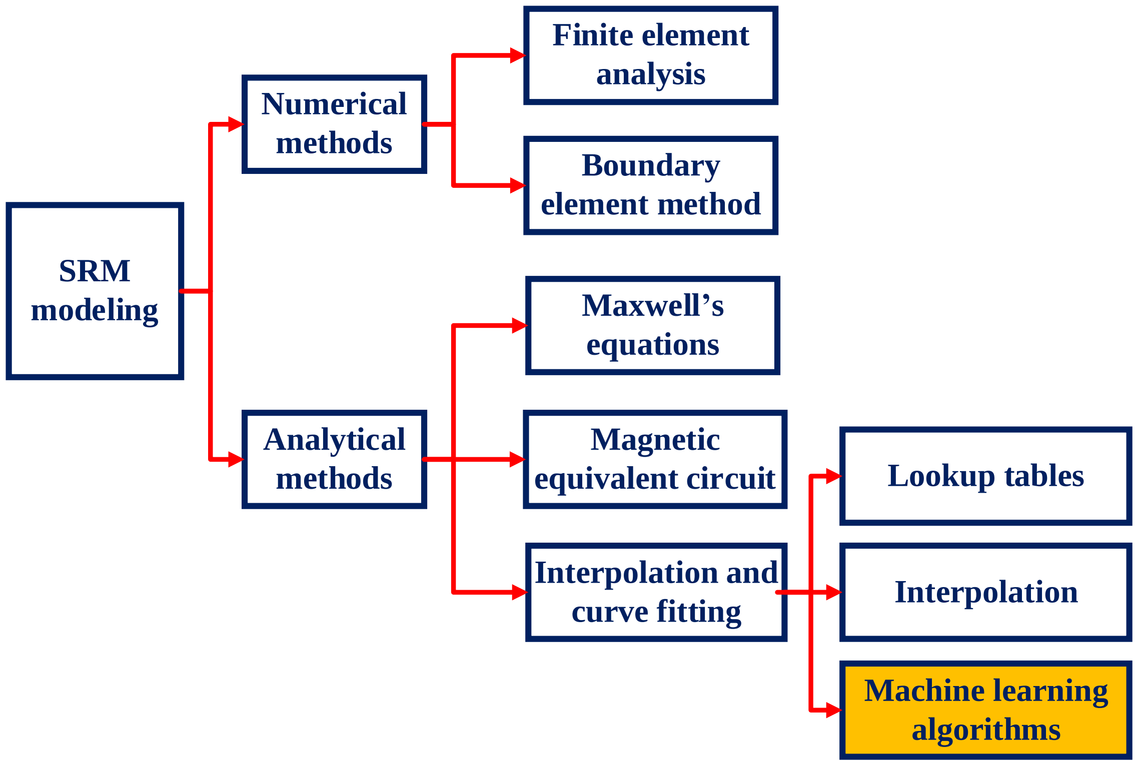

Fig. 3. 1. Classification of various modeling techniques for SRMs.

3.1.1 Numerical Modeling Methods:

Numerical modeling methods utilized in SRM modeling include FEA and boundary element method (BEM) [46], [47]. FEA is the most common numerical technique. It provides an electromagnetic analysis with high accuracy for motor geometrical parameters. It does not require the assumptions considered in analytical methods [24]. The FEA modeling accuracy is highly dependent on the number of finite elements [48]. Since SRMs commonly operate in the saturated region, a large number of finite elements is required to promote model accuracy [49]. In addition, the airgap of SRMs varies with the rotor operation. This requires a fine mesh close to the airgap. The key disadvantage of FEA modeling is the high computational cost, as one FEA simulation time might extend to hours depending on the model complexity and how fine the utilized mesh is.

BEM is an alternative technique to FEA. It solves the magnetic fields on the boundary domain using the boundary integral equations. It usually requires less computational effort, and its accuracy can be as high as the FEA [50]. However, BEM's main shortcoming is the difficulty of analyzing and solving saturated magnetic fields [46]. To tackle this issue, BEM is usually combined with another modeling method, such as FEA or magnetic equivalent circuit (MEC), to model SRMs [50], [51]. FEA or MEC is used to solve for the electromagnetic fields in the saturated nonlinear regions, while BEM analyzes fields in the linear region.

3.1.2 Analytical Modeling Methods:

Maxwell’s equations, magnetic equivalent circuit (MEC), and curve fitting techniques are the most common analytical modeling methods. Maxwell’s equations-based models ignore the local saturation, mutual coupling effect, and leakage flux, thus limiting the model's accuracy [49]. It is commonly preferred in preliminary design stages to determine main design parameters [52], [53].

The MEC method is powerful in analyzing and designing electric motors. It develops magnetic circuits for considered machines to study magnetic characteristics. The MEC method utilizes fewer elements than numerical methods and results in smaller system matrix dimensionality. This provides a significant computation speed [24]. Unlike the Maxwell-based method, the MEC method can be improved to consider the magnetic saturation and leakage flux to achieve a closer accuracy with respect to FEA [38]. The magnetic flux path of MEC structures for SRMs should be modified with rotor position. This can be addressed by using empirical formulas or assumptions for the flux paths at various rotor positions based on preceding experience gained from FEA simulations. However, that restricts the generality and accuracy of this method [24].

Curve-fitting models utilize lookup tables, interpolation techniques, or machine learning algorithms to approximate phase flux linkage variation with respect to rotor position and stator current [49]. This is achieved based on limited data captured from FEA simulations or experiments.

The look-up table-based method is easy to implement with reasonable accuracy. FEA simulations are used to capture flux linkage, induced voltage, and torque characteristics with respect to various stator phase currents and rotor positions. These data are then stored in 2-D (or 3-D when mutual coupling between phases is considered) look-up tables. Then, a dynamic model for the considered SRM is developed, solving the time-domain differential equation for the phase current based on the look-up tables. Interpolation is applied to obtain the torque as a function of the rotor position and calculated phase current [54], [55].

Interpolation modeling techniques are used to approximate the nonlinear relationship between the flux linkage or inductance and the phase current by piecewise interpolation functions. For instance, a 2-D bicubic spline and quadratic interpolation function are adopted in [56] and [57] to analyze the magnetic performance of SRMs.

MLAs are used to express the nonlinear nature of the flux linkage, inductance, and torque regarding the SRM phase current and rotor position. The learning algorithms use training datasets acquired through numerical simulations or experiments. The advantage of MLAs is that they can predict SRM flux and torque profiles based on limited data. Thus, MLAs reduce the computational efforts required for conventional numerical methods [24]. In addition, these techniques are able to adapt to the variation in motor parameters due to losses and manufacturing tolerances [58].

3.2 Classification of Machine Learning Algorithms

Artificial Intelligence (AI) is a prosperous field with multiple practical applications and active research subjects. Machine Learning (ML) is the capability of AI systems to derive patterns from raw data to acquire knowledge. ML comprises computational methods that rely on available past information to enhance performance or get accurate predictions. This past information or sample data should be collected carefully since its quality and size are essential for predicting an accurate output [59]. MLAs can provide solutions for many applications, such as computer vision, speech recognition, robotics, biology, and medical diagnosis [59]. MLAs can be classified into supervised, unsupervised, and reinforcement learning [60]. These learning types differ in the sample data and its collection and evaluation.

Supervised learning algorithms are the most utilized MLAs. They learn from the available examples (training data) provided by a knowledgeable supervisor. The training data is composed of a set of labelled examples of the input vector and the corresponding output target vector [59]. After training the model, some examples that were not used in the training process are used to test the model's generalization ability. The difference between the predicted and the actual target values determines the prediction error. Fig. 3.2 illustrates the basic schematic of supervised learning techniques.

Supervised learning algorithms are used to address regression and classification problems [59]. Classification is one of the standard learning tasks. Digit and image recognition are examples of classification problems where definite discrete categories are assigned for each input item. The number of categories differs according to the classification problem. Regression is the prediction of a real output value corresponding to a given input vector. An excellent example that explains the difference between the classification and the regression is the weather temperature forecast. A regression model predicts the weather temperature in values such as 20°C. The classification predicts whether the weather is hot or cold. Another regression example related to this work is predicting the torque of an SRM based on the considered motor’s flux linkage and current.

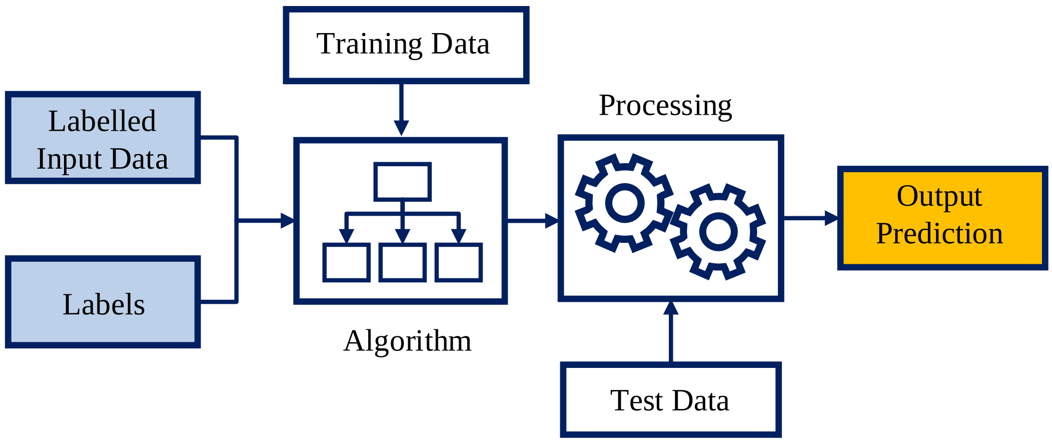

Fig. 3. 2. The basic flow chart of supervised learning techniques.

In unsupervised learning, the sample data comprises unlabeled examples containing input data without any target vector values [59]. Thus, there is no guide or instructor in this type, and the developed algorithm should learn to use the available data effectively without a guide. Unsupervised learning algorithm can observe the data features. It then attempts to predict the dataset structure, which is known as the probability distribution in the context of machine learning. It can also combine sets of similar examples into homogeneous subsets, known as clustering [59]. A famous clustering example is dividing uncategorized data of two different animals, such as dogs and cats, into two separate clusters. Fig. 3.3 shows the structure of unsupervised learning techniques. The system does not have any prior knowledge about the features and does not have any dataset for training. The algorithm task is to distinguish the features of the dataset on its own and perform clustering into subsets.

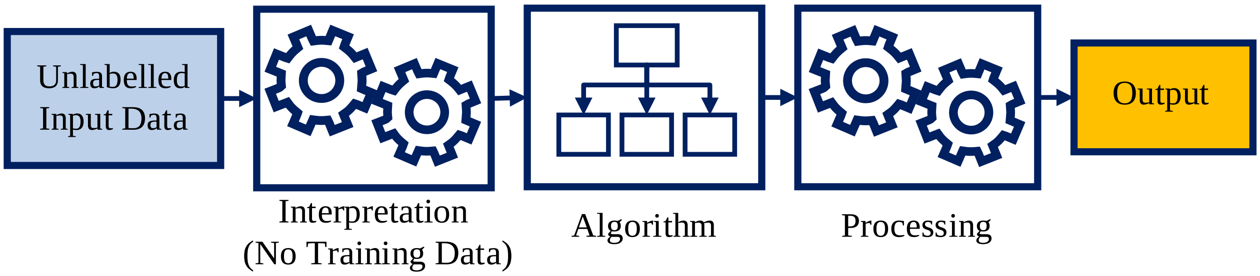

Fig. 3. 3. The basic flow chart of unsupervised learning techniques.

Reinforcement Learning does not have available training examples. Instead, a trial-and-error approach is used to define the training examples. The reinforcement learning approach interacts with the system (simulation model) by receiving observed states and selecting appropriate actions. In response to each control action, the algorithm accepts a feedback signal (reward) taken in each situation [61], as shown in Fig. 3.4. The reward differentiates between the good and bad action results and defines the objective of the reinforcement learning algorithm. The algorithm tends to maximize the reward over a set of iterations and actions with the system [60].

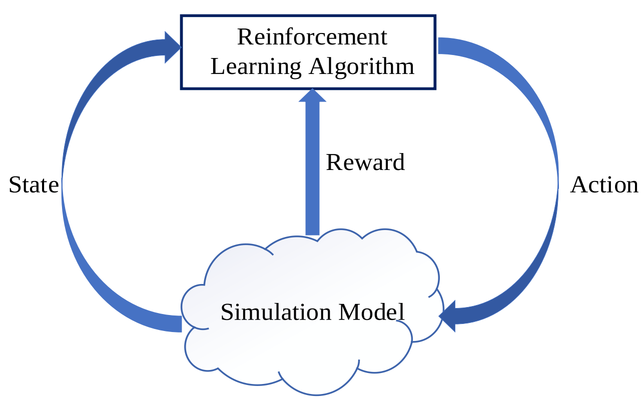

Fig. 3. 4. The basic flow chart of reinforcement learning technique.

3.3 Machine Learning-Based Algorithms for Modeling SRMs

This section presents relevant published work on modeling SRMs using MLAs. Several algorithms are used for modeling SRMs to accomplish fast computation and accurate results. Almost all machine learning techniques used in this context are supervised learning algorithms. These algorithms include feedforward neural networks (FNN), recurrent neural networks (RNN), adaptive neuro-fuzzy inference systems (ANFIS), and support vector machine (SVM).

3.3.1 Feedforward Neural Network (FNN)

Artificial neural networks (ANNs) have evolved rapidly in recent years due to their capability of learning and generalizing complex relationships, ease of implementation, and fast real-time operation. FNNs form the basis of several important commercial and industrial applications [62]. An FNN is a mathematical model that approximates functions by mapping features and labels. Features are the attributes associated with each given example. They are defined as the input vector to the learning algorithm. The accurate selection of the features is critical to achieving adequate performance results. This is typically done by the user based on prior knowledge of the learning problem [59]. Labels are the predicted outputs of the algorithm. The label can be a value for a regression problem or a category for a classification task.

Fig. 3.5 illustrates the basic structure of an FNN with one hidden layer. The information passes forward through the layers of the network. The input vector, X provides initial data, which propagates forward to the computational hidden neurons and finally produces the label y. The hidden neurons calculate a weighted sum of the features with an added bias b as illustrated in (3.1). This sum then triggers an element-wise nonlinear activation function $g(z)$. Typically, the hidden neurons are only distinguished from each other by the selection of the type of activation function.

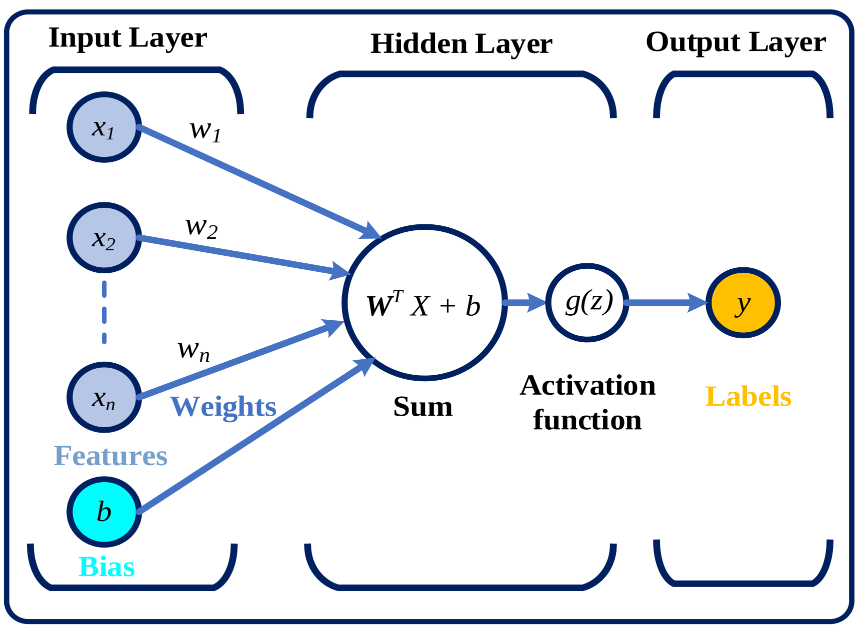

Fig. 3. 5. The basic structure of FNN with one hidden layer.

$$z = W^T X + b \tag{3.1}$$

$$g(z)=\begin{Bmatrix} \max\{0,z\} & \text{- RELU} \\ \dfrac{1}{1+e^{-z}} & \text{- Sigmoid} \\ \dfrac{e^{z}-e^{-z}}{e^{z}+e^{-z}} & \text{- Tanh} \\ \dfrac{1-e^{-2z}}{1+e^{-z}} & \text{- Tansig} \end{Bmatrix}. \tag{3.2}$$

A recommended default choice for most FNN applications is the rectified linear units (RELU) expressed in (5) [62]. Applying RELU to a linear transformation output produces a nonlinear transformation. The RELU function is a piecewise linear function composed of two linear segments. Therefore, it enables gradient-based optimization and generalization of linear models [62]. Before introducing the RELU activation function, most ANNs used Sigmoid, Hyperbolic Tangent (Tanh), and Tansig functions [62]. These activation functions are expressed in (3.2). These functions saturate at minimum function output for low stimulus values. They also saturate at maximum output for high stimulus values. They increase monotonically for the values in between the minimum and maximum outputs as the neuron stimulus increases [63].

The neural network's training process aims at estimating the optimal set of weights, W and optimal bias that would achieve the best function approximation. The learning algorithm usually involves an iterative procedure to minimize a loss (error or cost) function, which is used to estimate the algorithm's performance. The loss function is the measurement of the distance between the actual and predicted target response. The prediction error increases as the measured distance increases [62]. The model mean squared error (MSE) is typically used as a loss function to measure the model performance in regression tasks. The MLA is then evaluated using a test dataset. The test dataset has not been used during the training process. The main objective of the test dataset is to ensure that the algorithm can generalize the mapping to new input-output pairs.

Due to the FNN's ability to approximate any nonlinear mapping with a certain degree of accuracy, it maintains a high research interest, especially for the multilayer perceptron (MLP) and radial basis function (RBF) networks. MLP is a fully connected FNN which contains one or more hidden layers. The RBF networks are comprised of only a single hidden layer. Backpropagation learning algorithms enable MLP networks to be trained [64]. The following subsections overview the recent literature on using backpropagation neural networks (BPNN) and RBF neural networks in electric motor modeling.

3.4.1.1 Backpropagation Neural Networks (BPNN)

The backpropagation term describes the training methodology of MLP networks. Standard backpropagation applies gradient descent to the sum-squared error function through two stages. The derivatives of the loss function are evaluated with respect to the neurons' weights. These derivatives are propagated backward through ANN layers. Then, in the second stage, the weights are adjusted based on the evaluated derivatives [60]. The shortcoming of using gradient descent is its slow convergence. In most cases, the gradient descent algorithm (GDA) follows a zigzag pattern to reach an optimal solution, so it might not meet the fast training network requirements [63] [65]. Other gradient-based algorithms can be used to train ANNs, such as conjugate gradient, which searches for an optimal solution along a sequence of conjugate directions. It overcomes issue the GDA has and shows a faster convergence [63]. However, the step size should be adjusted for each iteration, which leads to a computational overhead [65].

Newton's method provides faster convergence than GDA and conjugate gradient approaches. Therefore, it is more favourable, but the high computational cost of calculating the Hessian matrix, H, (second-order derivatives) is the main concern. Moreover, it does not guarantee a local minimum convergence, especially if the initial point is far from the optimal solution [63]. The quasi-Newton method approximates H with the first-order derivatives. However, it uses a large memory to save the approximate matrix at each training iteration [65].

The Levenberg Marquardt (LM) algorithm tackles the issues with Newton’s method. When the sum squared error function is used as a cost function, LM does not require calculating the Hessian matrix. Instead, it uses a Jacobian-based approximation matrix. Generally, LM tends to finish the learning stage in fewer epochs than other discussed algorithms. The number of epochs reflects the number of the total complete passes through the training dataset. It can often be adjusted to hundreds or thousands to allow the learning approach to run until the error is minimized to a sufficient value. Moreover, LM guarantees local minimum convergence. It is evident that Quasi-Newton and LM provide faster convergence at the expense of more memory requirements. LM offers better overall performance as it combines the merits of gradient descent and Newton methods [65]. It is worth noting that the discussed gradient-based approaches obtain a local minimum, which is the global minimum for convex functions. The problem arises if the function is non-convex since it could possibly have multiple local minima [62], [63].

In [66], BPNN was used for modeling a 12/8 1.5-kW SRM. The network structure has one input layer for the two input variables: targeted average torque and rotor position. The BPNN contains two hidden layers with 12 neurons, and each neuron utilizes the Hyperbolic Tansig function. However, the output layer utilizes a linear activation function to estimate the output current. An experimental setup was built to collect the training dataset of the torque versus the rotor position at different current levels. The generalization of the learning algorithm is evaluated using a test dataset that was not used during the learning process. The authors in [66] utilized many numerical optimization algorithms for the network training, such as Quasi-Newton, conjugate gradient, and LM. LM achieved the fastest and the most accurate learning results. The error between the actual (measured) and the predicted output phase current using the LM algorithm was less than 0.1 A.

A BPNN was also applied in [67] to model an 8/6 SRM. The learning phase of the ANN utilizes 496 measured magnetization data samples. The structure of the BPNN consisted of a single input layer for the current and flux linkage, a single hidden layer, and a single output layer to estimate the rotor position. The activation function chosen for the hidden layer was a sigmoid, and the output layer was linear. LM managed to finish the training in only 22 epochs with the minimum error compared to conjugate gradient and quasi-Newton algorithms.

The authors in [41] developed real-time modeling of phase inductance and flux linkage of a 4.1-kW 8/6 SRM using FNN. Unlike [67], which used a static locked-rotor test to obtain the magnetic motor characteristics, this work applied dynamic measurements to achieve an online learning algorithm. The learning process was performed using the

BPNN algorithm to optimize the network weights. The network structure is comprised of one input layer assigned for the measured current and rotor position, two hidden layers, and a single output layer to estimate the flux linkage, as depicted in Fig. 3.6. A Gaussian function was utilized as an activation function for both hidden and output layers. The proposed model was validated experimentally. However, as discussed earlier, GDA was applied to train the ANN and optimize the weights, which has a slow convergence.

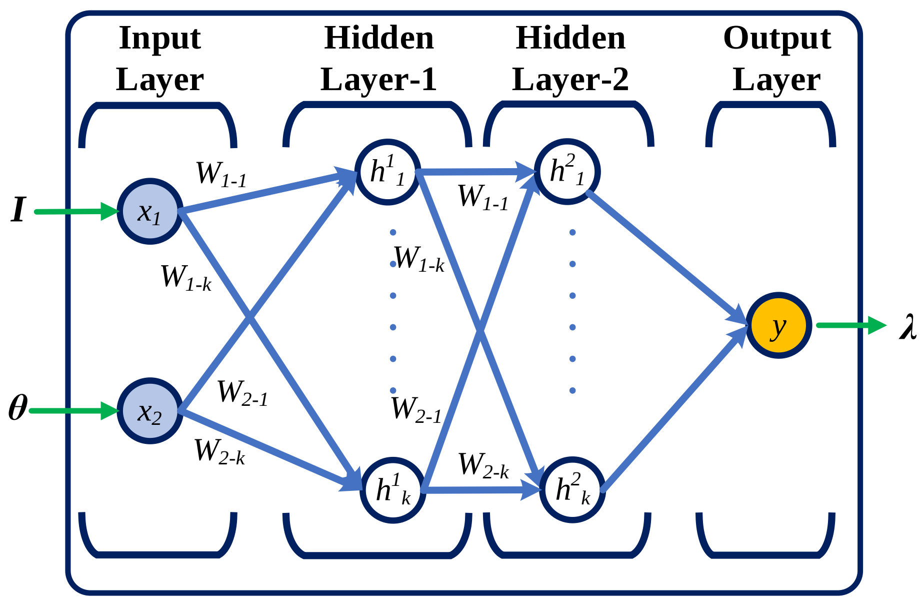

Fig. 3. 6. The basic structure of FNN with two hidden layers.

In [68], two cascaded single-output BPNNs were used for modeling an 8/6 SRM. The first BPNN was used to model the current $i(\lambda,\theta)$ and the second for the torque $T(i,\theta)$. The authors used FEA to obtain the dataset. The variation ranges of phase current and rotor position angle used to get the dataset are [0A – 20A] and [0° – 30°], respectively. The chosen step size was 1A for the current and 1° for the rotor position. The training dataset uses even rotor position angles, whereas the test dataset uses the odd ones. The structures of the two BPNNs were similar: a single input layer for the inputs, two hidden layers, and a single output layer. The total number of hidden neurons to estimate the current and the torque is 10 and 8, respectively. The activation function of the hidden layer was a hyperbolic Tansig, whereas that of the output layer was a linear function.

In [68], LM was utilized as an optimization algorithm for training the network. The mean square error was acted as a loss function for performance evaluation, and the target error was set to 0.0001. The simulation results showed that the generalization capability of the cascaded BPNN models is high. However, the training process took longer time than that in [67]. In [68], It took about 1000 epochs for modeling the current and more than 600 epochs for modeling the torque; however, it took only 22 epochs for modeling the rotor position in [67]. An 8/6 SRM was modelled in both works. That significant difference might be because of the dataset size and the target error used to terminate the learning phase. In fact, the training error, gap between training and test errors, and sample data size should be selected carefully to avoid overfitting and underfitting problems [61]. Overfitting and underfitting are common problems associated with learning in ANNs. Overfitting means the model is complex and does not optimally fit the new data. It arises when the gap between test and training errors is too large, leading to a significant generalization error. In contrast, underfitting refers to a model that is incapable of fitting the training data with a sufficiently low error value.

The authors in [69] used an FNN to form an efficient mapping for the nonlinear characteristics of an 11.5-kW 6/4 SRM. The current and flux linkage are the inputs to the

FNN, and the output is the estimated rotor position, as illustrated in Fig. 3.7. In [69], a single-layer FNN with ten hidden neurons was proposed to obtain a good balance between the estimated error and the ANN complexity. The hidden layer neurons use sigmoidal activation functions, whereas the output layer utilizes linear transfer function. A test dataset was used to assess the performance and the generalization capability of the learning algorithm. This methodology introduced an initial approach for a sensorless position estimation for SRM control.

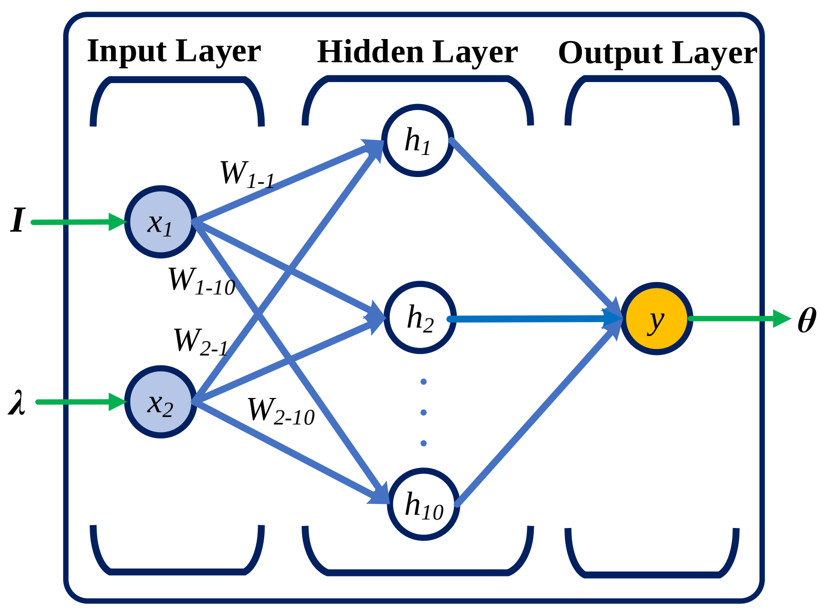

Fig. 3. 7. The basic structure of a single-layer FNN with ten hidden nodes to model a 6/4 SRM [69].

In [70], a BPNN was applied to model the magnetic nonlinearity of SRMs. The flux linkage of the SRM and the position are the inputs to the ANN, whereas the current is the ANN output. Two hidden layers were utilized with hyperbolic tangent transfer functions.

The learning algorithm was developed using GDA to adjust the network weights and minimize the error arising from the difference between the actual and predicted outputs. The training dataset was collected experimentally to train the ANN more accurately and efficiently. The training strategy starts with a few hidden neurons. Then, the number of neurons is increased while monitoring the network's generalization capability after each epoch. The generalization capability was evaluated through the testing dataset. The optimal number of hidden neurons was found to be 8 for each hidden layer. The total number of training epochs was 2000. The training results using the BPNN showed great agreement with the experimental outcomes.

3.4.1.2 Radial Basis Function Neural Network (RBFNN)

The structure of the radial basis function neural network (RBFNN) has only a single hidden layer, as depicted in Fig. 3.8. The RBFNN is considered as a linear function approximator that uses RBFs for its features. Typically, the RBF feature holds a Gaussian response which depends only on the i^{th} measurement of the distance between the central state, and the state, X relative to the feature width, σ_i [65]:

$$F_i(X) = e^{-\frac{\|X - c_i\|^2}{2\sigma_i^2}} \quad . \tag{3.3}$$

Some learning techniques for RBFNN include adjusting the centers of the features and the widths of the Gaussian distribution. The most outstanding merit of RBFNN is that it provides the best approximation along with fast convergence. However, the number of hidden neurons is more critical than that used in BPNN [65]. The computational complexity is the downside of RBF networks, especially for nonlinear RBF networks [61]. At the start of the training process, the number of hidden neurons is zero, and it increases gradually until the error difference between the actual and estimated output reaches the target error, or the number of the neurons reaches a prespecified limit.

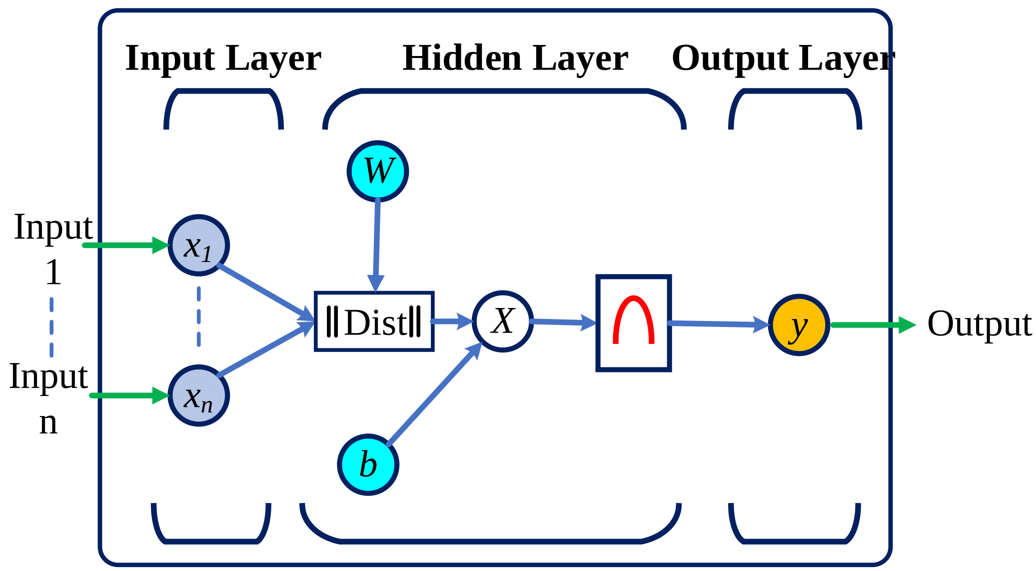

Fig. 3. 8. A simplified example of RBFNN structure.

An RBFNN was used in [71] to model the magnetic characteristics of an 8/6 SRM. A set of experimentally measured data for the flux linkage at various stator currents and rotor positions was used for training. The proposed RBFNN is comprised of two inputs for the current and rotor position, six hidden neurons, and one output layer to estimate the flux linkage. The number of epochs for the network training is 100. The simulation outcomes of the proposed RBFNN showed a good match with the experimental training data.

However, the authors did not test the generalization ability of the proposed RBFNN using a separate test dataset.

In [65], the authors used an RBFNN and BPNN for modeling a 1.5-kW 12/8 SRM and compared both neural networks. The training dataset was acquired using experimental measurements. The inputs of both neural networks are the flux linkage and stator current, whereas the network output is the position. The structure of the BPNN had a single hidden layer with a Tansig activation function. An LM optimization algorithm was implemented for learning BPNN. The recorded error of the BPNN output (rotor position) was 1.51° when using five hidden neurons. The error increases as the number of neurons decreases. For RBFNN, the optimum number of hidden neurons was 69, and the maximum rotor position error was 2.07°. It is clear that the LM-BPNN showed better accuracy than the RBFNN for estimating the rotor position.

3.3.2 Recurrent Neural Network (RNN)

Unlike FNN, recurrent neural network (RNN) utilizes recurrent units that store past information data to handle a sequential input [58] [72]. A neural network is called recurrent when the output or an intermediate state is passed back to the input, thus allowing the use of past data, as shown in Fig. 3.9.

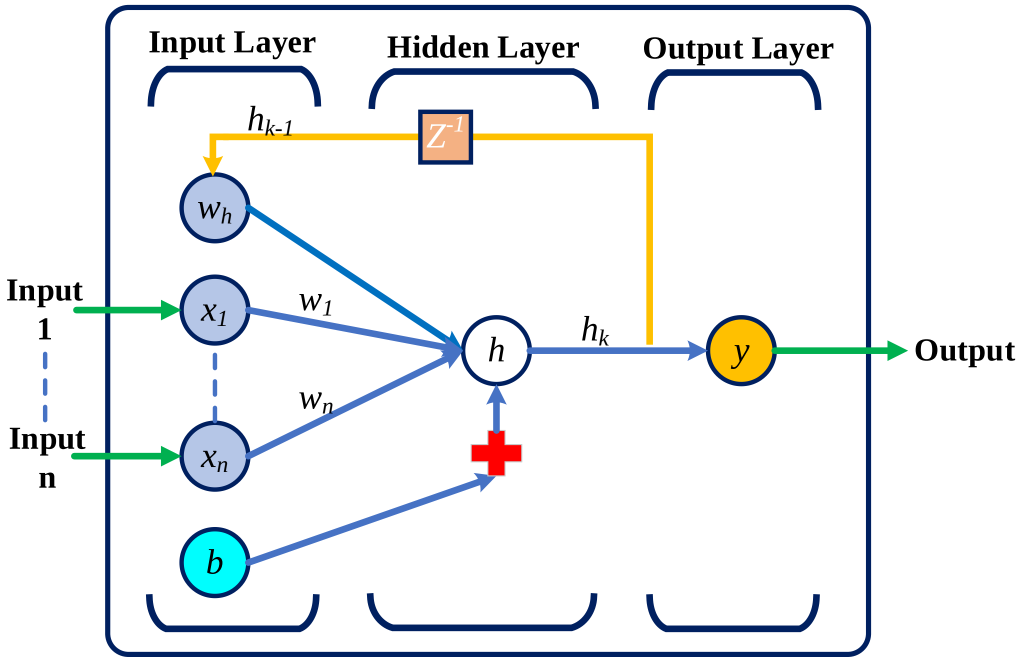

Fig. 3. 9. A basic structure of RNN.

The authors in [58] adopted a two-layer RNN for parameter identification of an 8/6 SRM. Since the SRM parameters may differ at a standstill from dynamic operation due to the losses and saturation, the authors added a parallel damper winding to the magnetization winding to improve the model accuracy. The RNN was adopted to estimate the damper and the magnetizing currents because both are highly nonlinear and not measurable. Besides phase current and rotor position, the phase voltage, v and speed, ω are assigned as inputs to the RNN to consider the motional back EMF. The outputs of the RNN are the magnetization current, I_m and the total phase current (used as a training objective), which are fed back again into the input layer to form RNN.

The chosen activation functions are Tansig for the hidden layer and pure linear for the output layer. After training the RNN using standstill data, the damper current was calculated by subtracting the estimated magnetizing current from the total phase current. The damper voltage was also calculated. As a result, the damper inductance and resistance were identified using the maximum likelihood estimation technique [73]. The proposed online model had been validated, and the results showed its estimation superiority over the standstill model. The average covariance of the phase currents for the online model was 0.6885, whereas that for the standstill model was 0.9127.

3.3.3 Adaptive Neuro-Fuzzy Inference Systems (ANFIS)

Adaptive neuro-fuzzy inference system (ANFIS) integrates the expert knowledge of fuzzy logic, represented in membership functions and if-then rules, with the ANN learning power. Thus, it combines the benefits of both FIS and ANN. The ANFIS aims to optimize the FIS parameters using the learning algorithm based on the training data sets. Like ANN, parameter optimization is finished when the error measured between the real and target output is minimized.

In [74], the authors applied an adaptive neuro-fuzzy inference system to identify the inductance of a 6/4 SRM. A hybrid learning technique that combines the backpropagation and least square method was utilized for rapidly training and adapting the fuzzy inference system. The inputs for ANFIS are the stator phase current and rotor position angle, whereas the output is the estimated phase inductance. A dataset of 552 samples is generated using FEA; 75% of these data are used for training and 25% for testing ANFIS. The current dataset is between 2A – 24A, whereas the rotor position range is from 0° – 45°. The number of training epochs is 100. The authors assigned 9 Gaussian membership functions for each current and rotor position. Thus, the number of rules is 81. The root mean square errors (RMSEs) for training and testing ANFIS were 1.914e-6 and 3.461e-6, respectively. Thereby, the ANFIS-based inductance profile was in good agreement with that of the FEA model. However, dynamic simulation and real-time validation need to be investigated. Additionally, a comparison between ANFIS and ANN should be added since the authors in [67] showed that the LM-based BPNN was more accurate than the ANFIS model. ANFIS usually has the potential to converge to a local minimum solution [75].

Another similar approach that uses ANFIS for modeling a 0.55-kW 1500-rpm 6/4 SRM was introduced in [76]. The authors employed ANFIS for modeling the considered SRM flux linkage $\psi(i,\theta)$ and torque $T(i,\theta)$ .The flux linkage characteristics were obtained experimentally, and the torque was calculated using the virtual displacement principle [76]. Data samples of 396 out of 512 datasets are used for training the network. The remaining sets were used for testing. The RMSE value at the end of the training process was 1.78e-3 Wb for the flux linkage and 0.022 Nm for the torque model. These values were reached after 100 epochs. After training ANFIS, the model accuracy was validated by comparing the flux linkage and torque with the corresponding measured data. The authors verified their proposed model by carrying out a dynamic simulation. Fig. 3.10 shows the block diagram of the SRM dynamic model to simulate its dynamic performance. The maximum deviation in the average torque between the measured and simulated results was less than 10%.

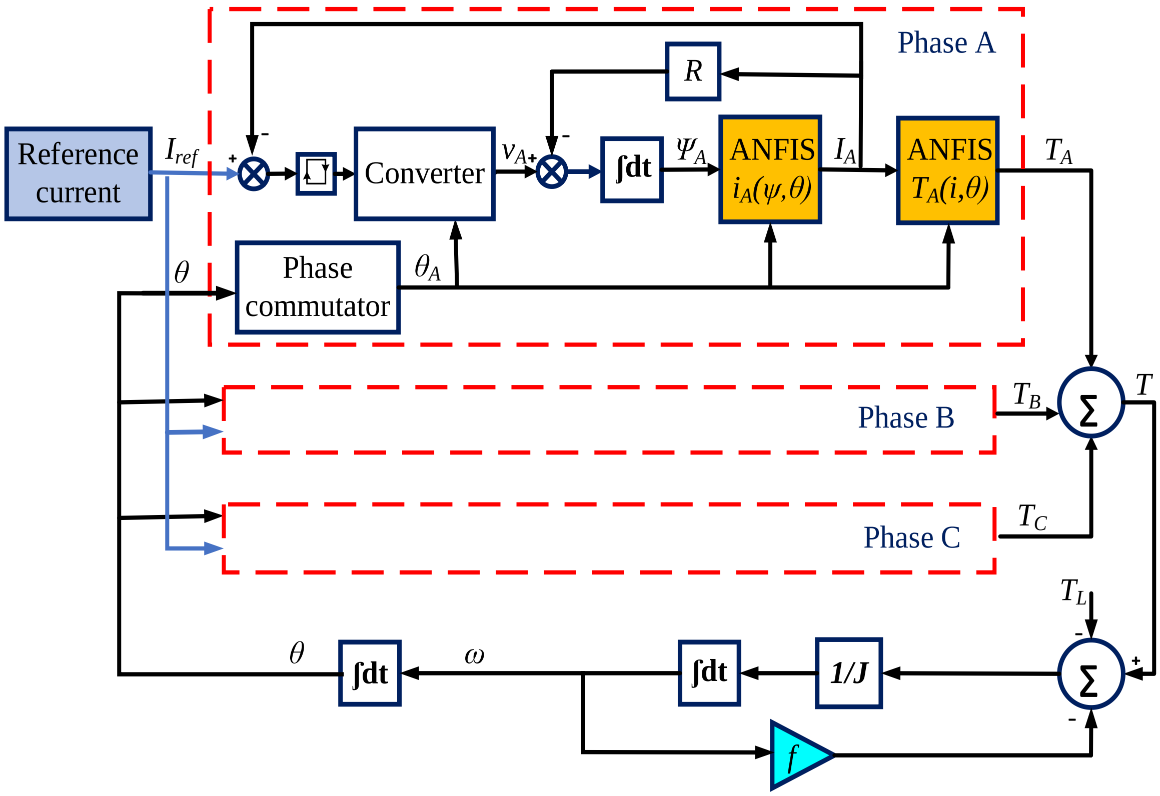

Fig. 3. 10. The simulation block diagram of a 3-phase SRM using ANFIS to model the torque and flux linkage characteristics [76].

3.3.4 Support Vector Machine (SVM)

A Support Vector Machine (SVM) is a class of supervised machine learning algorithms that was first presented as a classifier to achieve classification tasks [77]. The support vector network nonlinearly maps the input vectors to some high-dimensional feature space. SVM derivation is based on the theory of statistical learning. SVM can also be used for regression tasks; in this case, it is called a support vector regression (SVR). Fig. 3.11 (a) shows a schematic diagram of the SVM for the classification tasks. The blue line represents a separating hyperplane that differentiates between two different types of data

[78]. The red lines represent the marginal hyperplanes and the dark red circles located on these planes are called the support vectors. On the other hand, Fig. 3.11 (b) shows a schematic diagram of the SVM for the regression tasks, which can be used to forecast the data trends. The formula for separating hyperplane is [78]

$$f(X) = W^T \varphi(X) + b \tag{3.4}$$

where $\varphi(X)$ denotes the kernel functions that takes the input data X and maps it to high-dimensional solution space.

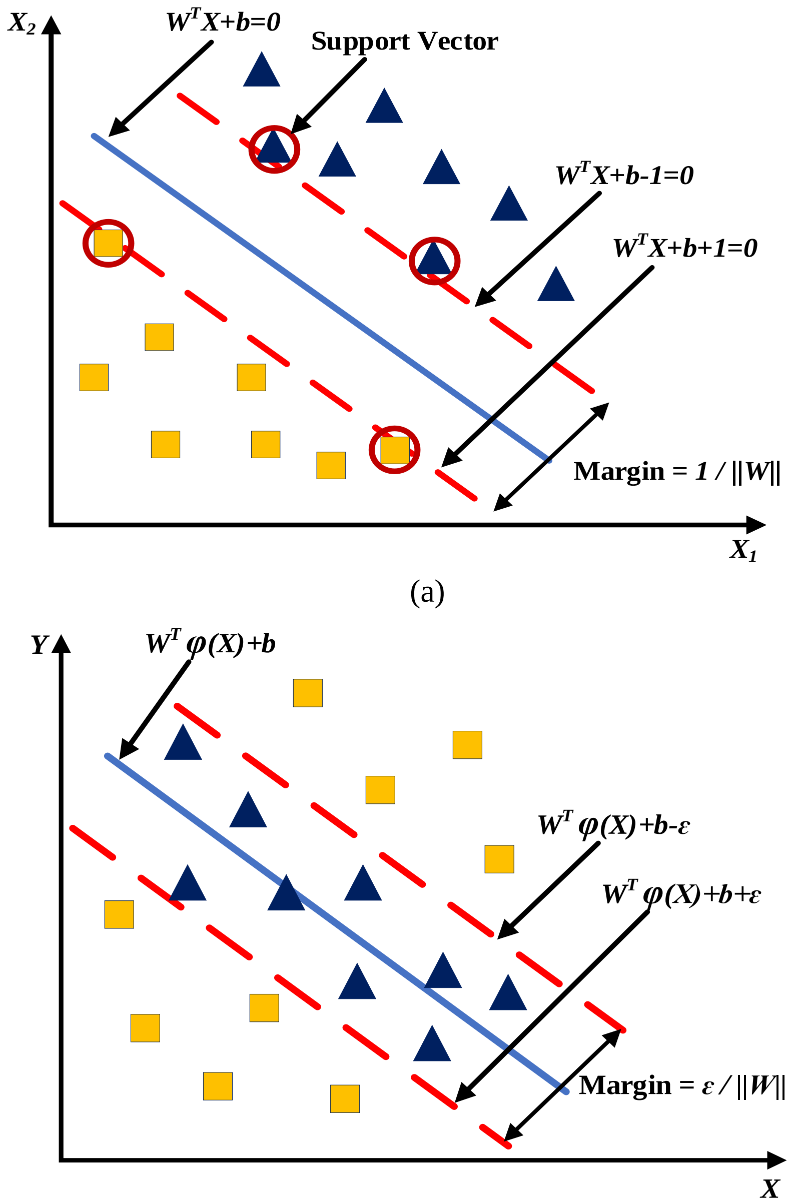

Fig. 3. 11. The schematic diagram of SVM separating and marginal hyperplanes for the (a) classification and (b) regression tasks. ε in (b) is the tolerable deviation between the hyperplane and the transformed data [78].

SVM has gained much popularity since it has overcome ANN problems such as dependency on the size and quality of the sample data, and the overfitting possibility. SVM has been successfully applied in fault diagnosis [79],[80], speech recognition [81], and data mining [82], [83]. In [84], a combined modeling method for a 1-kW 12/8 SRM using SVM and BPNN was introduced. The flux linkage characteristics were measured without rotor position sensors and clamp devices. Thus, only 64 samples are acquired, which are not sufficient for precise modeling. Therefore, the proposed algorithm in [84] consists of two main steps: data reconstruction and characteristic description. SVM was trained in the data reconstruction stage, using a few measured sample data to model the flux linkage characteristics. After that, two BPNNs were adopted in the description stage to model the SRM. One BPNN model is used to model the current $i(\psi,\theta)$ based on the reconstructed data. However, the other BPNN was used to model the torque $T(i,\theta)$ based on the calculated static torque characteristics.

The authors verified the proposed method's accuracy by carrying out dynamic simulation and comparing its results with those from experimental measurements. The discrepancy between the simulation and online estimation of the average torque is 5.7% [84]. The SVM succeeded in converting the flux linkage modeling problem with low-dimensional space to an optimization problem with a high-dimensional space.

SVM was also formulated to solve nonlinear equations using quadratic programming to avoid local minima solutions. However, this increases the computational burden. In [85], an alternative approach was demonstrated to replace inequality constraints with equality constraints and apply sum squared error (SSE) as a loss function. This approach is known as the least square support vector machine (LSSVM). This reformulation has significantly simplified the problem because the solution became identified by the Karush-

Kuhn-Tucker (KKT) linear system [85]. This system can be efficiently solved by utilizing an iterative approach such as the conjugate gradient algorithm. This simplicity makes the LSSVM algorithm faster than standard SVM with less computational time [83], [86]. Similar to SVM, LSSVM can be employed for regression and classification tasks, but its regression model accuracy relies on the values of the hyperparameters [87].

Kernel functions are used in LSSVM to map the input data to a higher-dimensional space. There are different kernel functions, such as sigmoid, polynomial, Gaussian, and RBF. The proper selection of the kernel type is essential because this choice affects the LSSVM performance. Moreover, the choice of the regularization, C and kernel width, σ^2 parameters determine the accuracy and the generalization capability. Parameter optimization is thus crucial to obtain optimal performance. The cross-validation (CV) optimization method is usually applied in standard LSSVM [88]. Moreover, several optimization algorithms such as genetic algorithm (GA), particle swarm optimization (PSO), artificial bee colony (ABC), and differential evolution (DE) have been proposed for hyperparameter optimization [89]-[99].

In [89], an adaptive genetic algorithm was employed to update the LSSVM parameters. The authors used RBF to be the kernel function of the LSSVM, and the values of the parameters C and σ^2 were obtained using GA. This optimized LSSVM was used to form an efficient mapping structure for modeling nonlinear flux linkage characteristics of a 15-kW 12/8 SRM. The training data set was collected experimentally. The total number of the captured training data was 612, whereas the total number of test data was 126. The GA reduces the training time from 16 minutes when using a CV to 5 min.

Another LSSVM work was proposed in [90], where a grid diamond search (GDS) was employed to define the kernel function and the regularization parameters. GDS is based on grid search and diamond search methods. Grid search is applied first to speed up the search and identify the optimal space. The diamond searching algorithm then estimates the optimal solution in the best solution space. Although GDS has an extensive search range and fast convergence, it lacks relative search precision. The recorded computation time of GDS is 6 seconds, but it was 13 minutes for the CV method. The researchers in [90] used the proposed LSSVM-GDS to model the nonlinear characteristics of the flux linkage of an 8/6 SRM. Similar to [89], the rotor position and stator current are taken as inputs. The proposed model was verified by comparing the forecasted results with the measured data, which reflected satisfactory matching.

Another similar approach based on LSSVM was presented in [91]. A PSO was used to optimize the LSSVM hyper-parameters. The proposed LSSVM-PSO was used to model the inductance of a 1-kW 12/8 SRM. The training data set was obtained from a 3D FEA model of the considered SRM. The chosen kernel function in this work is RBF, and PSO optimized the parameters.

An improved 0.5-kW 12/8 SRM model based on LSSVM was introduced in [92]. Two cascaded single-output SRM models were replaced by a multi-output LSSVM to modify the model structure. The model inputs are flux linkage and rotor position, whereas the outputs are the phase current and torque. A combination of the RBF and poly kernel functions has been used to enhance the performance of the kernel functions. The parameters of the improved kernel functions were optimized using the CV optimization method. An experimental DC-pulse test was performed to obtain 1196 sample data set. The provided simulation results of the modified LSSVM model in [92] showed a decrease in the training time from 4.7 seconds to 2.619 seconds. Also, a noticeable improvement in the phase current model was demonstrated as the error reduced by 3%.

The authors in [97] have employed LSSVM with artificial bee colony (ABC) to model flux linkage characteristics of a 0.5-kW 4000-rpm 8/6 SRM. ABC is a meta-heuristic optimization algorithm that mimics the foraging behaviour of a bee swarm [98]. ABC was used in this work to tune the LSSVM hyperparameters. The sample data were obtained using a 2D FEA model. The current and rotor position resemble the model inputs. The training sample size is 450 data pairs, and the testing size is 154. The regression efficiency of the proposed LSSVM-ABC model was verified against other models such as LSSVM, LSSVM-GA, LSSVM-PSO, and LSSVM-DE. The LSSVM-ABC model offered the best modeling results, with a mean absolute error (MAE) of 0.066%.

The authors in [99] used LSSVM for modeling an 0.5-kW 8/6 SRM. They proposed LSSVM-DE to model the motor torque. The training data was collected using FEA. The number of data samples captured for training the algorithm is 732, and the test sample uses 144 sample data. In this paper, DE was chosen to optimize C and σ^2 parameters to accomplish the learning and training processes of the selected kernel function. The exponential RBF was selected to build the LSSVM-DE and validate its regression capability by comparing it with LSSVM, LSSVM-GA, and LSSVM-PSO. The proposed LSSVM-DE offered the most accurate regression model. Furthermore, the authors carried out a dynamic MATLAB simulation with the proposed LSSVM-DE-based model using the torque and current models. The behaviour of the proposed model imitated that of the FEA-based model.

Tables 3.1 and 3.2 summarize the motor modeling methods considered in this Chapter using the ANN and SVM algorithms, respectively. A fair comparison of MLAs used in modeling or designing motors requires some essential aspects, such as similar datasets and similar training techniques with the same trainable hyperparameters [94]. It should also consider the same motor type since many factors can change for different motors. Therefore, new studies in the same field are suggested to share the captured datasets to help assess future works.

Table 3. 1. Motor modeling methods using NN.

Ref.	Motor	MLA	Output (input)	No. of hidden layers / neurons	Activation function of hidden/ output layers	Dataset acquisition method / size	Error
[66]	12/8 SRM	LM-BPNN	$i(T,\theta)$	2/6	Tansig/ pure line	Measured	Error < 0.1 A
[67]	8/6 SRM	LM-BPNN	$\theta(i,\lambda)$	1/80	Sigmoid/ pure line	Measured / 496	APE =0.1266%
[41]	8/6 SRM	GDA-BPNN	$\lambda(i,\theta)$	2/-	Gauss/ gauss	Online measured	--
[68]	8/6 SRM	LM-BPNN	$i(\lambda,\theta)$ & $T(i,\theta)$	2/10	Tansig/ pure line	2D-FEA / 620	Target MSE=0.0001.
[69]	6/4 SRM	FNN	$\theta(i,\lambda)$	1/10	Sigmoid/ pure line	Measured / 1000	Error [-5° – +5°]
[70]	SRM	GDA-BPNN	$i(\lambda,\theta)$	2/8	Tangent/ pure line	Measured	--
[65]	12/8 SRM	LM-BPNN	$\theta(i,\lambda)$	1/5	Tansig	Measured	MSE=0.135 (1.51°)
[65]	12/8 SRM	RBFNN	$\theta(i,\lambda)$	1/69	Gauss	Measured	MSE=0.19 (2.07°)
[71]	8/6 SRM	RBFNN	$\lambda(i,\theta)$	1/6	Gauss	Measured /120	--
[58]	8/6 SRM	RNN	$(i,I_m)(i,\theta,v,\omega)$	--	Tansig/ pure line	Measured/800	Average covariance = 0.9127
[74]	6/4 SRM	ANFIS	$L(i,\theta)$	2/-	Gauss membership	2D FEA / 552	RMSE=3.461e-6
[76]	6/4 SRM	ANFIS	$\lambda(i,\theta)$ & $T(i,\theta)$	2/-	Gauss membership	Measured / 512	RMSE=1.78e-3 Wb & 0.022 Nm

Table 3. 2. Motor modeling methods using SVM.

Ref	SRM	MLA	Output(input)	Kernel function	Dataset acquisition method / size	Computation time (Sec)	Error
[84]	12/8	SVM-CV	$\lambda(i,\theta)$	RBF	Measured / 64	--	--
[89]	12/8	LSSVM-GA	$\lambda(i,\theta)$	RBF	Measured / 738	300	MAPE =0.0078%
[90]	8/6	LSSVM-GDS	$\lambda(i,\theta)$	RBF	--	6	--
[91]	12/8	LSSVM-PSO	$L(i,\theta)$	RBF	3D FEA	--	MRE=0.031%
[92]	12/8	LSSVM-CV	$i(\lambda,\theta)$ & $T(i,\theta)$	RBF-poly	Measured / 1196	2.619	MSE = 1.487e-3 A & 5.560e-5 Nm
[97]	8/6	LSSVM-ABC	$\lambda(i,\theta)$	RBF	2D-FEA / 604	--	MAE = 0.066 % MRE=0.38e-3 %
[99]	8/6	LSSVM-DE	$T(i,\theta)$	Exponential RBF	2D-FEA / 876	--	MAE=2.78e-5 % RMSE=3.89e-5%

3.4 Machine Learning-Based Algorithms for SRM Design Optimization

The design optimization of electric machines is a nonlinear multi-objective problem [35]. It requires repeated calls to the electromagnetic solver. Repeatedly invoking FEA within an optimization loop can be prohibitive. To reduce the computational time of the optimization problems, different surrogate models have been introduced in the literature. Space mapping (SM) aims at utilizing a fast “coarse” model with reduced accuracy [100] to design an accurate but time-intensive “fine” model. SM was proposed in [101] to design a brushless DC motor. A kriging surrogate model was used with an evolutionary algorithm to optimize a three-phase PMSM in [102]. Researchers have recently used MLAs as surrogate models due to their high accuracy and effective generalization ability compared to other models.

At the beginning, an initial FEA model is developed to create a reasonable dataset with various combinations of motor geometric parameters. An MLA is then trained using this dataset to map out the nonlinear relationships between the geometric input parameters and corresponding objectives at different operating conditions. The MLA provides a good surrogate model of the computationally expensive FEA. Finally, a multi-objective optimization algorithm is applied to get the optimal design. The surrogate ANN is repeatedly invoked by the optimization algorithm to guide the optimization iterates.

An SRM design process might not be straightforward due to its high nonlinearity. Multiple geometric design parameters should be optimally chosen to fulfill the requirements of the application. These parameters include the number of stator and rotor poles, bore diameter, pole arc angles, taper angles, air gap length, etc. The authors in [14] focused on designing the stator pole arc angle β_s and rotor pole arc angle β_r, shown in Fig. 3.12, due to their direct impact on the inductance and torque profile.

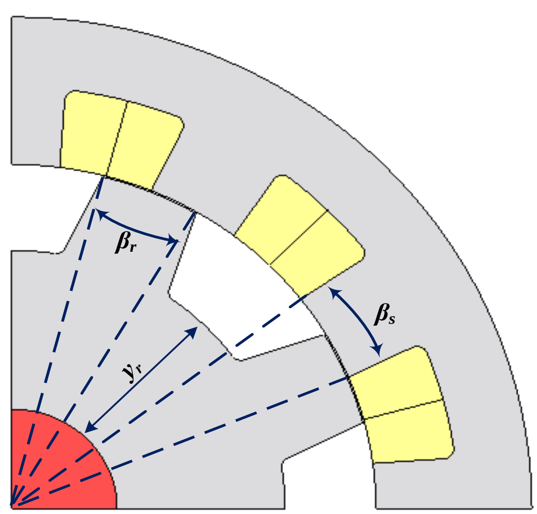

Fig. 3. 12. A quarter model of the considered SRM showing the stator and rotor arc angles.

In [14], a generalized regression neural network (GRNN) was employed in the design procedure of a 3-phase 12/8 SRM. GRNN is a class of probabilistic ANN with a simple structure and fast convergence [103]. It has a good generalization ability, especially with a relatively small training dataset. GRNN has similarities with the RBF method, as it has an RBF layer in its structure and a special linear layer. Furthermore, GRNN has a single adjustable parameter known as the spread parameter. This parameter controls the GRNN generalization capability. It should be carefully optimized to enhance the prediction of the motor performance.

The authors in [14] used FEA to obtain static torque characteristics of the considered motor. The static torque characteristics were collected for 35 various combinations of both β_s and β_r considering some predefined pole arc angles constraints [14]. These constraints were selected to guarantee a fully unaligned position and ensure self-starting capability [104]. In addition, β_s (see Fig. 3.12) was chosen smaller than β_r to slightly increase the copper winding area and aligned/unaligned inductance ratio. The static characteristics were utilized to get the average torque and the torque ripples. A GRNN is trained to fit input data with specific label data. The trained GRNN is then validated using test data.

In [14], an optimization algorithm that exploits GRNN as a surrogate was applied to get the optimal combination of β_s and β_r to maximize the torque and minimize the torque ripples. The torque ripple was reduced by 12% compared to the initial design. The proposed method was validated by simulating the optimal geometry using FEA, and the output results were in good agreement with the results of the proposed approach.

In [105], another work using GRNN was proposed for the modeling a 4-kW 12/8 SRM. The model represents the nonlinear relationship of the ripples and operation efficiency with three geometric variables: β_s, β_r and rotor yoke thickness, y_r (see Fig. 3.13). The spread parameter was optimized using the fruit fly optimization algorithm (FOA), which is based on the foraging pattern of the fruit fly swarm [105]. FEA was used to capture a dataset of 105 samples for training. 15 data samples were used to test the GRNN. The results show the superiority of the FOA-GRNN model compared to the traditional GRNN.

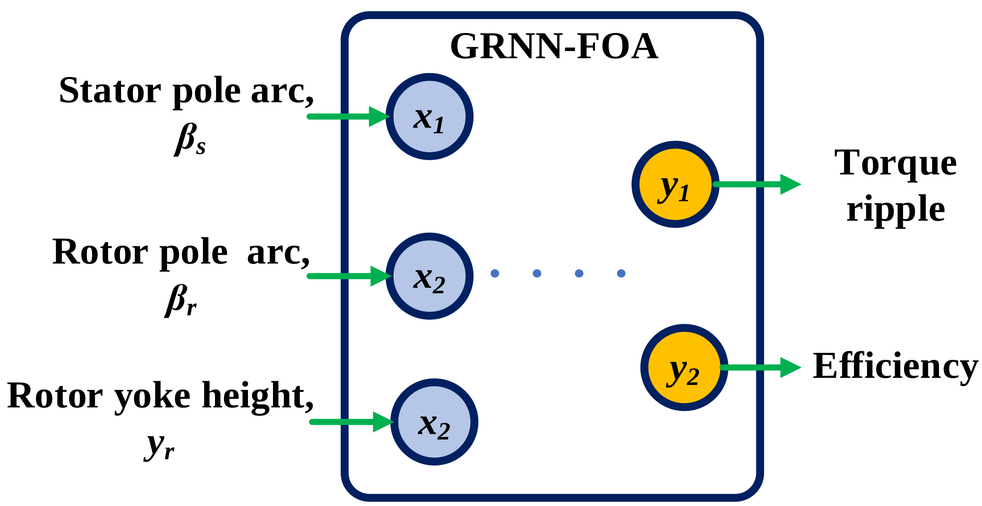

Fig. 3. 13. The GRNN Input-output modeling system proposed in [105].

3.5 Summary

This Chapter presented a review of the applied machine learning algorithms in the modeling and geometry design optimization of SRMs. Many MLAs are appropriate for modeling and design of SRMs. According to the presented and discussed studies in this Chapter, all applied MLAs in this field are supervised learning algorithms. The feedforward neural network and the support vector machine represent 75% of the considered articles in this literature review. Most of the studies take the current and rotor position as inputs of the proposed algorithm and the torque and/or flux linkage as outputs. The sample data was either acquired using the 2D-FEA simulation or based on a locked rotor test experiment. Although the experimental method gives more accurate prediction results, it requires sophisticated sensors and tools.

The quality and size of the data samples are essential for achieving a good prediction model. There is no general rule for splitting the sample data into training, validation, and testing sets. However, the training set commonly forms more than two-thirds of the total sample data. The training process of the neural networks is an optimization problem. Levenberg Marquardt offered the fastest and most accurate learning algorithm for backpropagation neural networks. In LSSVM, determining the kernel function and regularization parameters requires optimization algorithms as well. The RBFNN is superior in approximation ability and convergence speed. However, its significant modeling error requires a larger network scale as compared to the BPNN based on the LM learning algorithm.

The ML-based models are used as surrogates in electric motor design due to their high accuracy and effective generalization ability. The main contribution of the MLAs in this field is reducing the computational time of the design optimization process. Generally, the prediction accuracy of the MLAs and computation cost are key guidelines to assess modeling and design methods.

Chapter 4

SRM Design Optimization: A Framework for Effective Machine Learning Algorithm Selection and Evaluation

The design process for SRM geometry follows a multi-stage and iterative approach [107]. It begins with an initial static analysis using finite element analysis (FEA) to generate look-up tables for flux linkage and static torque. Dynamic analysis follows using MATLAB simulations based on the established look-up tables. Then, the conduction angles are optimized for each geometrical change to improve the SRM torque profile [9].

These iterative design steps are repeated until the optimal design is reached, leading to prohibitive computational time.

Notably, MLAs have recently acquired attention in electric machine design due to their capacity to learn and accurately predict nonlinear parameters and performance outputs [13]. Using the MLAs as surrogate models to replace the FEA and MATLAB analyses can significantly decrease the computational time of the motor design [11].

As discussed in Chapter 3, MLAs are broadly classified into supervised, unsupervised, and reinforcement learning techniques. Among these, supervised learning algorithms, particularly the back-propagation neural networks (BPNN), radial basis function neural networks (RBFNN), and generalized regression neural networks (GRNN) are commonly applied to motor modeling and design [13],[14],[15]. These algorithms differ in their structural composition and operational principles. The selection criteria for the appropriate MLAs as a surrogate model are influenced by several factors such as model structure, execution time, generalization ability, and fitting accuracy.

The main objective of this Chapter is to apply MLAs in SRM geometrical design. However, differences in MLA structure, training, and processing times challenge motor designers in selecting the best MLA and formulating an efficient evaluation method. Therefore, this Chapter introduces an extensive analysis of various MLAs applied to SRM modeling and design. Additionally, it presents a robust framework for a comprehensive evaluation of these MLAs, facilitating the selection of the optimal machine learning topology for SRM design. Moreover, this Chapter addresses the key challenges associated with the learning process, such as overfitting and underfitting concerns.

The MLAs under consideration include BPNN, GRNN, and RBFNN. Additionally, this Chapter explores conventional regression fitting algorithms such as polynomial and quadratic regression methods. To capture the required training dataset, an FEA and MATLAB modeling are developed to get the static and dynamic properties of the SRM under consideration. Subsequently, these MLAs are employed to build a surrogate model for static and dynamic characteristics, including the optimization of conduction angles. In Chapter 5, the selected MLA is utilized to predict the optimal geometrical parameters that enhance the performance of the considered SRM.

4.1 Pole Arc Angles Design Effect and Constraints

Table 4.1 presents the key geometrical parameters of the initial (baseline) design of the 6/14 SRM examined in this study, while Fig. 4.1 provides a visual representation of its geometric structure. This motor, as detailed in [106], was designed as a furnace blower motor with a 1 HP rating for household applications. Among the SRM geometrical parameters, the stator and rotor pole arc angles exert significant influence over the static and dynamic performance of SRMs, underscoring the need for precise design considerations [1]. Consequently, our focus in this thesis is on optimizing the pole arc angles of the SRM to enhance motor performance.

Table 4. 1. Parameters of the considered 6/14 SRM

Parameter	Symbol	Value
DC-link Voltage [V]	VDC	163
Power rating [hp]	P	1
Machine base speed [RPM]	RPM	1103
Peak reference current [A]	I_{ref}	6.66
Stack length [mm]	L_{st}	74
Stator outer diameter [mm]	D_s	139.21
Shaft diameter [mm]	D_{sh}	12.7
Air gap length [mm]	L_g	0.4
Stator back iron thickness [mm]	y_s	10
Rotor back iron thickness [mm]	y_r	35.78
Stator pole height [mm]	h_s	10
Rotor pole height [mm]	h_r	7.08
Stator pole arc angle [°]	β_s	9.5
Rotor pole arc angle [°]	β_r	9.3
Stator taper angle [°]	τ_s	4
Rotor taper angle [°]	τ_r	4

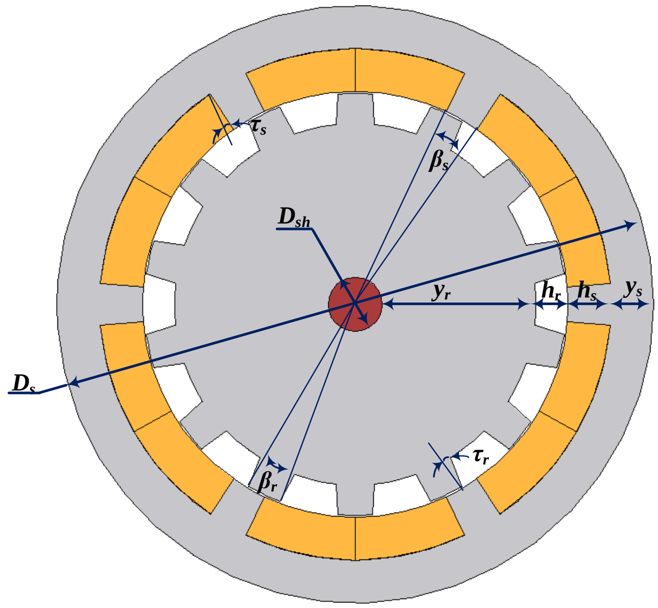

Fig. 4. 1. The FEA JMAG full model of the considered 6/14 SRM.

Generally, the SRM pole arc angles are carefully selected. Increasing the stator pole arc angle β_s widens the stator teeth, increases the aligned flux linkage and extends the SRM torque angle at each pulse, which might cause lower torque ripples. The excessive increase in β_s, however, can reduce the motor saliency, thus decreasing the peak and RMS of the output torque [108]. Moreover, a larger β_s can compress the winding space, and this can reduce the number of turns, which leads to a torque reduction [108]. Similar to β_s, slightly increasing the rotor arc angle β_r widens the rotor teeth and would boost the aligned flux linkage, which enhances the output torque. Also, the excessive increase in β_r would reduce the motor saliency, and as a result, the output torque production could be decreased [108]. Therefore, the design of the SRM pole arc angles is sensitive and crucial.

In SRMs, pole arc angles have a powerful effect on the inductance and torque quality profiles. Electromagnetic torque production is contingent on the changes in magnetic reluctance. To ensure this, the design of the length of the stator and rotor pole arcs should guarantee a fully unaligned position. Otherwise, the rotor tooth of the SRM will partially or totally align with the stator tooth at any rotor position. Therefore, to maintain this condition, the stator tooth arc length should be lower than the arc length between two successive rotor teeth [1]. This condition defines the maximum values of β_s and β_r.

Furthermore, the minimum values of β_s and β_r should guarantee the self-starting capability of SRMs [1]. The applied constraints of β_s and β_r are identified in (4.1) for the given number of phases, m and rotor poles, N_r [20]. Based on these constraints, the range of possible combinations of β_s and β_r is [8.00°:12.00°]. These bounds are given by [1]:

$$\frac{4\pi}{mN_r} \leq \beta_s + \beta_r < \frac{2\pi}{N_r} \tag{4.1}$$

4.2 Training Data Acquisition

To effectively model and design an SRM using an MLA, it is crucial to accurately capture sample data that depicts the correlation between the variation in the input design parameters and the corresponding output objectives. Electromagnetic modeling is thus conducted to study the static analysis of the considered SRM. Following that, a dynamic analysis is carried out to determine the output objectives for each design candidate. This dynamic model includes conduction angles optimization to ensure optimal performance. In this section, we present a detailed explanation of the static and dynamic modeling required to generate the required training data.

4.2.1 Static Characteristics Modeling

Electromagnetic modeling forms the basis of SRMs geometrical design optimization. As discussed in Chapter 3, the modeling methods can be categorized into numerical and analytical approaches [13]. Analytical-based modeling methods are possibly used in the static analysis of SRMs. However, they commonly require various assumptions, which are not usually easy to provide [24]. These approaches do not accurately account for motor nonlinearities [1]. Therefore, in this study, we employ a numerical FEA-based modeling method, which is recommended for the static characterization of SRMs [1]. FEA is the most widely used numerical modeling method. The FEA model is applied to characterize the static flux linkage and torque profiles of the 3-ph 6/14 SRM at different rotor positions and phase currents.

The study of static phase characteristics is pivotal for understanding the operational principles and nonlinear behavior of the switched reluctance machines. In this research, the static characteristics of the considered SRM are the flux linkage, induced voltage, and phase torque when a single phase is excited by a constant current over the entire electrical cycle. This is because the mutual coupling among phases is neglected in this work.

In traditional configurations of switched reluctance machines, which possess an even number of stator poles per phase, as is the case with the SRM under investigation in this study, mutual coupling occurs momentarily during each cycle. Generally, this effect can be disregarded when formulating a model for an SRM [1]. This is because when current is applied to the coils of a typical SRM phase, the bulk of the resulting magnetic flux is interlinked with the coils of the very same phase. Hence, in the FEA conducted in this research, a single phase is energized with a constant current throughout one complete electrical cycle.

Subsequently, we relatively increased the static current applied to energize the phase to simulate the impact of core saturation. The static flux linkage and torque profiles at various rotor positions and phase currents are depicted in Figs. 4.2 and 4.3, respectively. Fig. 4.2 illustrates that the incremental rise in the flux linkage diminishes at high currents due to the elevated magnetic flux density, resulting in a higher level of core saturation. Furthermore, it is worth noting that the look-up tables (LUTs) created for one phase can be effectively employed to model all phases.

To cover the entire design domain while adhering to the given constraints, 50 different configurations with appropriate pole arc angles are considered. The static characteristics of each SRM design are then imported into a MATLAB/Simulink model for dynamic analysis. The dynamic analysis provides the average torque and torque ripples values for each design candidate for performance assessment.

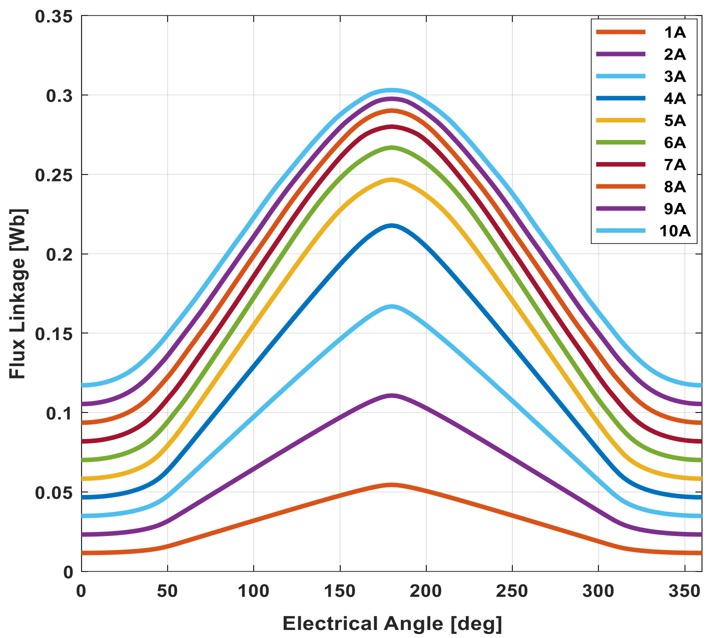

Fig. 4. 2. The static flux linkage characteristics of the 6/14 SRM at various rotor positions and phase currents.

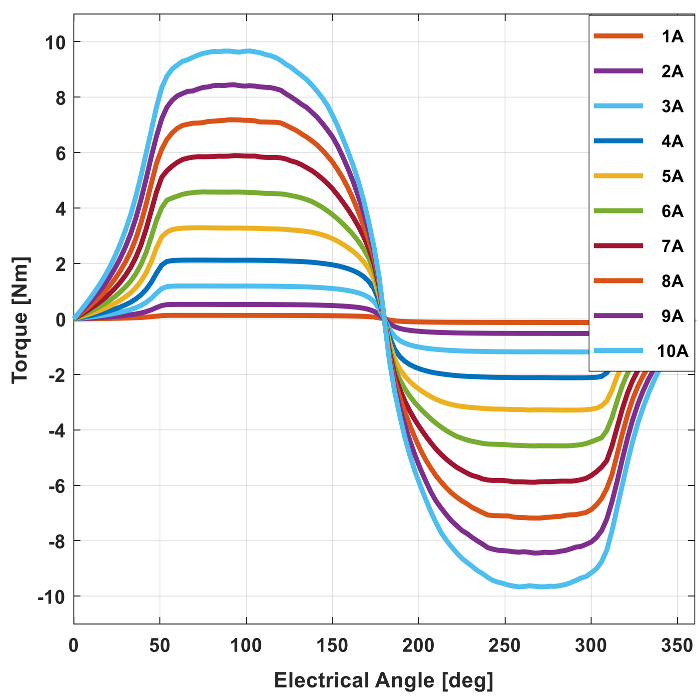

Fig. 4. 3. The static torque profiles of 6/14 SRM at various rotor positions and phase currents.

4.2.2 Dynamic Characteristics Modeling

In contrast to PMSMs and IMs, SRMs do not operate with sinusoidal currents. The switching nature of the SRM magnetic field makes it challenging to directly apply phase transformation techniques to drive SRMs [1]. Consequently, SRMs require distinct modeling approaches to study their dynamic behavior. The developed dynamic model in this work assesses the motor's performance while operating at a constant speed, considering the dependency of the flux linkage on the current and rotor position. This dynamic model computes the dynamic average torque and torque ripples by exciting the phase for given firing angles, motor speed, and DC-link voltage.

In this section, we explain the utilized MATLAB Simulink model and how it exploits the offline phase flux linkage LUTs generated from FEA simulations. The Simulink model is primarily built based on the equivalent circuit and the voltage equation (2.2) discussed in Chapter 2. This model is formulated as a discrete-time domain with a fixed time step. Solving (2.2) for the flux linkage in discrete time domain form and looking up the current based on the past flux values, we get:

$$\lambda_{ph}(k)=\lambda_{ph}(k-1)+[v_{ph}(k)-R_{ph}i_{lut}(\lambda_{ph}(k-1),\theta_{elec}(k-1))]T_s\ , \tag{4.2}$$

where k is the discrete step value and T_s is the sampling time. i_{lut} is the current required to get a specific flux linkage at a certain electrical angle, θ_{elec}. This i_{lut} can be derived from the inversion of the phase flux linkage LUT. Using (4.2), a dynamic simulation model can be implemented to solve for the SRM flux linkage and current. The calculated current waveform can then be employed to evaluate the torque, as depicted in Fig. 4.4.

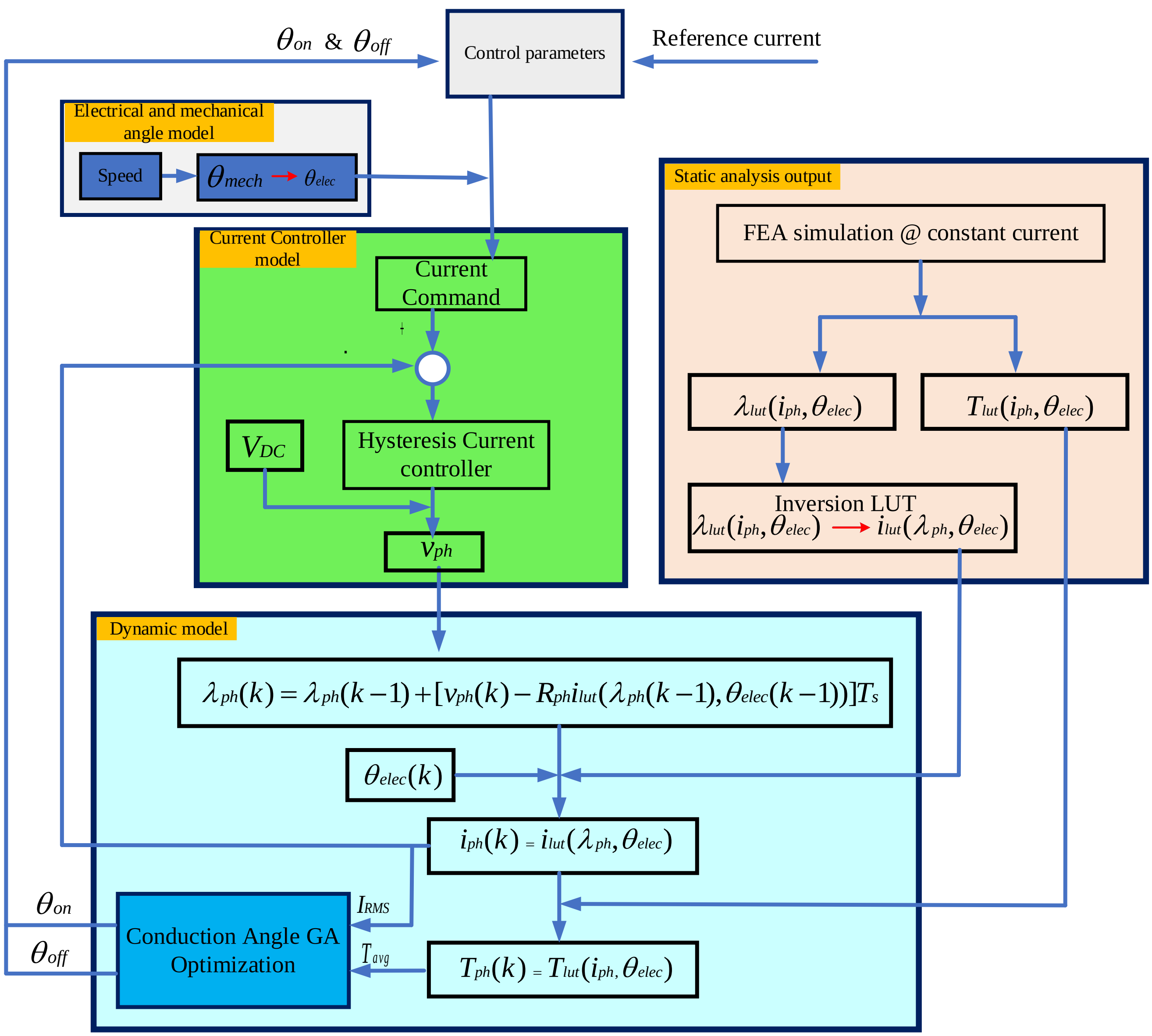

Fig. 4. 4. A simplified chart for the developed dynamic model for the considered SRM.

The dynamic model of the SRM also includes the angle model and hysteresis current controller model. The correlation between the SRM phase voltage and current relies on the current control method, with the current being regulated by an asymmetric bridge converter and various control parameters, as discussed in Chapter 2. Typically, the primary control parameters are the reference current and turn-on and turn-off angles, which are utilized to generate the commanded current for phase current regulation. Hysteresis control is applied in SRM drives to maintain tracking of the reference current. When the phase current achieves the reference current value, the hysteresis controller maintains it within the predefined hysteresis band. Fig. 4.4 shows a simplified chart for the developed dynamic model.

4.2.3 Conduction Angle Optimization

The current control at low speeds can track the reference current to achieve the proposed torque, while the conduction angles can decrease the ripples and enhance motor efficiency [1]. On the other hand, tracking the peak current at high speeds is not attainable due to the high induced voltage. In such cases, the conduction angles would be the sole control parameters. Therefore, to enhance the SRM performance at various operation conditions, the selection of conduction angles, turn-on, θ_{on} and turn-off, θ_{off} angles, should be made with utmost precision.

Tuning the conduction angles manually for each geometrical design candidate is considerably time-consuming [1]. Therefore, in this thesis, an optimization algorithm based on a genetic algorithm (GA) [109] is applied to speed up getting the optimal candidate firing angles. The main objective used in the developed genetic optimization algorithm is maximizing the average torque T_{avg} which is evaluated as:

$$f_{obj} = T_{avg} = \frac{1}{\theta_{cycle}} \int_{0}^{\theta_{cycle}} T(\theta)d\theta \ . \tag{4.3}$$

The average torque is determined based on the instantaneous phase torque, $T(\theta)$ over one complete electrical cycle θ_{cycle}.

The GA population size was selected as 80, and the maximum number of generations was set to 20. These parameters provide a combination of good accuracy and adequate simulation time. Linear constraints are set for the range of the θ_{on} and θ_{off} to effectively cover the operation within the application design space [9]:

$$\begin{aligned} \theta_{on} &\in [-90, 90] \\ \theta_{off} &\in [70, 180] \end{aligned} \tag{4.4}$$

The angle boundary is selected to ensure positive torque production without having a large overlap angle between the phase commutation, which can cause high torque ripple,

$$\begin{aligned} \theta_{on} - \theta_{off} &< \frac{-360}{m} \\ -\theta_{on} + \theta_{off} &< \frac{360k}{m} \end{aligned} \tag{4.5}$$

The parameter K can be tuned depending upon the application requirements. For this application, K is set to 1.4. Also, a nonlinear constraint is set for the phase RMS current, I_{RMS}, which is calculated based on the instantaneous phase current, I_{ph} as follows:

$$I_{RMS} = \sqrt{\frac{1}{\theta_{cycle}} \int_{0}^{\theta_{cycle}} i_{ph}^{2}(\theta)d\theta} \leq I_{RMS\_constraint} \tag{4.6}$$

After running the FEA simulation using JMAG software for the base design of the considered SRM, the generated LUTs are implemented in the developed dynamic Simulink model and executed at the base speed of 1103 RPM. The θ_{on} and θ_{off} are optimized to maximize the average torque. The dynamic model was executed so that the initial two cycles were designated as transient periods, and the subsequent cycles were employed for the calculation of average torque and torque ripples. The average torque per phase and total torque of the third electrical cycle are shown in Fig. 4.5.

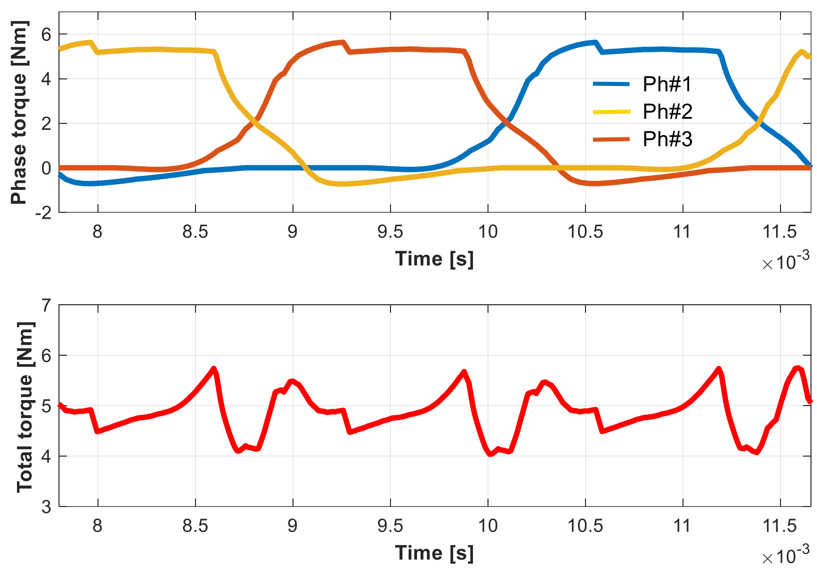

Fig. 4. 5. The phase and total average torque of the base design of the considered 6/14 SRM.

In order to capture the complete necessary training data, a parametric sweep was conducted for the pole arc angles while considering the previously mentioned constraints. This resulted in the acquisition of 50 design candidates. Following this, FEA analysis was carried out, and the flux linkage and average torque LUT were imported to the SRM dynamic drive model. For each design candidate, the conduction angles were optimized using the GA to achieve maximum average torque. Therefore, the trained MLA not only acts as a surrogate for the FEA analysis but also for the dynamic model, including the GA optimization of the conduction angles.

To ensure the quality of the output torque, the RMS value of the torque ripple is determined in equation (4.7) using the developed dynamic model. The torque ripple of each design candidate is also utilized as a second output for the MLA. For example, Table 4.2 shows five samples out of the 50 samples that were used to train the developed MLA. The MLA can thus predict the average torque and torque ripples for any new SRM pole arc angles. This facilitates the selection of the optimal design candidate considering both the net output torque and torque quality.

$$\Delta T_{RMS} = \sqrt{\frac{1}{\theta_{cycle}} \int_{0}^{\theta_{cycle}} (T(\theta) - T_{avg})^2 \, d\theta} \tag{4.7}$$

Table 4. 2. Some examples of the training data

β_s [°]	β_r [°]	Average torque T_{avg} [Nm]	Torque ripples ΔT_{RMS} [Nm]
8.5	9	4.688	0.413
9	9	4.736	0.367
9	10	4.897	0.311
9.5	9	4.832	0.399
9.5	10	5.024	0.428

4.2.4 Dynamic Model Validation

To validate the developed dynamic model, the three-phase current waveforms of the baseline design which were computed within the MATLAB dynamic model, shown in Fig. 4.6, are imported into the FEA static model of the SRM. Subsequently, we compared the torque waveforms generated by the dynamic model and the FEA model. The comparison, as illustrated in Fig. 4.7, reveals a close match between the torque waveforms. It is important to emphasize that mutual coupling was not considered in the dynamic model, whereas the FEA simulations inherently account for mutual coupling effects. The strong agreement between the results underscores the insignificance of mutual coupling when modeling this SRM drive with the optimized firing angles. It should be highlighted that the validation process using the FEA demands a substantially longer computational time as compared to the established dynamic model. This observation emphasizes the significance of dynamic modeling as an efficient and practical approach for our study.

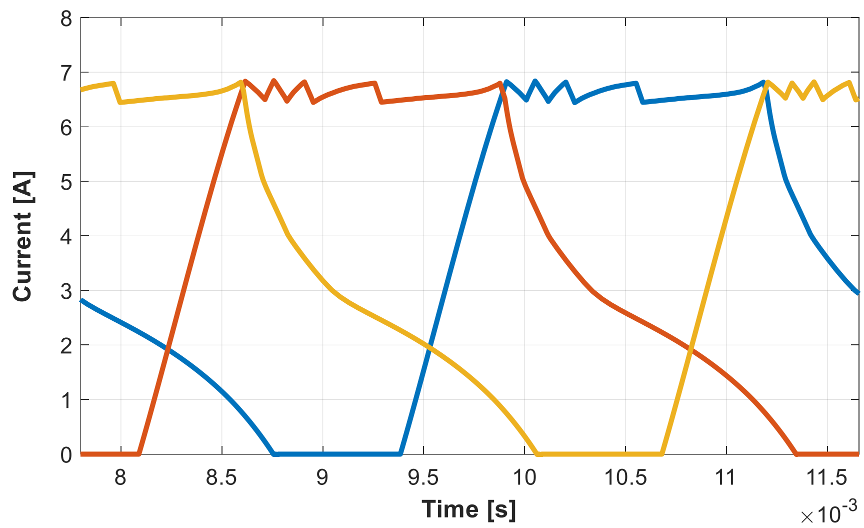

Fig. 4. 6. Three-phase dynamic currents of the baseline design of the considered SRM at base speed and peak reference current (6.66A) and for θ_{on} = -30.5° and θ_{off} =137.47°.

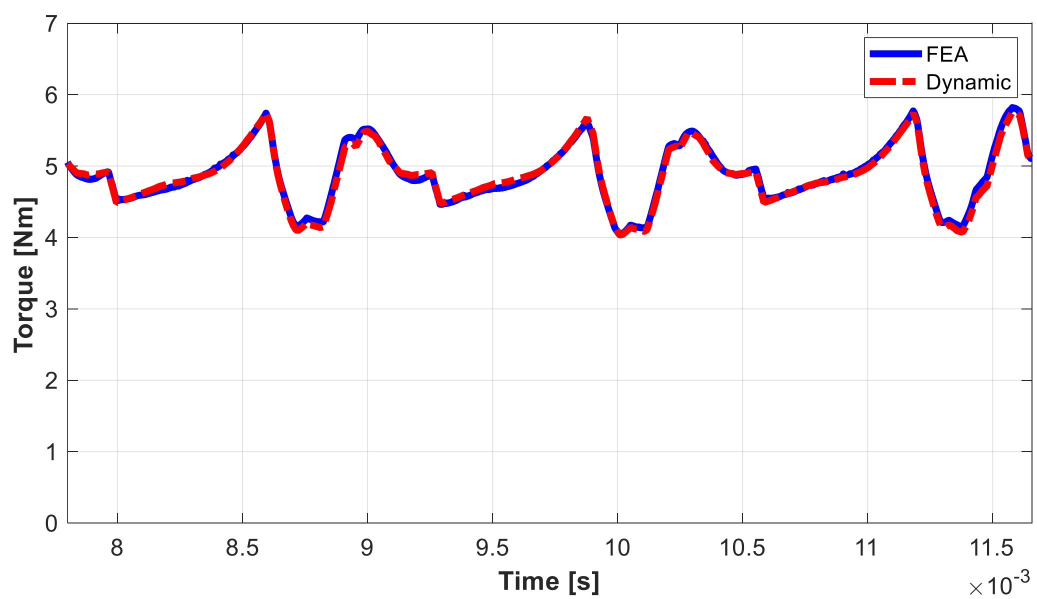

Fig. 4. 7. A Comparison of torque calculated from the FEA and dynamic models for the baseline design.

4.3 Machine Learning Algorithms

In this study, the MLA is employed to map out the nonlinear relationships between pole arc angles and motor performance, specifically focusing on average torque and torque ripples. Within the realm of machine learning, this endeavor is categorized as a regression problem, making supervised learning algorithms the best fit for motor design problems [13]. However, various supervised learning algorithms are suitable for motor design, like BPNN, RBFNN, and GRNN. These supervised learning algorithms differ in their structure, training algorithms, and processing time, which poses a challenge for motor designers in selecting the most suitable MLA and formulating an efficient evaluation approach.

Hence, this section undertakes a thorough comparison of these algorithms, accompanied by a set of evaluation criteria. The exploration begins by employing traditional 3D scatter fitting methods, specifically the second-degree polynomial and locally weighted smoothing quadratic regression (LWSQR) techniques. Followed by an in-depth examination of BPNN, RBFNN, and GRNN. The following subsections present the fundamental principles, structure, and training outcomes of the respective algorithm.

4.3.1 Second-Degree Polynomial 3D Scatter Fitting Method

The MATLAB 3D scatter fitting tool is employed to construct two second-degree polynomial models. The first model is employed to establish the relationship between SRM pole arc angles and average torque, while the second model is dedicated to correlating SRM pole arc angles with torque ripples. The collected training dataset is utilized to determine coefficients that minimize the disparity between predicted values from the polynomial models and the actual data points. To evaluate the fitted model, the assessment metrics are calculated to examine how closely the polynomial curved surface aligns with the actual data points.

4.3.2 Locally Weighted Smoothing Quadratic Regression Method

The LWSQR method offers a systematic framework for modeling complex data relationships. This approach combines local regression and smoothing techniques to construct finely tuned quadratic regression models that capture the variations of the dataset. Initially partitioning the dataset into smaller subsets, the method applies local regression to fit quadratic models to the data points within each subset. By incorporating a smoothness parameter, the LWSQR method ensures a delicate balance between accurately capturing data trends and maintaining overall smoothness in the resulting curves and surfaces. In this study, we employed two 3D locally weighted smoothing quadratic regression models to establish the connection between SRM pole arc angles and both average torque and torque ripples. The smoothness parameter is carefully adjusted to balance the precision of the fitting against the overall smoothness of the model. Using the obtained training dataset, we developed an optimal LWSQR model that accurately fits the data.

4.3.3 Back-propagation Neural Network

Fig. 4.8 displays the structure of the BPNN, consisting of two inputs for stator and rotor pole arc angles and two outputs for the average torque and torque ripples. This BPNN has only one single hidden layer, utilizing Tansig as the activation function for its hidden neurons. The number of optimal hidden nodes was identified as 8. The output layer uses a linear activation function for both outputs.

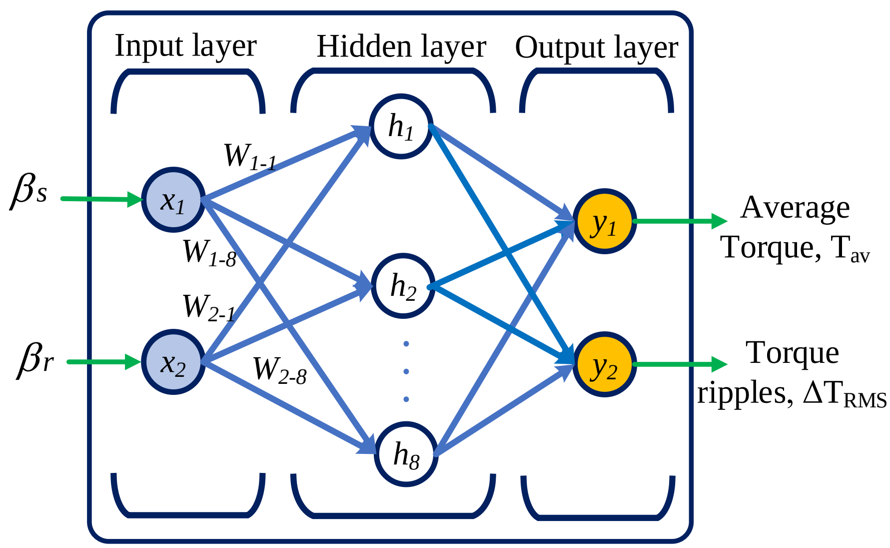

Fig. 4. 8. The basic architecture of the proposed single-layer BPNN to model the considered 6/14 SRM.

The decision to employ one hidden layer with eight neurons was determined through a heuristic approach. It balances the trade-off between the training accuracy and model complexity. Increasing the number of layers or nodes, the training accuracy may improve, but there is a higher likelihood of overfitting. Overfitting indicates that the model structure is complex and fails to achieve an optimal fit with new data. It occurs when the gap between training and test errors becomes substantial, resulting in a notable generalization error [13].

In this Thesis, the Levenberg Marquardt (LM) is used to train the BBPN, addressing the shortcomings of the Newton and GDA methods, as detailed in Chapter 3. To assess the network's performance, the mean square error (MSE) was used as the loss function with a target error set at 0.0001. The training dataset, comprising 50 points, was partitioned into 70% for training, 15% for validation, and 15% for the testing set. LM-BPNN managed to finish the training process in 17 epochs. Fig 4.9. shows the error convergence curve for training, validation, and testing with respect to the number of epochs.

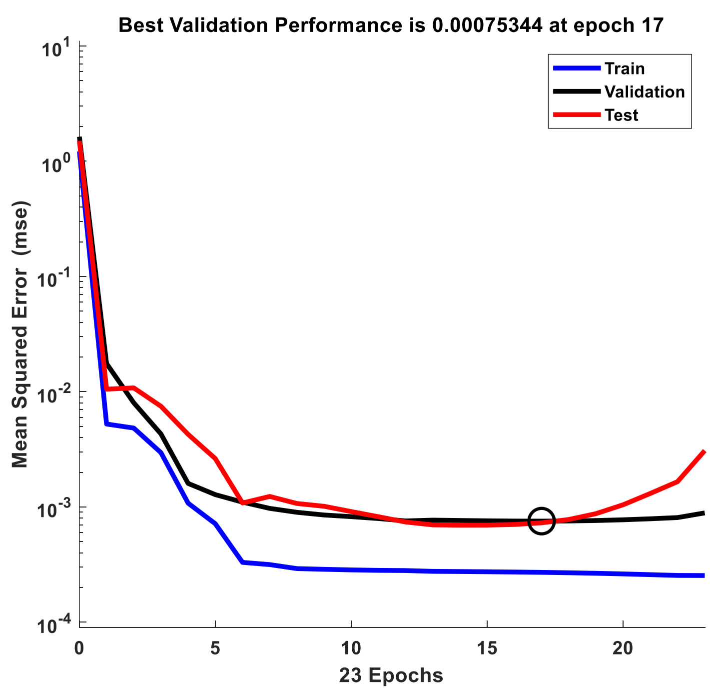

Fig. 4. 9. The train, validation, and testing profiles of the BBNN.

4.3.4 Radial Basis Function Neural Network

The proposed structure for the RBFNN aims to establish correlations between SRM pole arc angles and both average torque and torque ripples. It consists of a single hidden layer with ten hidden neurons, as shown in Fig. 4.10. The key components of the RBFNN architecture are the radial basis functions (RBFs) within the hidden layer. These RBFs commonly employ Gaussian functions as activation functions for their hidden nodes. The proposed RBFNN successfully completed the training phase within 500 epochs.

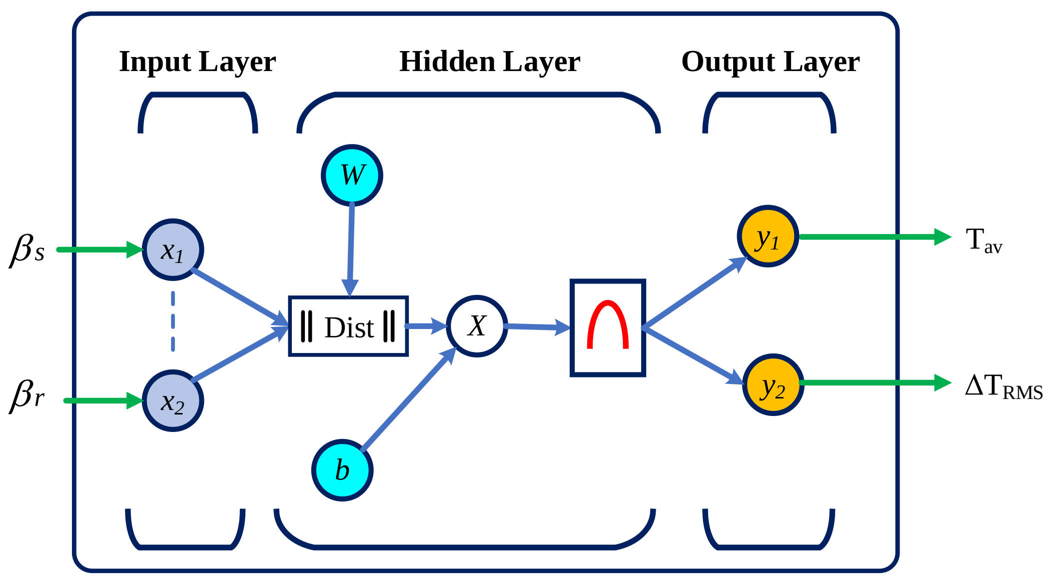

Fig. 4. 10. The schematic diagram of the proposed RBFNN.

4.3.5 Generalized Regression Neural Network

GRNN is a class of probabilistic neural networks and possesses a straightforward architecture without any hidden layers. GRNN shares similarities with the RBF method, featuring an RBF layer within its structure [13],[36]. Additionally, GRNN incorporates a single adjustable parameter called the spread parameter, which plays a crucial role in determining the network's generalization capability. In this study, cross-validation is utilized to optimize the spread parameter to achieve the highest accuracy in predicting motor performance. Fig. 4.11 shows the architecture diagram of the GRNN.

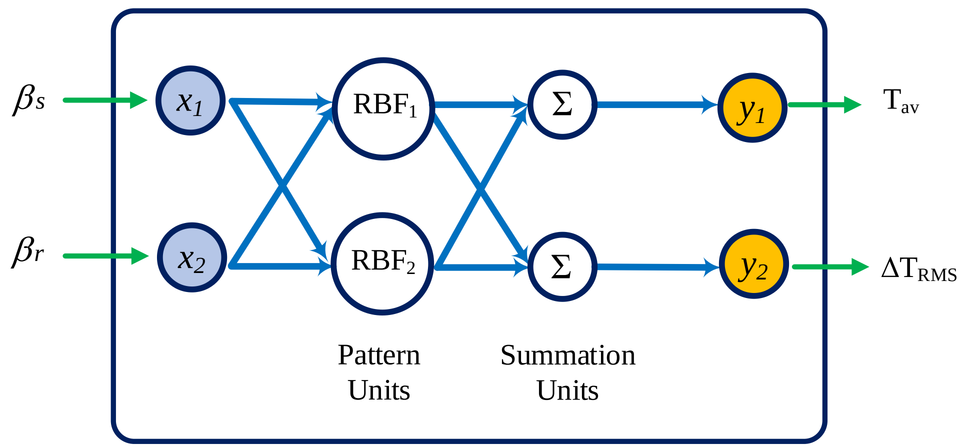

Fig. 4. 11. The basic architecture of the GRNN.

4.4 Evaluation and Selection of Optimal MLA

The correlation between the SRM's pole arc angles and motor performance exhibits a high degree of nonlinearity, demanding a precise surrogate model to effectively approximate this relationship. Additionally, the RMS value of the torque ripples of the considered SRM falls within the range of 0.2 to 0.7 Nm, indicating a high sensitivity in predicting torque ripple values. Consequently, the evaluation process to ensure the robust reliability and accuracy of the developed MLA is highly important in this study.

Fig. 4.12 provides an overview of the evaluation framework applied to the developed MLAs to select the optimal algorithm that effectively provides a surrogate model for the static and dynamic properties of the SRM under consideration. The evaluation process is initiated with an analysis of the training and testing performance of the developed MLAs, measured through key metrics, including MSE and the linear regression correlation coefficient (R). The evaluation results, detailed in Table 4.3, showcase a comparable level of accuracy across all five developed algorithms in fitting the training dataset. However, for a comprehensive assessment, it is imperative to investigate the trained models' generalization capability and potential overfitting. Therefore, an additional evaluation loop, as illustrated in Fig. 4.12, has been incorporated to test generalization accuracy and identify the optimal MLA.

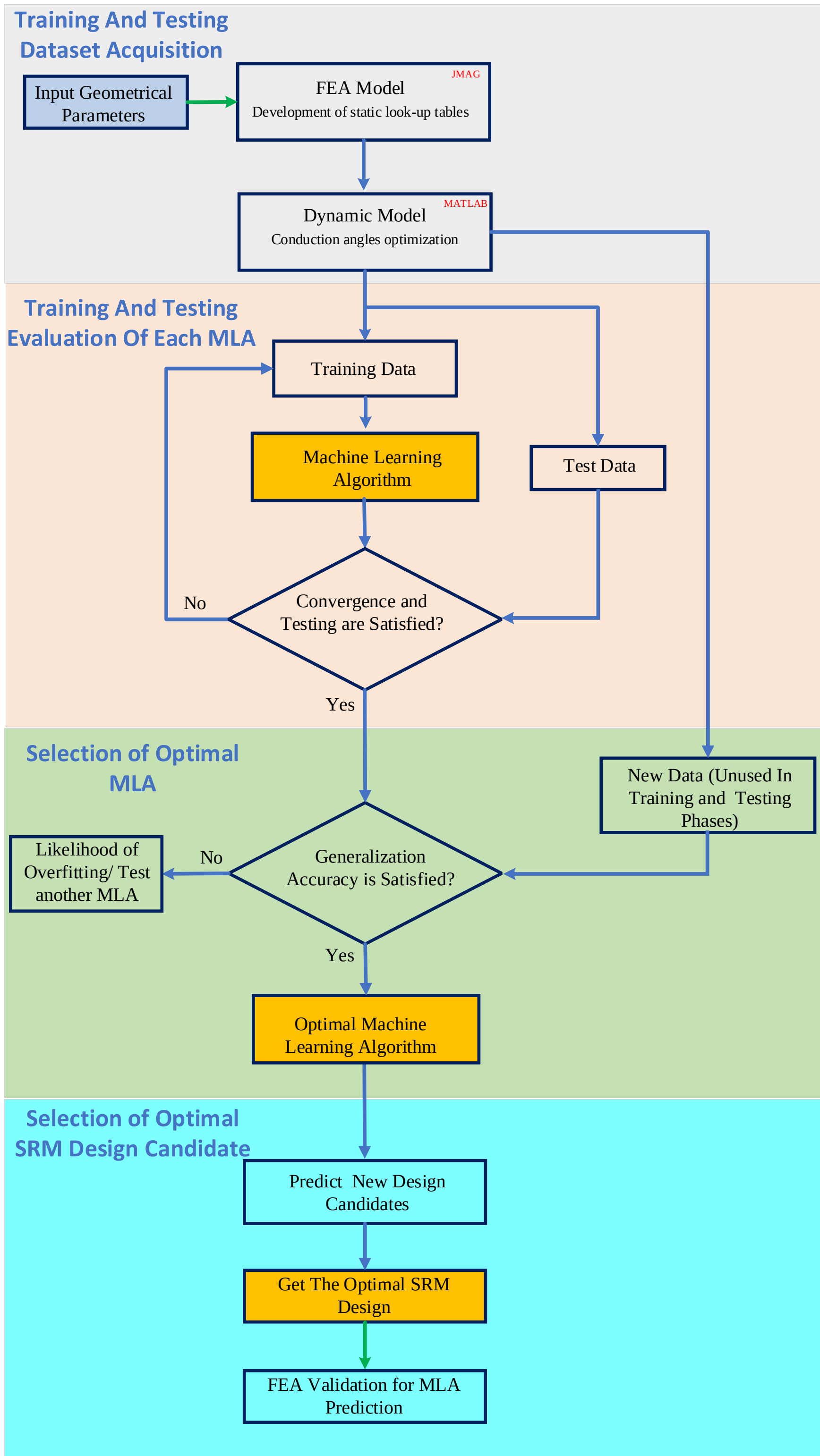

Fig. 4. 12. Block diagram of the evaluation framework for MLAs optimizing the pole arc angles in SRMs.

Table 4. 3. The performance metrics for the training and testing datasets of the 3D scatter fitting methods, BPNN, RBFNN and GRNN.

Parameter	2nd-degree Polynomial	Quadratic Regression	BPNN	RBFNN	GRNN
MSE (Nm)	17.1e-04	2.94e-04	2.706e-4	2.13e-4	4.08e-4
R	0.9388	0.9899	0.99995	0.9984	0.9962

Since the training and testing results are satisfactory for all developed algorithms, this section aims to ensure that the models will perform well when predicting motor performance for new design candidates. The generalization capability of the machine learning surrogate models is assessed utilizing a dataset comprising 10 points that were excluded in the training and testing phases. Fig. 4.13 and Fig. 4.14 illustrate the error between the predicted and actual values of average torque and torque ripple, respectively. Notably, the BPNN exhibits the minimum error values for both average torque and torque ripple across nearly all ten design points. It is observed that the algorithms predict the average torque with higher accuracy than the torque ripple, indicating the high nonlinearity of the torque ripple's relationship with changes in pole arc angles.

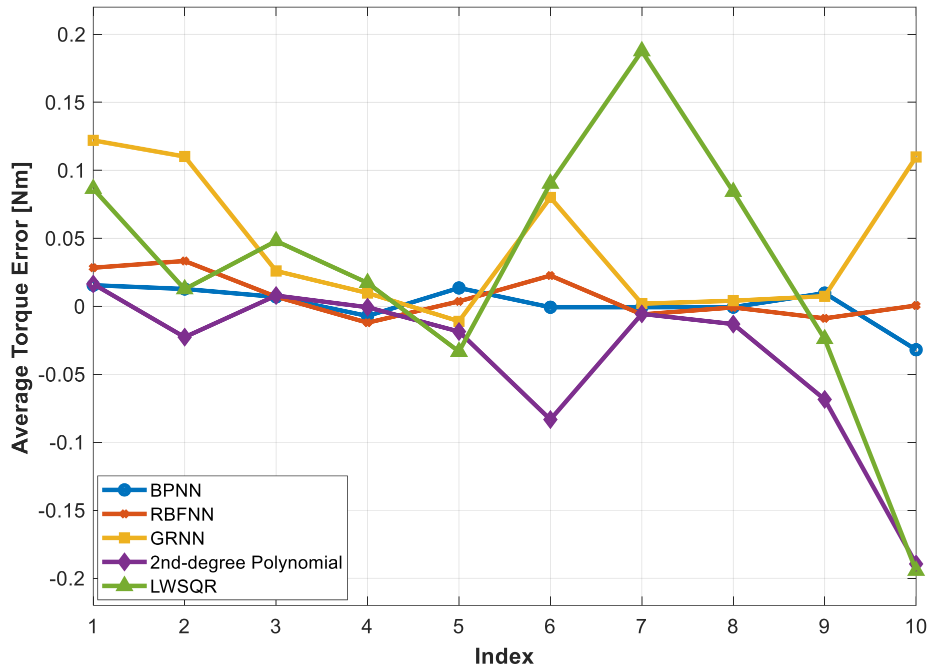

Fig. 4. 13. A comparison of the MLAs and regression techniques for average torque prediction on new data points.

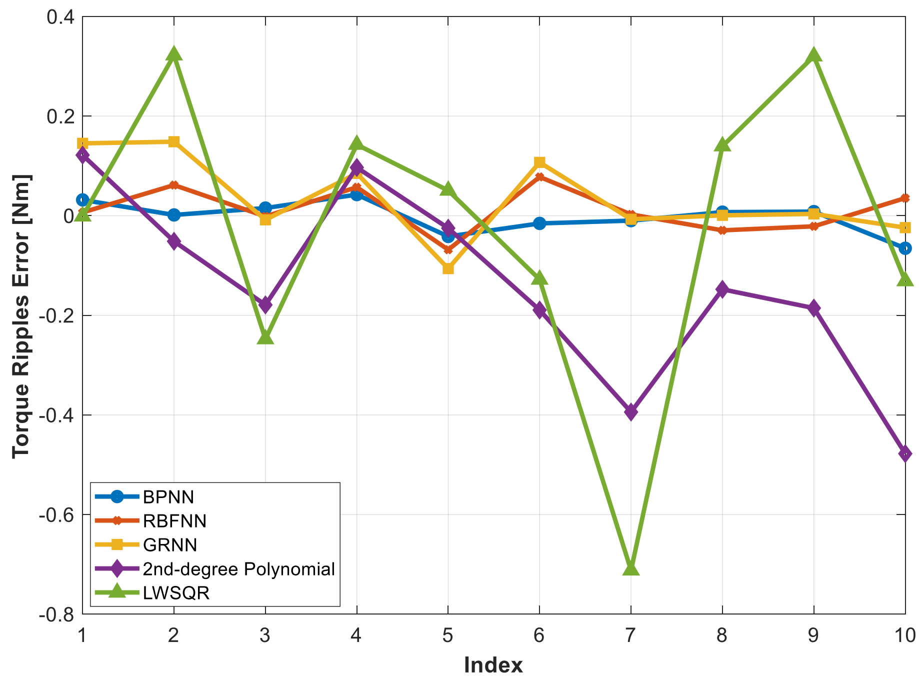

Fig. 4. 14. A comparison of the MLAs and regression techniques for torque ripple prediction on new data points.

In this comparative analysis, we also employ multiple metrics, including MSE, mean absolute error (MAE), and mean relative error (MRE), to assess the fitting performance of the proposed methods. The results of the generalization assessment, presented in Table 4.4, unequivocally confirm that the BPNN outperforms the other surrogate algorithms across all considered metrics.

Table 4. 4. The performance metrics for the generalization dataset of the 3D scatter fitting methods, BPNN, RBFNN and GRNN.

Parameter	2nd-degree Polynomial	Quadratic Regression	BPNN	RBFNN	GRNN
MSE (Nm)	292.0e-4	475.5e-4	5.65e-4	12.0e-4	60.0e-4
MAE (Nm)	0.11475	0.14865	0.0169	0.0242	0.0559
MRE (%)	19.804	25.822	2.244	3.18	6.09

The substantial errors associated with polynomial and quadratic regression approaches highlight their limitations in accurately predicting new data. Particularly, the second-degree polynomial model struggles to capture the highly nonlinear characteristics, leading to significant discrepancies. Additionally, the considerable disparity between training and testing errors in quadratic regression fitting suggests a concern of overfitting. This overfitting problem necessitates a larger training dataset to yield reliable outcomes, potentially resulting in longer simulation times. In contrast, the proposed BPNN showcases its capability to predict new data with remarkable accuracy, even with this small training sample, and without encountering overfitting concerns. While the training and testing outcomes initially favoured the RBFNN as the optimal MLA, the generalization capability test underscores the superiority of the BPNN.

The evaluation of MLAs extends to other crucial aspects, including the structure and computational time during the learning process, particularly focusing on the top two MLAs: BPNN and RBFNN. The BPNN incorporates 8 hidden neurons and outperforms the RBFNN, which houses 10 hidden neurons. Furthermore, regarding the number of epochs needed to complete the training process, the BPNN requires 17, while the RBFNN demands 500 epochs. When weighing aspects like training, testing, generalization capability, structure, and computational time, the BPNN stands out as the overall optimal MLA compared to other developed MLAs. Consequently, the developed BPNN will be used as a surrogate model for the static and dynamic characteristics of the SRM in the remainder of this thesis.

4.5 Summary

In this Chapter, various MLAs were developed to map out the SRM stator and rotor pole arc angles and their dynamic performance, acting as surrogates for static and dynamic analyses. A comprehensive comparison of the developed MLAs, including BPNN, GRNN, RBFNN, and conventional regression fitting algorithms, was conducted. The evaluation framework considered the training results, generalization capability, and learning computational time. While the training results demonstrated comparable performance among the developed algorithms, BPNN proved its capability to predict new data with remarkable accuracy.

Chapter 5

SRM Design Optimization for Torque Improvement Using Machine Learning Algorithms

5.1 BPNN-based Surrogate Model of Average Torque and Torque Ripples

Existing research on geometry optimization of switched reluctance motors (SRMs) using machine learning algorithms (MLAs) has focused only on the machine's static characteristics. The dynamic characteristics, however, are critical to improving the SRM performance, particularly at high speeds. This Chapter introduces an advanced optimization method utilizing a supervised learning algorithm to act as a surrogate model for both static and dynamic characteristics of the SRM. As presented in Chapter 4, a backpropagation neural network (BPNN) is applied to map out the SRM geometrical parameters, stator and rotor pole arc angles and their dynamic performance metrics, such as average torque and torque ripples. In this section, we will briefly revisit and summarize the design and the structure of this BPNN, which are detailed in Chapter 4.

The initial phase of SRM design involves specifying key geometrical parameters. In our investigation, we examine the stator and rotor pole arc angles, which significantly influence motor performance. While wider stator and rotor teeth enhance aligned flux linkage and torque output, excessive adjustments may diminish motor saliency, affecting torque production adversely [20]. Furthermore, the relationship between pole arc angles and torque ripples is highly nonlinear. Hence, careful consideration is essential in designing these angles, underscoring the necessity for a surrogate model to characterize these geometrical parameters precisely.

The motor under study is the 6/14 SRM, and its parameters are previously listed in Table 4.1. The pole arc angles can vary between 8.00° and 12.00°, according to the constraints discussed in Chapter 4, equation 4.1. To demonstrate the influence of varying pole arc angles on the static properties of the SRM, we performed a comparative analysis between the maximum pole arc angles ($\beta_s = 12°$& $\beta_r = 12°$) and minimum pole arc angle angles ($\beta_s = 8.00°$& $\beta_r = 9.14°$) configurations. Fig. 5.1 illustrates the static flux linkage at various current levels for both maximum and minimum pole arc angles. Additionally, Fig. 5.2 presents a comparison of the static torque profiles. The results indicate that widening the pole arcs leads to an increase in the values of the flux linkages. For instance, at 10A, the flux linkage value at the aligned position is 0.38Wb for the largest pole angles, whereas it is 0.27Wb for the smallest angles. Similarly, the expansion of the stator pole arc angles results in a rapid rise in the static torque, as illustrated in Fig. 5.2.

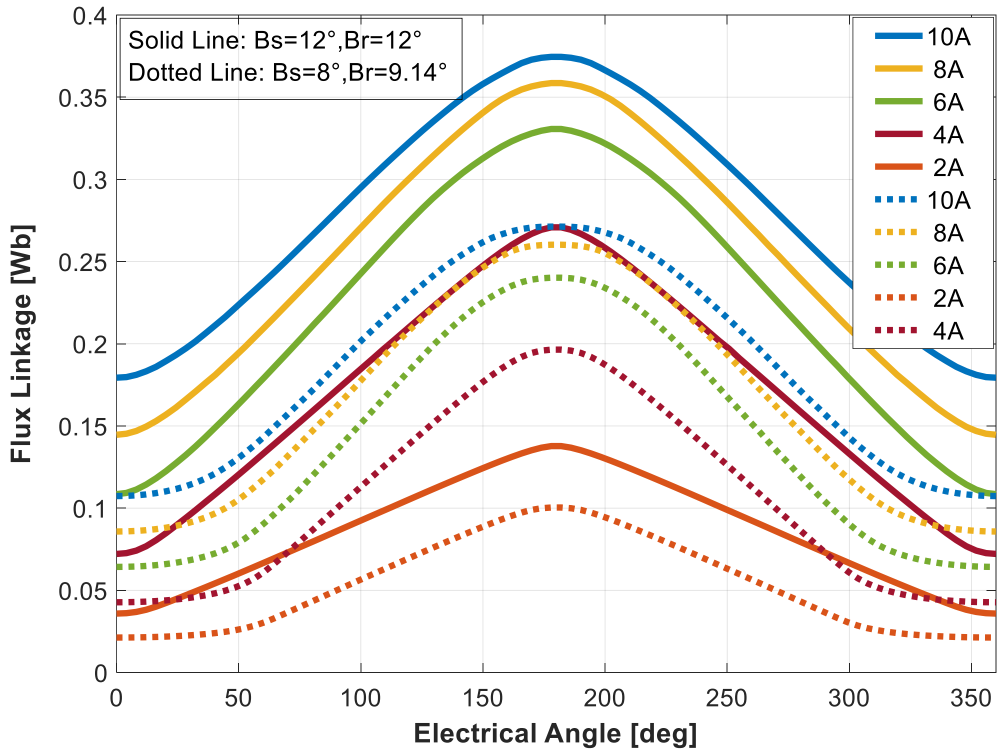

Fig. 5. 1. Static flux linkage comparison between largest and smallest pole arc angles of 6/14 SRM at various phase current levels.

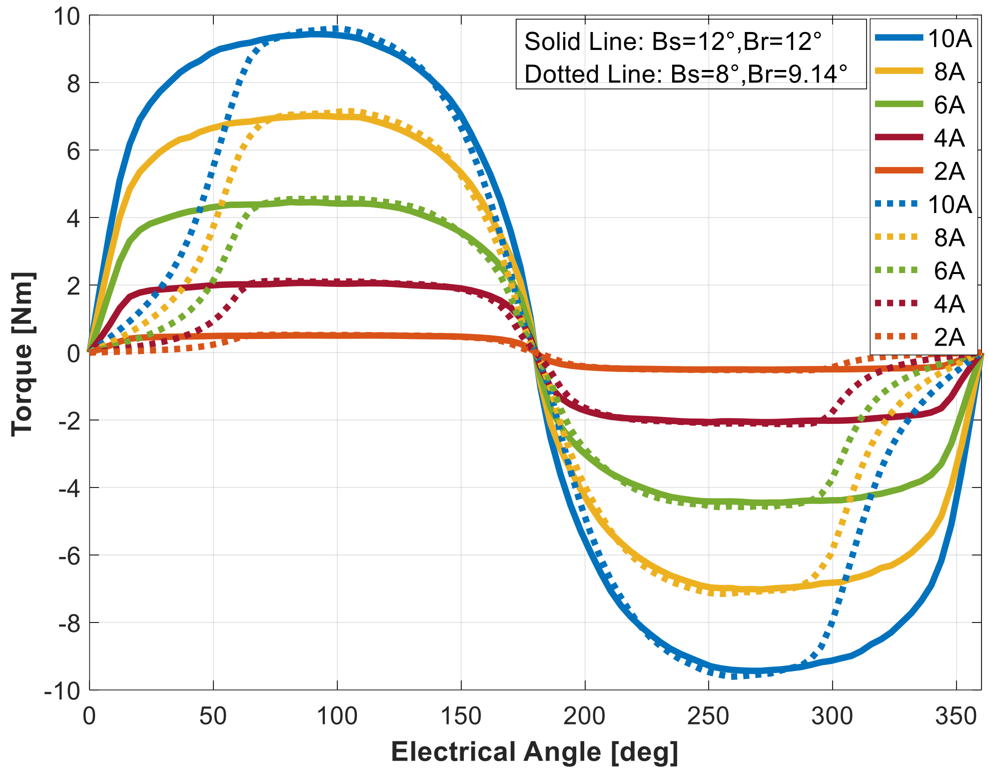

Fig. 5. 2. Static torque profiles comparison between largest and smallest pole arc angles of 6/14 SRM at various phase current levels.

Similarly, the pole arc angles impact the SRM dynamic characteristics of SRMs. We compare the dynamic analysis results between configurations with β_s =12° and β_r =12° and those with β_s =8° and β_r =9.14°. Fig. 5.3 visually represents the total dynamic torque, with blue indicating the largest stator and rotor pole arc angles and red representing the lowest arc angles. The increase in static torque, as shown in Fig. 5.2, is reflected in the total dynamic torque. The average torque for the largest pole angles is 4.95Nm, while for the lowest angles, it is 4.47Nm. Additionally, RMS torque ripple values are derived from the dynamic model, with 0.653Nm for the largest angles and 0.548Nm for the lowest angles.

These results highlight the nonlinear correlation between average torque and torque ripples with variations in pole arc angles, emphasizing the necessity for accurate function approximation to depict these relationships.

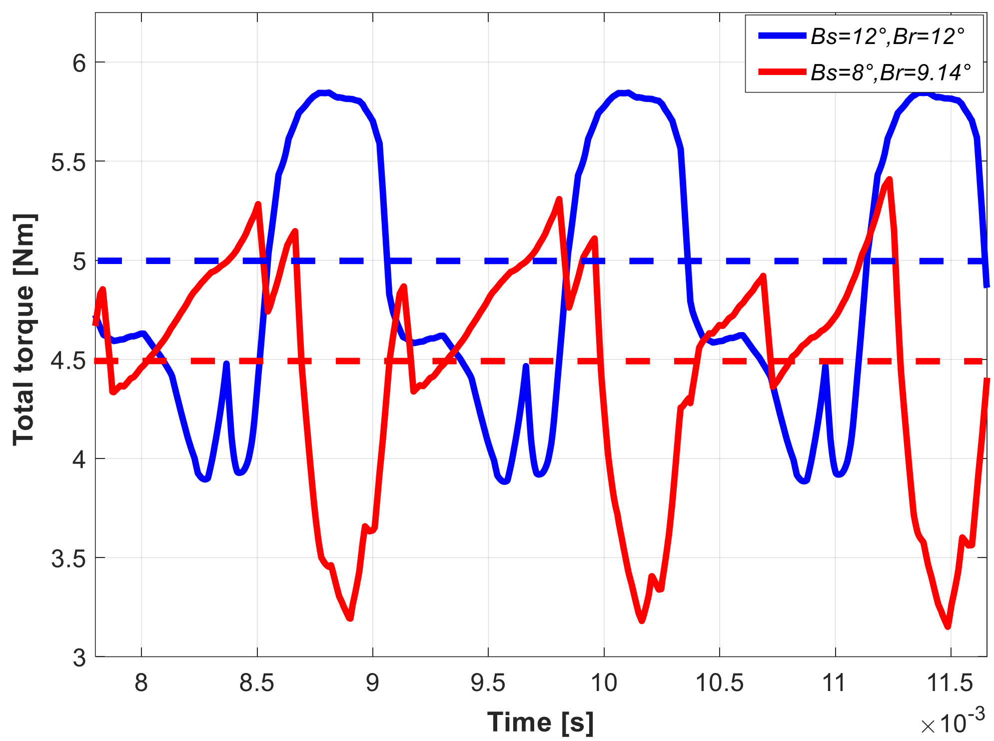

Fig. 5. 3. Dynamic torque comparison between configurations with β_s =12° and β_r =12° and those with β_s =8° and β_r =9.14°.

To capture the training data, 50 design candidates, a parametric sweep was conducted for the pole arc angles while considering the previously mentioned constraints. FEA analysis was carried out, and the static characteristics LUTs were imported to the SRM dynamic model. For each design candidate, the conduction angles were optimized using the GA to achieve maximum average torque. Therefore, the trained MLA not only acts as a surrogate for the FEA analysis but also for the dynamic model, including the GA optimization of the conduction angles.

According to the comprehensive assessment of the BPNN, RBFNN, and GRNN presented in Chapter 4, the BPNN proved to be superior. Consequently, the BPNN has been employed in this thesis. The architecture of the proposed BPNN, as depicted in Fig. 4.8, includes a single hidden layer with eight neurons utilizing the Tansig activation function. This structure was chosen heuristically to balance training accuracy and model complexity. The Levenberg-Marquardt (LM) algorithm was applied as the optimization method for training the proposed BPNN. The training dataset, comprising 50 points, was partitioned into 70% for training, 15% for validation, and 15% for the testing set. LM-BPNN managed to finish the training process in 17 epochs. The training, testing and generalization assessment are shown in Tables 4.2 and 4.3. These results demonstrate the high accuracy of the designed BPNN in predicting new data points, validating its capability for effective generalization without encountering overfitting or underfitting issues.

5.2 Estimation and Selection of Optimal Design Candidates

Following the training and evaluation of the BPNN, it was utilized to generate 10,000 new design candidates that were not previously utilized for network training or testing. The BPNN's outcomes are visualized in a 2-D plane, as shown in Fig. 5.4, where the objectives, namely the average torque and the torque ripples, are plotted for each design candidate. From the results obtained, two design candidates, identified as DC1 and DC2, were chosen as optimal candidates, as shown in Fig. 5.4. DC1 has the highest average torque, whereas DC2 has the lowest torque ripples. The design variables and the performance objectives of the optimized design candidates are compared to the baseline design. The comparison outcomes are presented in Table 5.1.

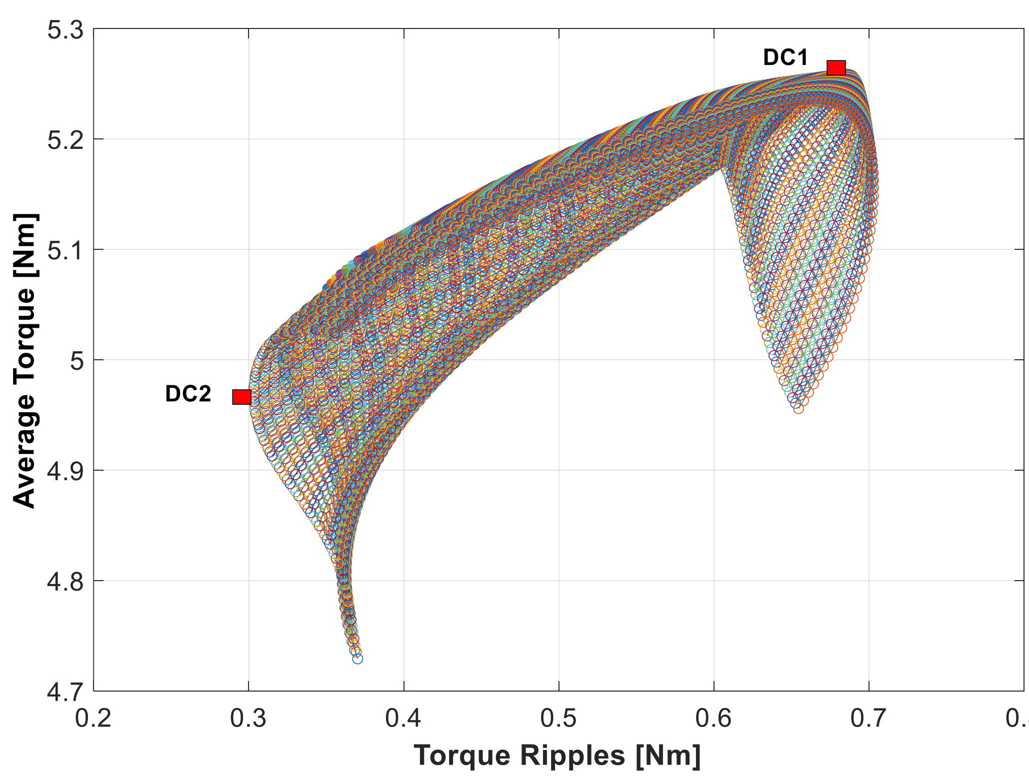

Fig. 5. 4. A scattered 2–D plane showing the objective outputs of 10,000 design candidates generated by the trained BPNN. The two recommended designs are identified as DC1 and DC2.

Table 5. 1. The design variables and performance objectives of the baseline and optimized design candidates

Parameter	Baseline	DC1	DC2
β_s [°]	9.5	10.8788	9.00
β_r [°]	9.3	11.1212	10.7273
Average torque [Nm]	4.88	5.2585	4.9687
Torque ripples RMS [Nm]	0.398	0.6857	0.3032

Static and dynamic simulations were carried out using the optimal values of the pole arc angles to verify the estimated output of the neural network. The actual values of the average torque and torque ripples were compared to the BPNN estimated values, as shown in Table 5.2. The relative error of the average torque of DC1 and DC2 is 0.05% and 0.36%, respectively. Also, the relative error of the RMS torque ripples of DC1 and DC2 is 2.10% and 0.03%, respectively. These extremely low error values reflect the precision of the proposed BPNN model.

Table 5. 2. The actual and estimated values of the average torque and torque ripples of the optimized design candidates

Parameter	DC1		DC2	
	BPNN	Actual	BPNN	Actual
Average torque [Nm]	5.2585	5.2610	4.9687	4.9865
Torque ripples [Nm]	0.6857	0.6716	0.3032	0.30329

5.3 Analysis of Optimal Design Candidates

To investigate BPNN-estimated design candidates, FEA JMAG models of DC1 and DC2 were simulated using their proposed pole arc angles. Fig. 5.5 illustrates the partial cross-sectional models of the baseline and optimized design candidates. The static torque profiles of DC1 and DC2 compared to the baseline at different phase currents are shown in Fig. 5.6 and Fig. 5.7, respectively. Whereas the dynamic torque output for a complete electrical cycle of both design candidates is displayed in Fig. 5.8 and Fig. 5.9. Notably, enlarging the stator pole arc angles in DC1 causes a fast rise for the static torque profile. Thus, the total motor torque output from the dynamic Simulink model is increased, as shown on the blue graph in Fig. 5.8.

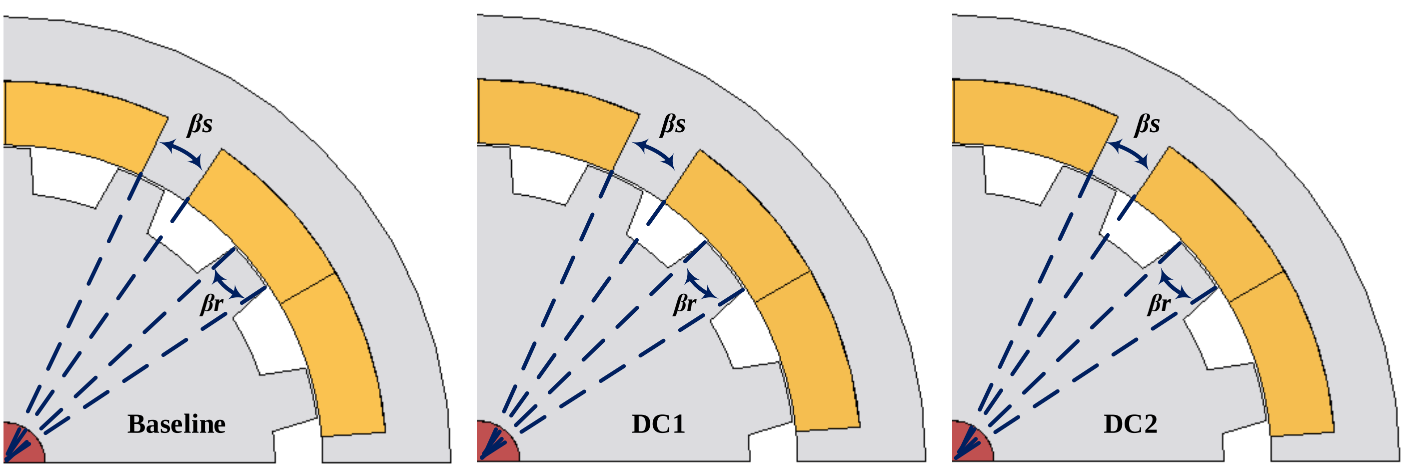

Fig. 5. 5. FEA JMAG partial model of the baseline and the optimized design candidates.

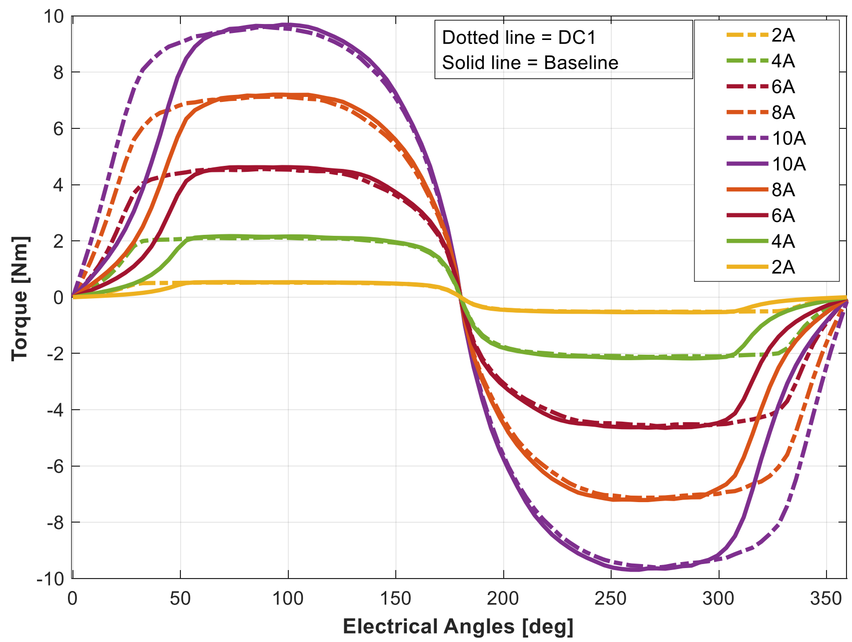

Fig. 5. 6. A comparison of static torque profiles between DC1 and baseline at various phase currents.

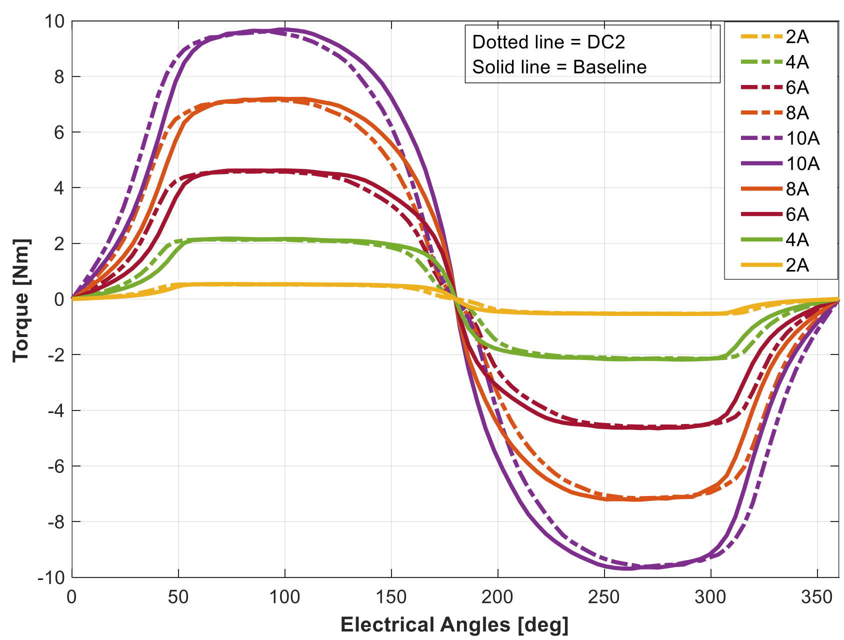

Fig. 5. 7. A comparison of static torque profiles between DC2 and baseline at various phase currents.

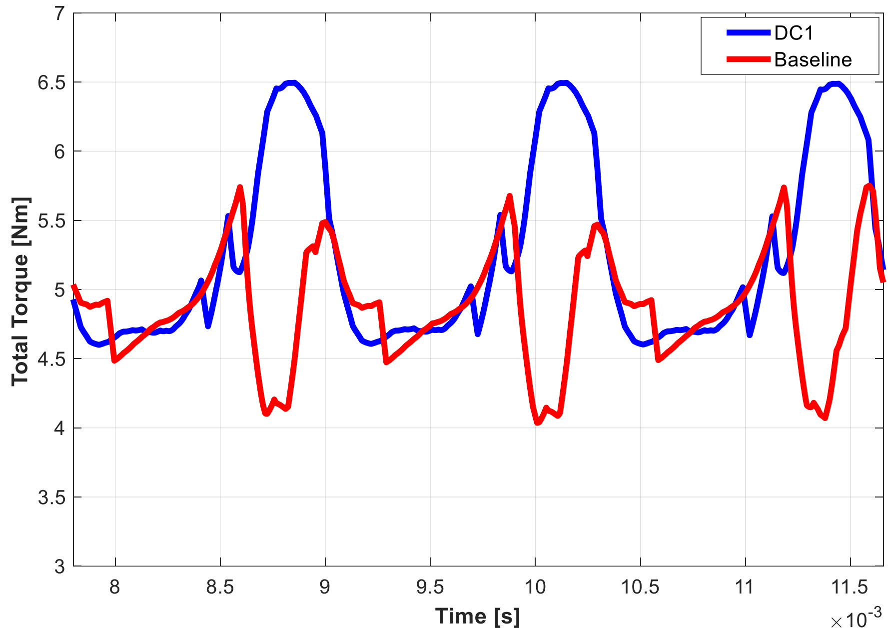

Fig. 5. 8. Total torque of DC1 for one electrical cycle compared to the baseline.

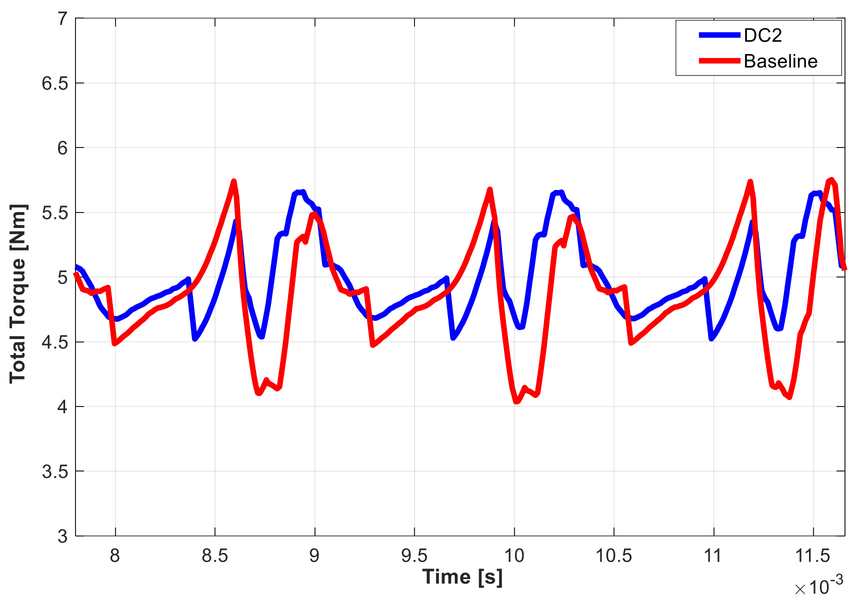

Fig. 5. 9. Total torque of DC2 for one electrical cycle compared to the baseline.

In addition to the analysis of the static behavior of the optimized design candidates, we also assessed their dynamic characteristics, particularly the optimization of conduction angles, to validate the performance of the BPNN output. In DC1, the optimized turn-on angle of the current is more advanced than in DC2, as indicated in Table 5.3. Advancing the turn-on angle leads to injecting the current before the build-up of the induced voltage, resulting in an increase in the total average torque produced. Thus, DC1 experienced higher average torque than DC2. Although DC1 recorded the highest average torque, it also exhibited a greater value of RMS torque ripples. Because the conduction angle optimization is a single-objective process aimed at maximizing the average torque, even if it comes at the expense of higher torque ripples. Evidently, the proposed BPNN accurately surrogated the optimization process of the conduction angles, saving significant computational time.

Table 5. 3. The conduction angles of baseline and optimized design candidates.

Conduction Angles	Baseline	DC1	DC2
Turn ON, θ_{on} [°]	-30.5	-36.9	-29.2
Turn OFF, θ_{off} [°]	137.47	131.1	138.7

In SRMs with a larger number of rotor poles, proximity between the poles results in flux leakage to adjacent poles during phase energization. As the adjacent pole experiences a declining inductance profile, it is reasonable to anticipate a negative torque output [20]. This leads to increased torque ripples, negatively impacting the motor's torque quality. To address this issue, one solution is to widen the rotor-pole arc angle compared to the stator-pole arc angle. This intentional difference introduces dead time in the inductance profile during turn-off delay, preventing potential negative torque during phase conduction and promoting self-starting capabilities [110]. In this study, both design candidates, DC1 and DC2, demonstrate a larger rotor pole arc angle compared to the stator pole arc angle. However, the difference between β_r and β_s in DC2 is significantly greater than in DC1. This increases the dead zone in the middle of the static torque waveform in DC2 compared to DC1, as shown in Fig. 5.6 and Fig. 5.7. This eliminates the negative torque production and hence reduces the torque ripples more effectively in DC2 compared to the baseline and DC1 designs. Consequently, by reducing the torque ripples, the overall torque quality is improved, leading to a reduction in audible noise generation from the SRM.

The recommended designs meet the arc angles constraints and are deemed as effective solutions with respect to the output performance of the considered SRM. However, since both design candidates exhibited an average torque slightly higher than the baseline, the selection of the best candidate was prioritized based on its output torque ripples. Consequently, DC2 was selected as the most optimal design candidate as it exhibited an average torque enhancement of 2.2% and a remarkable reduction of torque ripples by 23.8% when compared to the baseline design [111].

The utilization of MLA in motor design offers numerous benefits, such as a reduction in computational overhead. This approach effectively acts as a surrogate model for static and dynamic simulations, including the optimization process of the conduction angles. As a result, it leads to significant savings in computational time. To quantify the amount of time saved, we calculated and recorded the execution time of all the steps involved in obtaining the design candidates. It took a total of 2,000 minutes to obtain the 50 data points comprising the training dataset. Each individual data point necessitates 25 minutes to execute the static FEA model and generate the required lookup tables. Additionally, the MATLAB Simulink model, which includes the GA optimization of conduction angles, consumes 15 minutes for each data point. Then, the proposed method took approximately 10 minutes to learn the training data and generate 10,000 new data points. The studies presented in this work were conducted using a computer equipped with an Intel(R) Core (TM) i7-8700 CPU running at a speed of 3.20GHz and 32.0 GB of RAM. In comparison, using the conventional FEA and MATLAB method to get 10,000 points would take 400,000 minutes, which is a formidable computational cost. Therefore, the proposed method offers significant execution time savings.

5.4 Summary

In this Chapter, we proposed a non-conventional optimization approach utilizing the BPNN to accurately map out the crucial SRM geometrical parameters, stator and rotor pole arc angles and their dynamic performance, including average torque and torque ripples. The developed BPNN acts as a surrogate model, replacing both static and dynamic models, including GA optimization of the conduction angles. To enhance the training process, LM algorithm was implemented, ensuring efficient and rapid convergence while reducing network complexity. Using the developed approach, 10,000 design candidates for the considered 6/14 SRM were obtained. The optimal design was rigorously validated with high precision using FEA and Simulink analysis, establishing its reliability and superior performance. This proposed method showcases an improvement of 2.2% in the motor average torque and a remarkable reduction of 23.8% in torque ripples compared to the baseline design. Additionally, this method significantly reduced computational time, and costs compared to conventional iterative techniques.

Chapter 6

Modeling and Analysis of SRM Radial Forces Using Machine Learning Algorithms

6.1 Radial Force Density

In electric machines, sources of acoustic noise and vibration can be categorized into four main types: electromagnetic (including radial forces, switching action, and torque), mechanical (such as bearing and friction), electromechanical (eccentricity), and aerodynamic (rotor and fan) [1]. This Chapter focuses on a detailed examination of radial forces in SRMs. Radial forces are generated in an SRM when magnetic flux crosses the air gap. These forces cause deformation of the stator core, which in turn contributes to acoustic noise and vibration in the SRM [1]. Moreover, when the radial force harmonics frequencies coincide with the natural frequencies of the stator core for a specific mode shape, resonance happens, leading to amplified vibration and noise levels.

Therefore, motor designers should consider the reduction of radial force harmonics when optimizing the motor geometry. Radial forces constitute one of the critical objectives that should be addressed alongside average torque, efficiency, and torque ripple. Accurate modeling is a prerequisite for optimizing motor geometry to reduce radial forces and mitigate their adverse effects on vibrations and noise. Hence, this Chapter delves into the modeling of radial forces and the decomposition of their harmonic components. Furthermore, it presents a machine learning algorithm (MLA)-based surrogate model for the most influential radial force harmonic components, facilitating the integration of radial force reduction into a multi-objective optimization framework.

When the SRM stator poles are exposed to electromagnetic forces, they vibrate. The resulting pressure is referred to as force density, which is decomposed into radial and tangential force densities, as shown in Fig. 6.1. These forces can deform the stator core, leading to structural vibration. Notably, radial forces are the primary contributors to acoustic noise in the radial flux inner rotor SRM, which constitutes the central focus of this thesis.

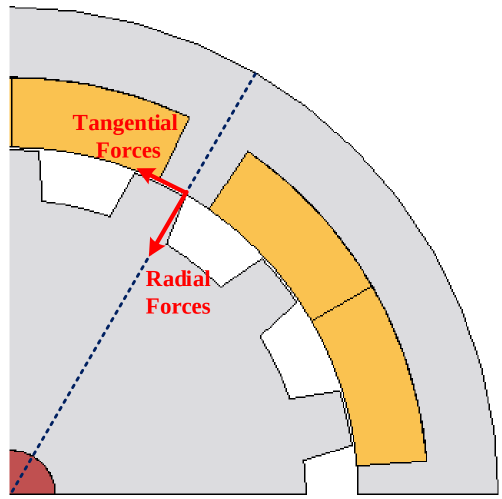

Fig. 6. 1. Stator's electromagnetic forces components.

The electromagnetic radial force density, or the electromagnetic radial pressure, is defined as the force per unit area, and its unit is lbs/in^2 or N/m^2. The radial force components can be evaluated using the FEA models and then decomposed into their harmonics. The flux solution of the FEA model can be used to evaluate the radial force density F_d of the SRM machine using the Maxwell stress tensor as follows [112],

$$F_d(t,\theta) = \frac{1}{2\mu_o}[B_r^2(t,\theta) - B_t^2(t,\theta)] \ , \tag{6.1}$$

where t is the time step, θ is the airgap spatial position, B_r is the radial component of the flux density, B_t is the tangential component of the flux density, and μ_o is the air permeability. As can be noted from equation (6.1), the radial force density wave is characterized as a travelling wave that has time and spatial dimensions.

The stator radial forces are evaluated using FEA by exciting the coils with dynamic current waveforms. The dynamic model, discussed in Chapter 4, is simulated at the base speed for one complete electrical cycle, and the resulting dynamic current waveform is down-sampled and imported into the FEA model of the SRM. This approach significantly reduces the computational time compared to implementing the voltage source and power electronics converter directly within the FEA model. Fig. 6.2 illustrates the simulation loop for this process. Fig. 6.3 depicts the dynamic current waveform obtained through this approach. It is worth noting that the calculated radial forces depend on the SRM control parameters, which were already considered during the simulation of the dynamic current waveform. Fig. 6.4 shows a typical radial force wave along the stator's inner circumference, resulting from exciting the coils with the dynamic current waveform.

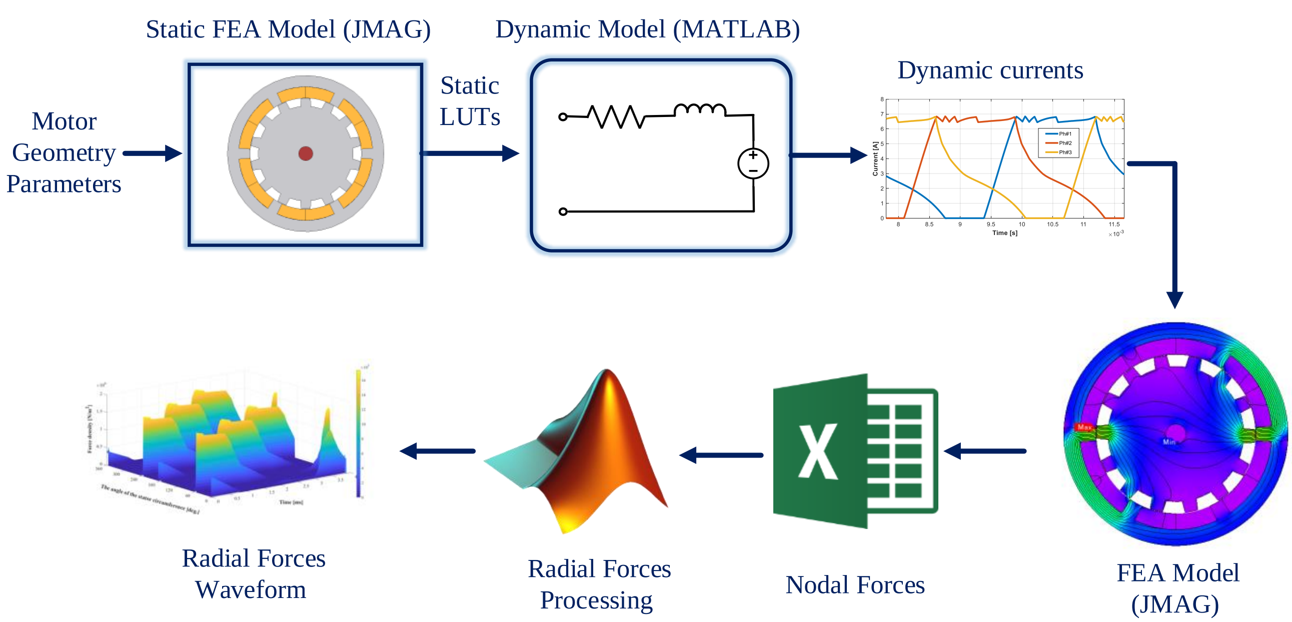

Fig. 6. 2. The simulation steps for radial forces waveform evaluation.

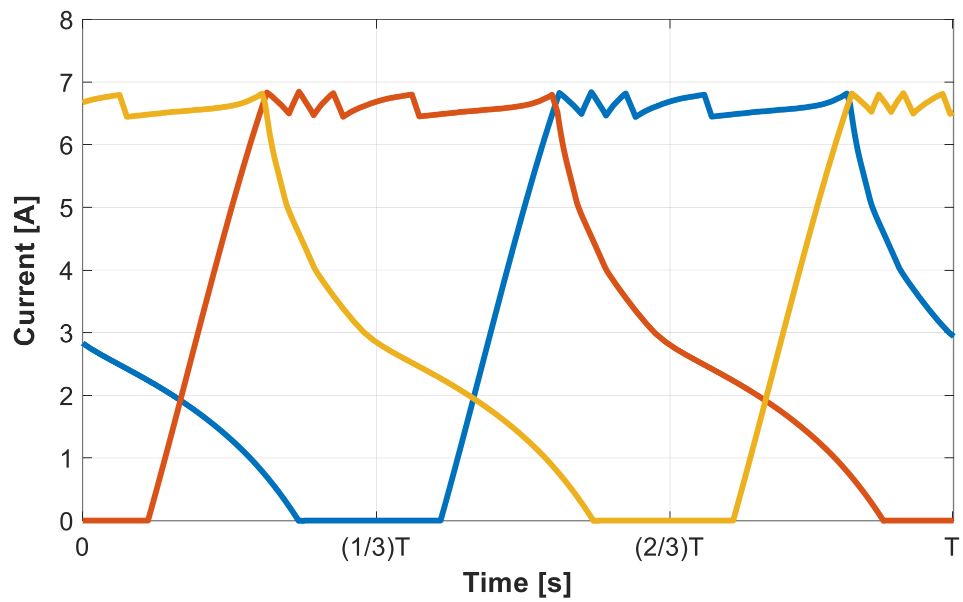

Fig. 6. 3. The three-phase dynamic current waveforms used to obtain the baseline design's radial forces.

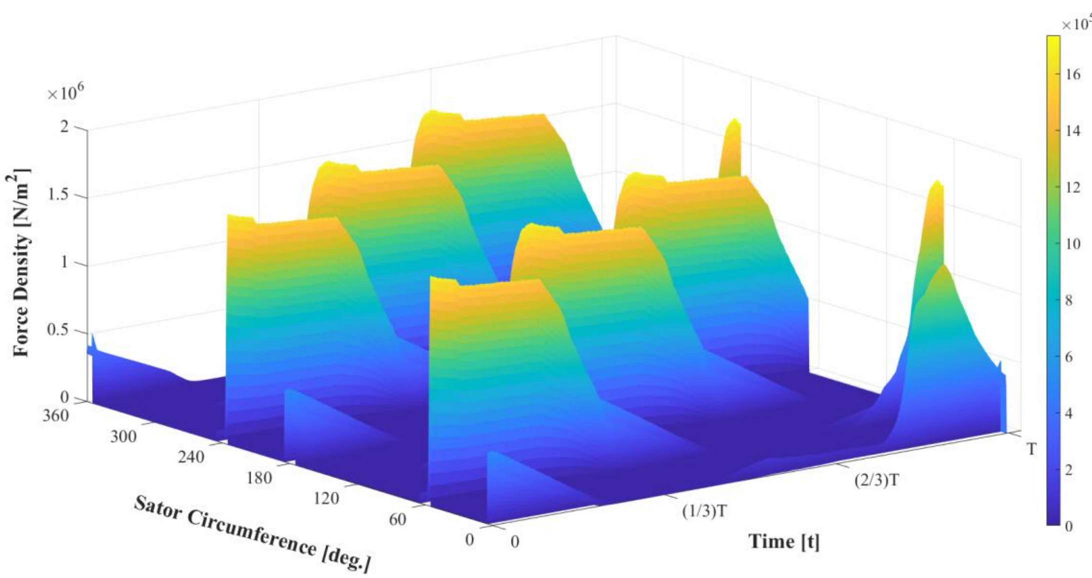

Fig. 6. 4. The stator radial force density waveform for the baseline design of considered SRM (6/14SRM) for one electrical cycle (T).

Exploiting the periodicity of SRMs, the nodal force computed in the FEA is simulated for $1/m$ of the electrical cycle, where m represents the number of the phases. This methodology, outlined in [112], was employed in this research to minimize the necessary rotor steps for acquiring the radial force density waveform.

6.2 Decomposition of Radial Force Density

The radial force density waveform in an SRM can be characterized as a travelling wave in a cylindrical shell, indicating its variation over time, circumferential position, and axial position along the motor. However, this study disregards the axial deformation that the radial force density may cause for simplification purposes. Instead, the analysis focuses on the time and spatial domains, necessitating a two-dimensional approach.

Consequently, the radial force density can be decomposed into spatial (circumferential) and temporal (time) harmonic components. This decomposition is achieved through the application of a two-dimensional fast Fourier transform (2D FFT), which computes the harmonic spectrum of the stator's radial force density for the case study machine across various geometrical configurations. Decomposing the radial force density into its constituent harmonic components makes it possible to analyze and mitigate the effects of specific harmonics that may contribute significantly to vibrations and acoustic noise. This harmonic analysis provides valuable insights for optimizing the motor design and minimizing the adverse impacts of radial forces.

The spatial harmonics of the radial force density are characterized by their circumferential order, v. Similarly, the temporal harmonics are identified by their mechanical temporal order, u, corresponding to the frequency of the harmonic relative to the fundamental frequency of the motor's rotation. The forcing frequency of spatial or temporal harmonic contents is expressed as follows:

$$f_{f(u,v)} = |u| N_r f_{mech} = |u| N_r \frac{RPM}{60} [Hz] \tag{6.2}$$

where N_r is the number of rotor poles, f_{mech} is the mechanical frequency of rotor and RPM is the motor speed.

The SRM pole configurations and the phase excitation sequence have an impact on the radial force harmonics pattern [113]. The motor under investigation is a 3-ph 6/14 SRM. Therefore, there are two stator teeth per phase; hence, two groups of radial force vectors act on the stator. Also, the circumferential orders of the radial force harmonics will be multiples of 2. Generally, the time and spatial orders of any radial force harmonic components can be expressed by [113]:

$$\begin{cases} u = N_r \times m \times j - N_r \times k \\ v = \dfrac{N_s}{m} k \end{cases} \tag{6.3}$$

where *j* and *k* are integer values [113]. For the 6/14 SRM, this formula is expressed as:

$$\begin{cases} u = 14 * 3 \times j - 14 \times k = 42 \times j - 14 \times k \\ v = \dfrac{6}{2} k = 2 \times k \end{cases} \tag{6.4}$$

Equation (6.4) defines the position of each radial force harmonic component and the dominant harmonic orders of 6/14 SRM. Fig. 6.5 shows the amplitudes of the harmonic components of the radial force density of the initial design of 6/14 SRM.

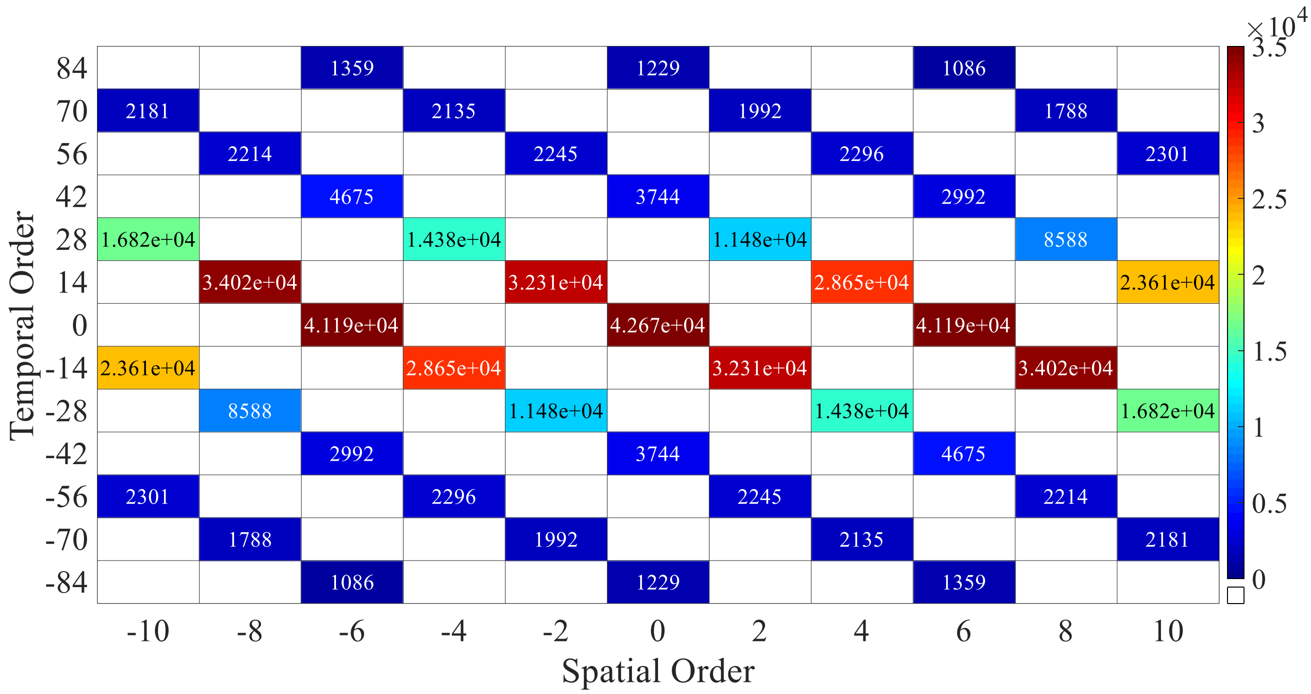

Fig. 6. 5. The stator radial force density components of the initial design of the 6/14 SRM.

6.3 MLA-based Surrogate Model of The Radial Forces Density Components

As presented in this Chapter, modeling the radial forces is complicated and necessitates heavy time-consuming FEA and dynamic analysis simulations. Moreover, the motor design optimization process requires repetitive invocations of FEA and dynamic simulations for any variations in the geometrical parameters. Therefore, developing a surrogate model for radial forces is crucial to reducing the repetitive effort and computational time, enabling an efficient multi-objective optimization framework for SRM enhancement. This endeavor aims to establish a comprehensive multi-objective environment capable of enhancing overall motor performance, as discussed in Chapter 7.

The optimal approach for mitigating acoustic noise and vibration in SRM involves identifying the most critical force density components through modal analysis and subjecting these components to optimization, as detailed in [1]. Typically, selecting dominant radial force harmonics requires analyzing the natural frequencies of the motor structure to identify potential resonance conditions [113]. However, the present study does not incorporate modal and acoustic noise analyses. Instead, the selection of the most significant radial force components was based on their amplitudes at circumferential vibration mode 2 and mode 4.

Fig. 6.6 shows the circumferential modes from mode 0 to 5 of the stator of radial flux SRMs. For SRMs with two stator poles per phase, the most dominant harmonic mode is mode 2 [116],[117]. Additionally, as outlined in [117], the modes 1-4 are significant for small machines. Therefore, two radial force components with the highest amplitudes in the 2nd and 4th spatial orders denoted as $F_d(u=14, v=2)$ and $F_d(u=14, v=4)$, were chosen for the optimization process in this study.

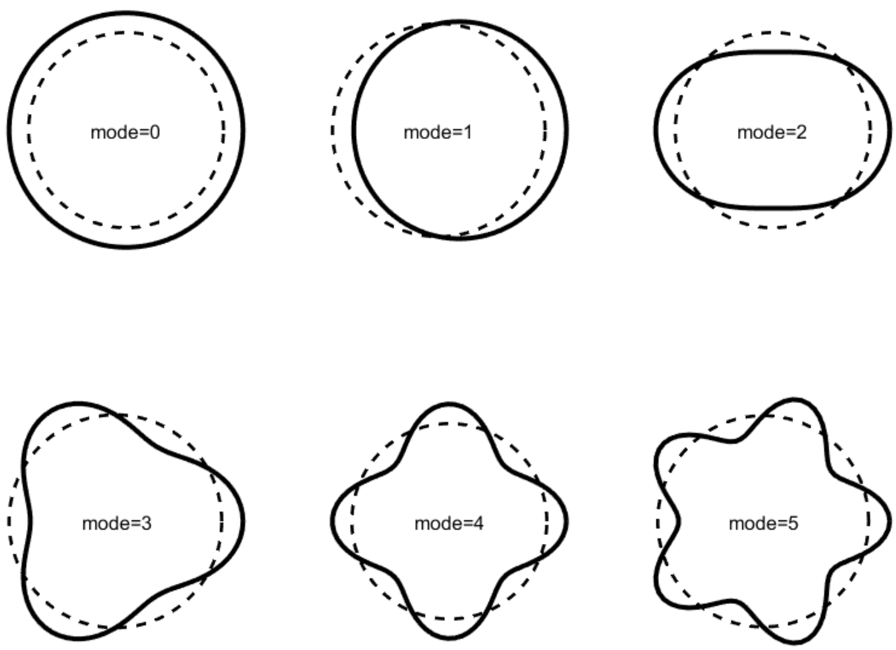

Fig. 6. 6. The circumferential mode profiles from modes 0 to 5 of the stator of radial flux SRMs.

To obtain the training dataset, the pole arc angles were varied 50 times within the specified minimum and maximum limits. The look-up tables (LUTs) of the static properties were computed using JMAG software and applied to the dynamic model to determine the SRM's dynamic current at the base speed. This dynamic current waveform was then imported into the FEA model, and the nodal forces were computed along the stator's bore diameter. A 2D-FFT was applied to get the radial force harmonic content. For each design candidate, the radial force components denoted as $F_d(u=14, v=2)$ and $F_d(u=14, v=4)$, were recorded as the target outputs for the developed MLA. Of the 50 data points generated, 34 were allocated for training the MLA, while the remaining points were used for testing and validation. Table 6.1 lists 5 data points as an example from the training dataset.

Table 6. 1. A subset of the training data utilized for the MLA to model the radial force harmonic components.

β_s [°]	β_r [°]	Radial force harmonic amplitude at $F_d(u=14, v=2)$ [N/m^2]	Radial force harmonic amplitude at $F_d(u=14, v=4)$ [N/m^2]
8.5	9	29210.43	26287.76
9	9	30431.51	27082.22
9	10	33266.46	29531.65
9.5	9	30366.09	26911.82
9.5	10	34098.37	29941.23

To maintain consistency with the analysis outcomes from Chapter 4, a back-propagation neural network (BPNN) was employed as a surrogate model for the dominant radial force harmonic components under variations in pole arc angles. The BPNN architecture comprised a single hidden layer with ten neurons to achieve the highest accuracy. The pole arc angles are fed to the input layer while the output layer predicts the most significant radial forces density harmonics at circumferential orders 2 and 4. Training of the neural network was conducted using the LM algorithm, completing the process in just 3 epochs. The architecture of this model is illustrated in Fig. 6.7, while error convergence curves in relation to the number of epochs are displayed in Fig. 6.8.

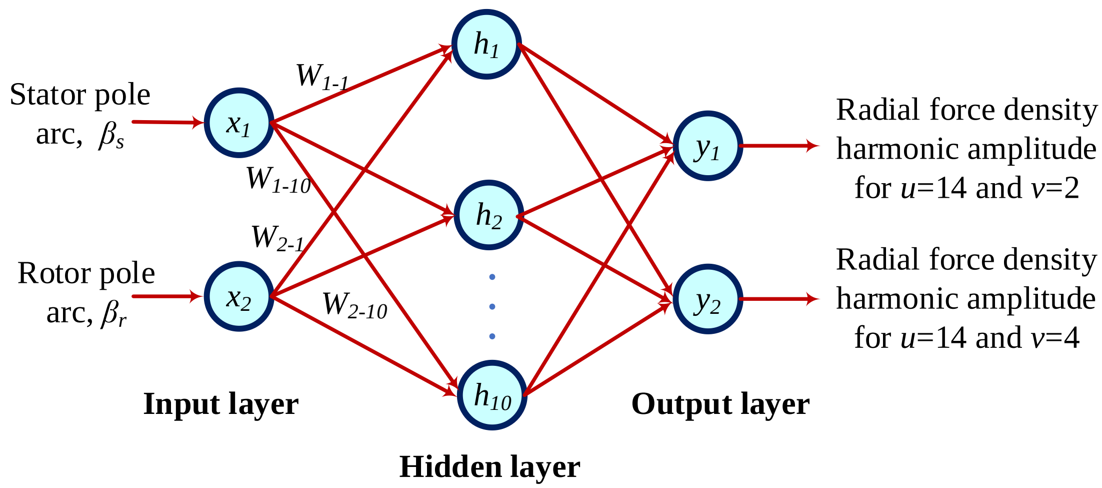

Fig. 6. 7. The BPNN-based surrogate model represents SRM radial forces density components.

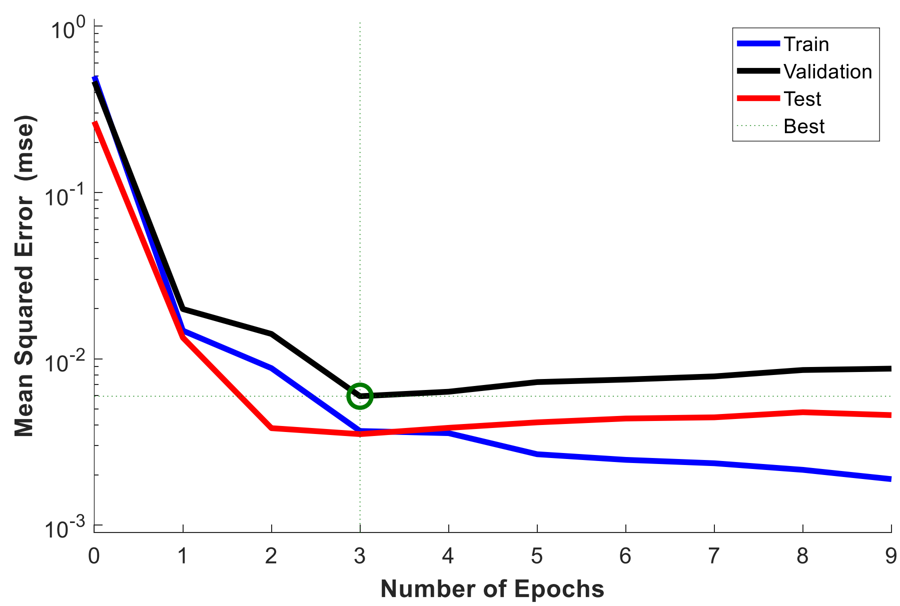

Fig. 6. 8. The training, testing, and validation profiles of the BPNN-based surrogate model of the SRM Radial forces.

The training and testing results of the proposed BPNN are outlined in Table 6.2. Generalization capability was verified with ten new data points not used in the training and testing phases. Performance metrics are summarized in Table 6.2, with the MRE of this generalization dataset at 1.48%. These minor errors confirm the high accuracy of the designed BPNN-based surrogate model.

Table 6. 2. The training and testing results of the BPNN-based surrogate model for the SRM radial forces density

Performance Index	Training Dataset	Testing Dataset	Generalization Dataset
MSE (Nm)	3.6787e-3	3.5236e-3	4.7871e-3
R-squared	0.98863	0.9823	0.94065

6.4 Summary

In SRMs with an inner rotor configuration, radial forces generated due to magnetic flux crossing the air gap can cause deformation of the stator core, leading to acoustic noise and vibration. Consequently, motor designers aim to mitigate these radial forces acting on the stator. This work evaluates stator radial forces using FEA by exciting the coils with dynamic current waveforms obtained from a simulated dynamic model. The radial force density is then decomposed into spatial and temporal harmonic components using a 2D FFT. This harmonic decomposition enables the analysis and targeted mitigation of specific harmonic components that contribute significantly to vibrations and acoustic noise.

However, repeatedly performing these simulation procedures to optimize the motor geometry can be computationally intensive. To address this challenge, this Chapter presents the development of an accurate surrogate model using a BPNN to replace the FEA and dynamic simulations, significantly reducing the repetitive effort and execution time. The architecture, training, and testing results of the developed BPNN are illustrated.

The primary objective of the proposed BPNN-based surrogate model is to estimate the amplitudes of the dominant radial force harmonic components, which can then be integrated into a multi-objective optimization algorithm. This approach aims to enhance the overall performance of the SRM by optimizing the motor geometry while considering the radial force harmonics as one of the objectives, as discussed in Chapter 7.

Chapter 7

Multi-objective Design Optimization Framework of SRM Using Machine Learning Algorithms

Switched reluctance motors (SRMs) feature a straightforward and robust design characterized by the absence of permanent magnets or rotor windings, facilitating elevated operating temperatures and minimizing manufacturing expenses [114]. The stator winding of SRMs typically employs a concentrated winding configuration, resulting in reduced machine assembly and maintenance costs. Additionally, this winding design minimizes the magnetic coupling between the phases, thereby enhancing the fault tolerance of SRMs [115]. However, SRMs present challenges such as significant torque ripples, acoustic noise, and vibrations attributed to their salient pole configuration [6]. In inner rotor SRM configurations, the radial force density acting on the stator leads to its deformation and subsequent vibration and noise generation [7].

SRM challenges can be effectively addressed through a comprehensive motor design. The process of designing motor geometry entails the fine-tuning of machine parameters, typically accomplished through a combination of experience and heuristic approaches. This often involves using finite element analysis (FEA) software to simulate the effects of different parameter adjustments [8]. However, this approach does not ensure the acquisition of the optimal design [9] and requires long execution times [10],[11]. Therefore, developing an accurate surrogate model using machine learning algorithms (MLAs) to replace FEA simulations would significantly save repetitive effort and execution time [12].

In Chapter 5, a back-propagation neural network (BPNN) was developed to provide a surrogate model for the FEA and dynamic Simulink model of the 6/14 SRM, considering the optimization of conduction angles. This surrogate model accurately established the correlation between variations in pole arc angles and the average torque and torque ripples. However, addressing acoustic noise and vibrations is imperative for establishing SRMs as a robust alternative to conventional motors. Consequently, Chapter 6 presented the development of a surrogate model using the BPNN for the most dominant radial force harmonic components. In conjunction with the previously developed BPNN-based surrogate model (discussed in Chapter 5), this endeavour aims to establish a comprehensive multi-objective optimization framework. This framework is designed to enhance the overall performance of the SRM by simultaneously optimizing the average torque, torque ripples, and radial force harmonic amplitudes, as discussed in this Chapter.

7.1 Genetic Algorithm Application for Optimal Design Selection

In this Chapter, a genetic algorithm (GA) is employed to optimize the design parameters of the considered SRM, focusing on enhancing its performance characteristics. Specifically, the optimization aimed to determine the optimal values of the SRM pole arc angles, which minimizes the torque ripples, improves the average torque, and reduces the radial forces acting on the stator. To accomplish this, we employed MATLAB's GA optimizer, incorporating a fitness function that integrates trained neural networks. As discussed in earlier Chapters, these neural networks were trained to estimate the SRM's torque characteristics and radial forces. To ensure a thorough exploration of the design space, the following linear constraints were utilized to establish realistic bounds on the parameters:

$$\beta_s \in [8°,12°] \tag{7.1}$$

$$\beta_r \in [8°,12°] \tag{7.2}$$

The fitness function utilized the two previously trained BPNNs: one for predicting the average torque and torque ripple and another for predicting the radial forces density components. The fitness function evaluated the performance of the design parameters based on predetermined criteria: the torque ripple should be minimized, the average torque should exceed that of the baseline design, and the most dominant radial force density components should be lower than those of the baseline,

Objective:

$$f_{obj} = \min(\Delta T_{RMS}) \tag{7.3}$$

Subject to:

$$T_{avg} \geq T_{avg,baseline} \tag{7.4}$$

$$F_d < F_{d,baseline} \tag{7.5}$$

If the design parameters fail to meet these criteria, the fitness function assigns penalty values to the objective function to discourage infeasible solutions. These specified conditions are not defined as constraints in the traditional sense. They are embedded within the objective function to optimize solutions that satisfy those conditions. This approach allows for more flexibility in the optimization process and enables the algorithm to explore the solution space more effectively.

To evaluate the developed methodology, two design cases are presented. The first design case focuses on optimizing the SRM geometry and improving the average torque and torque ripples. However, the second case study considers not only the SRM torque profile but also the impact of the most influential radial forces' density components acting on the stator.

7.1.1 Case Study I

This case design presents the selected design candidate that was previously discussed in Chapter 5, which utilized the BPNN-based surrogate model to optimize the average torque and minimize torque ripples without considering the effect of radial forces. Table 7.1 presents the optimal stator and rotor pole arc angles and their corresponding average torque and torque ripples. The average torque is improved by 1.8% as compared to the baseline design, while the torque ripples are reduced by 23.8%. The total torque of the case design relative to the baseline is illustrated in Fig. 7.1, a result previously introduced in Chapter 5. In this optimization, the BPNN-based surrogate model effectively enhances torque characteristics and minimizes torque ripples, resulting in notable improvements over the baseline design.

To address radial forces reduction, we calculated the radial forces density components for this design candidate, as depicted in Fig. 7.2. A comparison of the most significant components of radial forces density between this case design and the baseline design is presented in Table 7.1. Notably, the optimization process that solely focused on enhancing torque characteristics without considering radial forces resulted in an unintended 5% increase in the radial forces compared to the baseline design. This finding underscores the importance of adopting a multi-objective approach in SRM design, where the optimization process should consider not only torque characteristics but also the effects on radial forces harmonics.

Table 7. 1. The SRM pole arc angles and performance objectives of case study I and baseline designs.

Design Objectives	Baseline	Design Case I	Improvement
β_s [°]	9.5	9.00	--
β_r [°]	9.3	10.7273	--
Average torque [Nm]	4.88	4.9865	**(+) 2.2%**
Torque ripples [Nm]	0.398	0.3032	**(-) 23.8%**
Radial force density $F_d(u=14, v=2)$ (N/m^2)	32310	33945	**(+) 5%**
Radial force density $F_d(u=14, v=4)$ (N/m^2)	28646	30256	**(+) 5.62%**

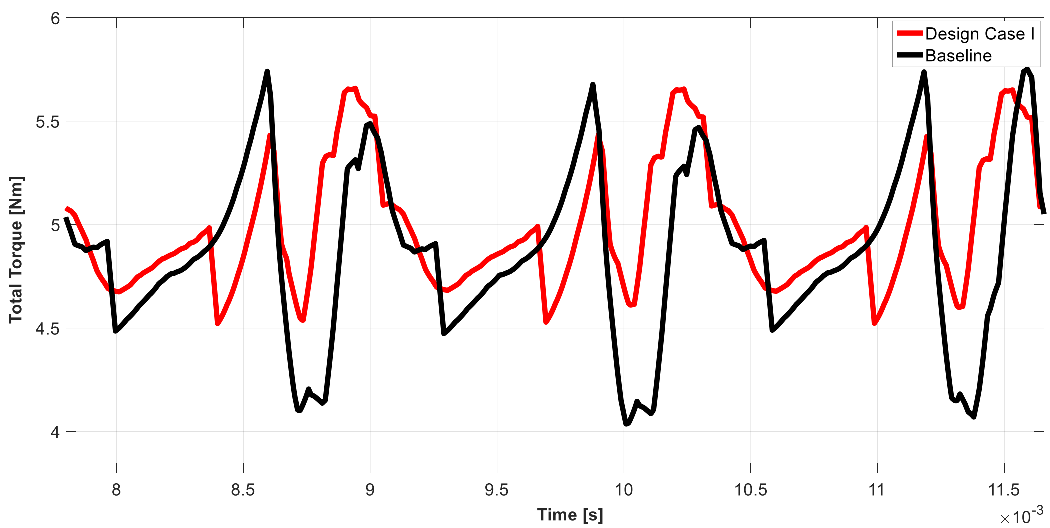

Fig. 7. 1. The total torque comparison between design case I and baseline design for the third electrical cycle (zoomed version of Fig. 5.9).

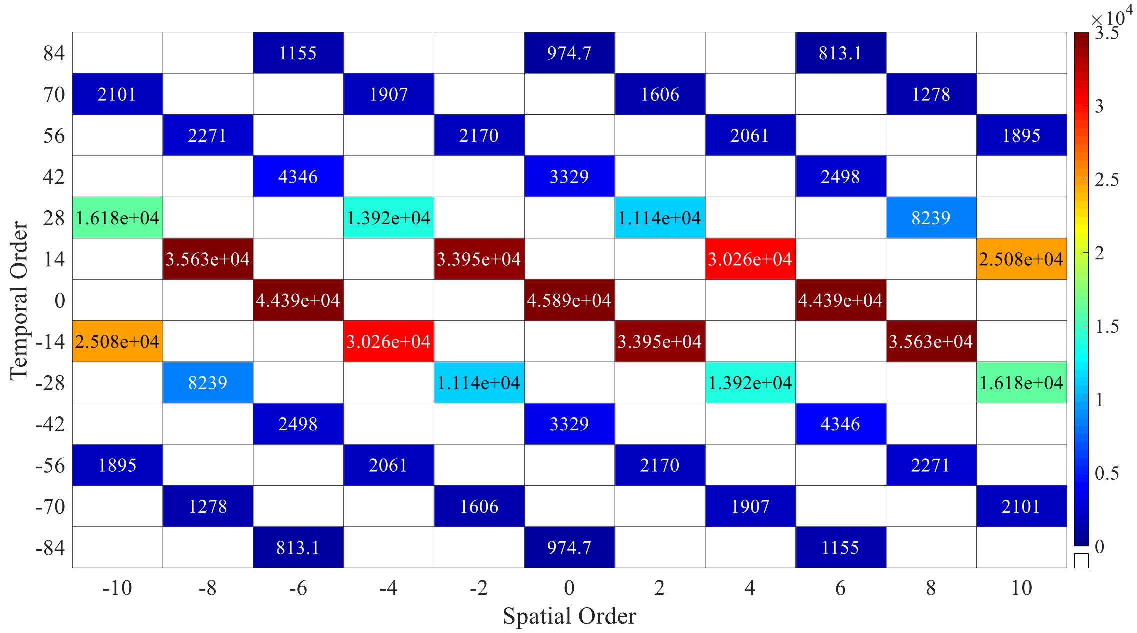

Fig. 7. 2. The dominant radial force density components for the 6/14 SRM design case I.

7.1.2 Case Study II

In this case, the GA utilized a combination of the two developed BPNN-based surrogate models to optimize the pole arc angles. The optimization focused on minimizing torque ripples while simultaneously improving radial force harmonics without decreasing average torque. Design conditions were set based on the values of the design objectives for the baseline design. Table 7.2 presents the optimal values of stator and rotor pole arc angles alongside their corresponding average torque, torque ripples, and dominant radial forces density for case study II. The torque ripple was significantly reduced by 18.84% as compared to the baseline design. Moreover, the radial force density harmonics at the 2nd and 4th circumferential orders decreased by 0.24% and 1.6%, respectively. Meanwhile, the average torque was almost maintained at the baseline design value, with a slight improvement of 0.2%. This design candidate represents the optimal design for this motor, as discussed in the subsequent section. Fig. 7.3 illustrates the total torque of the optimal design relative to the baseline design for one electrical cycle. Additionally, Fig. 7.4 displays the radial forces density components for design case II.

The proposed methodology specifically targeted the reduction of two radial force harmonic amplitudes. However, as illustrated in Fig. 7.4, the optimization process decreased the amplitudes of nearly all harmonic components compared to the baseline design. It is worth mentioning that the results presented in Table 7.1 and Table 7.2 reflect the actual performance of the motor. After the optimization algorithm predicts the optimal motor performance, the corresponding pole arc angles have been fed into the FEA to obtain the actual outputs of the SRM. Similarly, Figs 7.1, 7.2, 7.3, and 7.4 show the outputs from the actual FEA and Simulink models, representing the actual performance of the motor.

Table 7. 2. The SRM pole arc angles and performance objectives of case study II and baseline designs.

Design Objectives	Baseline	Design Case II	Improvement
β_s [°]	9.5	9.7432	--
β_r [°]	9.3	9.00	--
Average torque [Nm]	4.8801	4.8894	**(+) 0.2%**
Torque ripples [Nm]	0.398	0.3235	**(-) 18.84%**
Radial force density $F_d(u=14, v=2)$ (N/m^2)	32310	32232	**(-) 0.24%**
Radial force density $F_d(u=14, v=4)$ (N/m^2)	28646	28194	**(-) 1.6%**

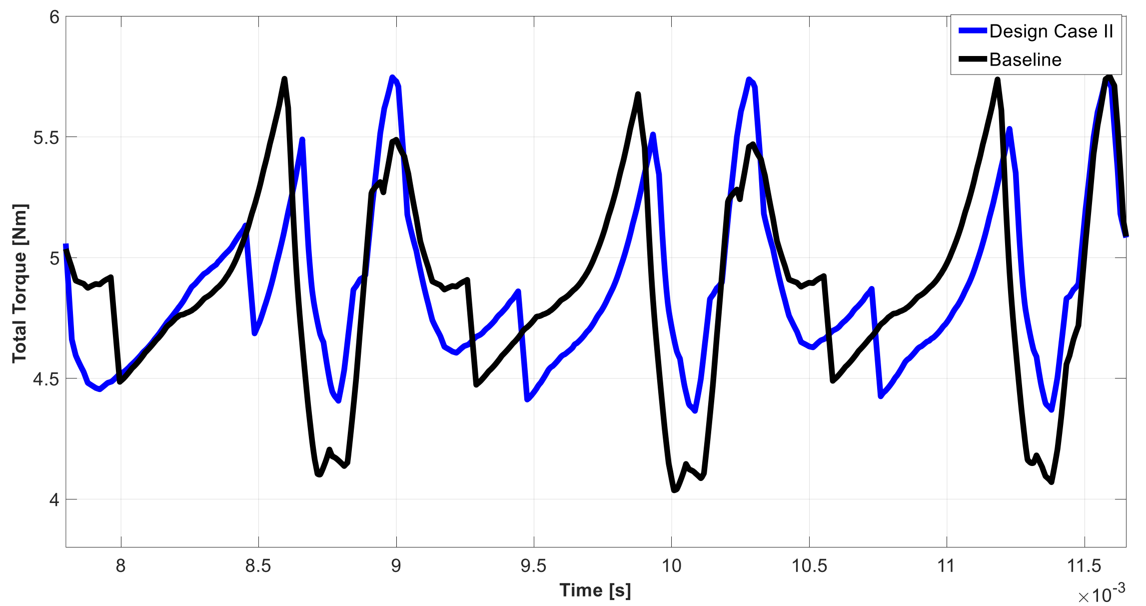

Fig. 7. 3. The total torque comparison between design case II and baseline design for a complete electrical cycle.

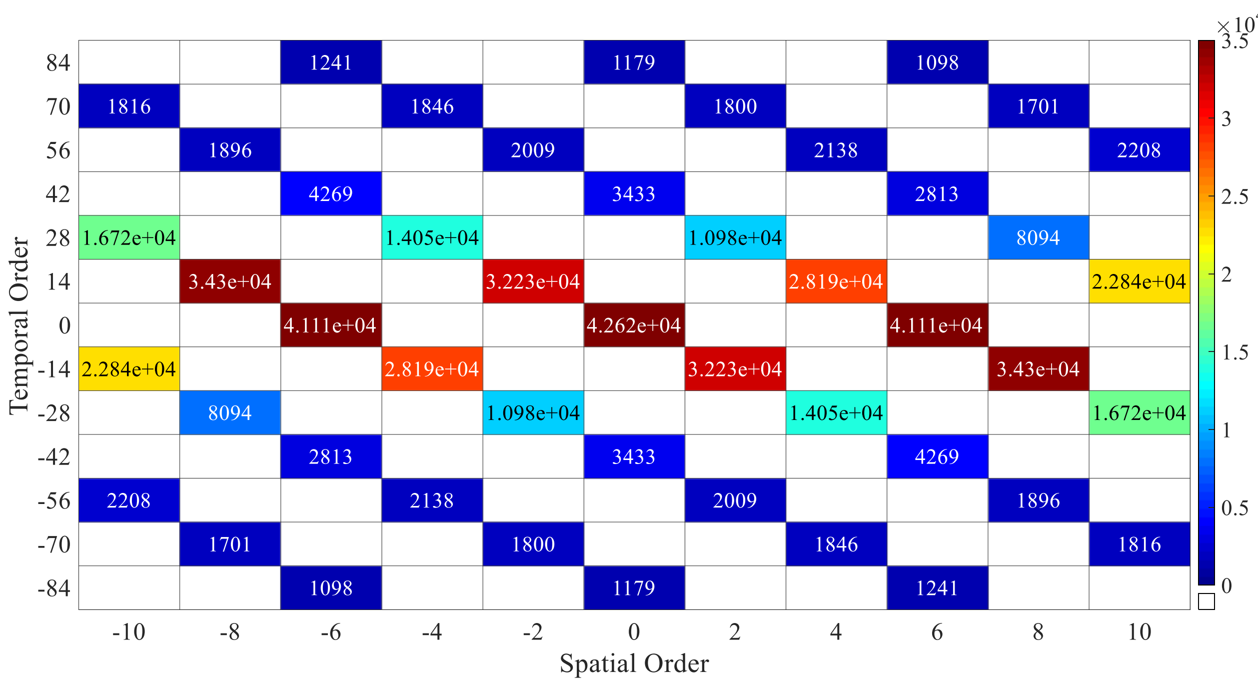

Fig. 7. 4. The dominant radial force density components for the 6/14 SRM design case II.

The proposed methodology, utilizing the GA, achieved the optimal design after 4650 evaluations, illustrating the number of design candidates required to identify the optimal solution. Evaluating these points using FEA and MATLAB demands a prohibitive amount of time, as obtaining a single point (including the values of the average torque, torque ripples, and radial force harmonic components) typically takes about 53 minutes. In contrast, the proposed algorithm required a total of 2655 minutes, which includes both the time to generate the 50-point training dataset and the GA execution time. As a result, the algorithm is approximately 93 times faster than the traditional method, significantly reducing the computational overhead.

7.2 Discussion

To improve the radial forces density alongside the torque profile, it is crucial to understand the highly nonlinear relationship between input and output design objectives. Achieving accurate relationships demands thousands of design points. However, using conventional simulation approaches such as FEA for this purpose is unreasonable, often taking dozens of days. In contrast, the developed BPNN-based surrogate models effortlessly establish the mapping between input and output design parameters within a few minutes. These accurate surrogate models were utilized to map the design parameters in the following graphical representation, providing insights for a multi-objective framework. Fig. 7.5 displays the average torque at different values for the stator and rotor pole arc angles, while Fig. 7.6 and Fig. 7.7 depict the torque ripples and radial forces density harmonics at $u = 14, v = 2$.

Increasing the pole arc angles boosts the average torque. However, torque ripples exhibit highly nonlinear behavior with changes in the pole arc angles, as shown in Fig. 7.6. Regarding radial forces, the data trend suggests a nearly proportional increase with expanding pole arc angles. This indicates that enhancing average torque would also raise radial force density, creating a trade-off between average torque improvement and radial force reduction. Such a scenario poses a challenge to our primary goal of multi-objective design optimization. Nonetheless, there is still room for improvement in these design objectives due to the high nonlinearity in torque ripples. These observations confirm the outcomes of design case II and affirm that this design candidate is optimal for this motor according to the predefined objectives and constraints.

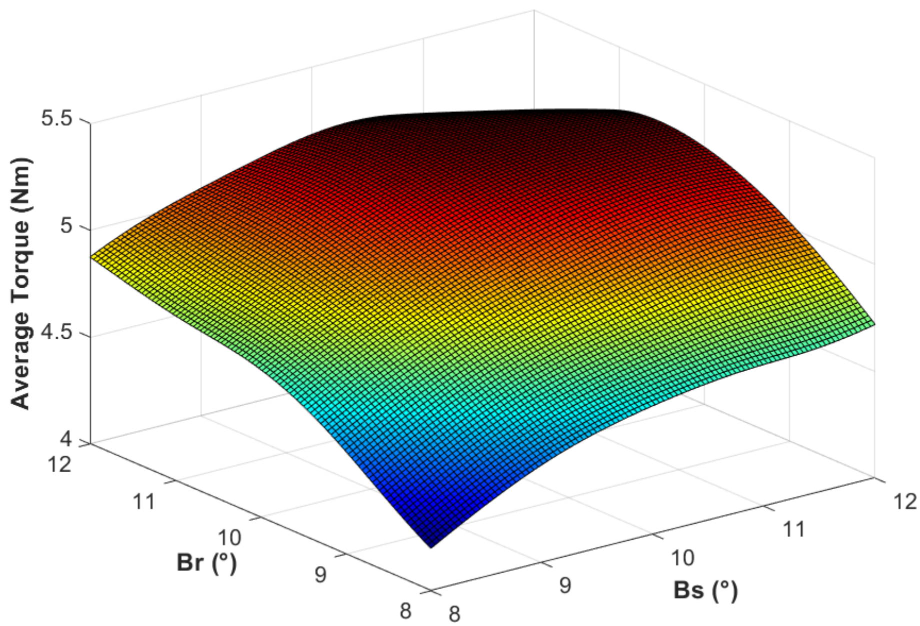

Fig. 7. 5. The average torque of the 6/14 SRM at various stator and rotor pole arc angles

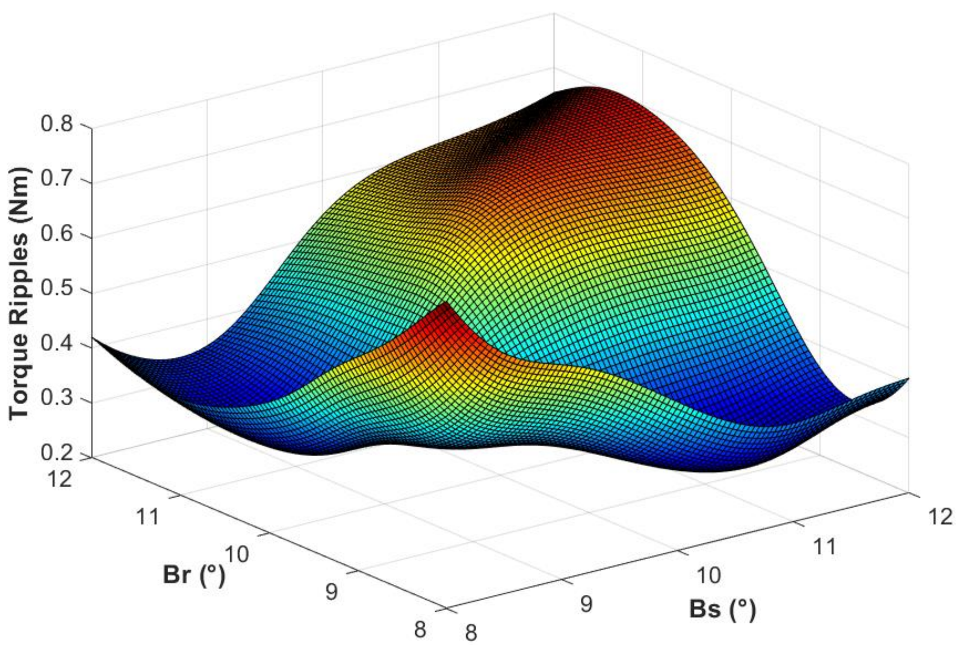

Fig. 7. 6. The torque ripples of the 6/14 SRM for various stator and rotor pole arc angles.

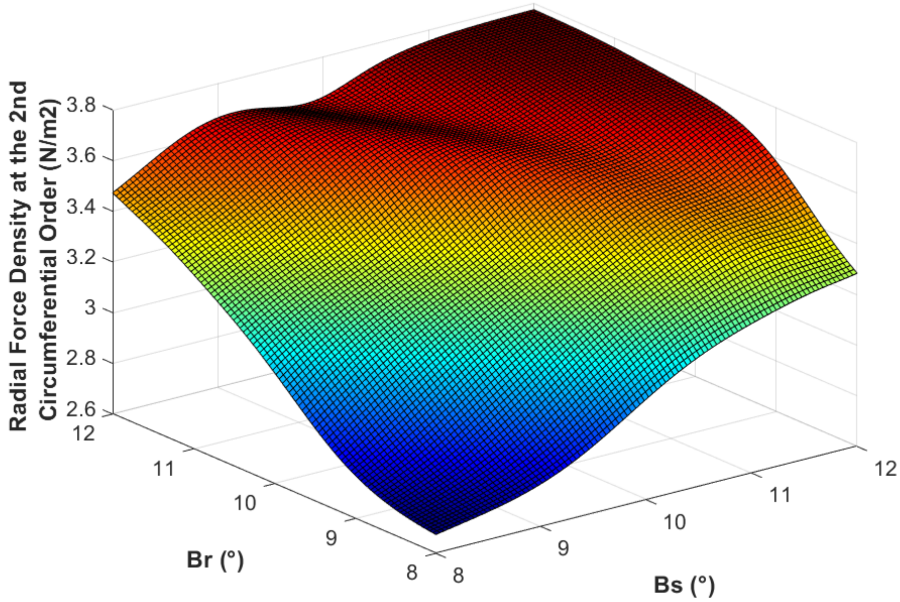

Fig. 7. 7. The radial force density at the 2nd circumferential order of 6/14 SRM for various stator and rotor pole arc angles.

7.3 Summary

This Chapter presented a novel approach utilizing MLAs for multi-objective design optimization of SRMs. The proposed methodology includes two surrogate models. The first model employs a BPNN-based surrogate model to replicate SRM static and dynamic characteristics, establishing relationships between pole arc angles and average torque and torque ripples. Dynamic modeling incorporates optimization of conduction angles, enhancing torque profile. The second BPNN-based surrogate model captures significant radial force density components. GA leverages these surrogate models to predict new geometrical parameters, improving the SRM torque profile and reducing radial forces components. The developed framework was applied to optimize a 6/14 SRM, providing correlations between its pole arc angles and defined design objectives. Since the correlations showed that improving average torque was accompanied by an increase in radial force density components, design constraints prioritized reducing of torque ripples and radial forces without reducing average torque. The optimal design significantly reduced torque ripples by 18% and the most influential radial force density components by around 2% while increasing the average torque by 0.2% compared to the baseline design. This approach significantly reduced computational time compared to traditional FEA and Simulink modeling methods.

Chapter 8

Conclusions and Future Work

8.1 Conclusion

This thesis explored the application of machine learning algorithms (MLAs) in the modeling and geometry design optimization of switched reluctance motors (SRMs), demonstrating the potential of MLAs to enhance the design process, improve performance metrics, and reduce computational costs. The research began with a foundational review of existing machine learning techniques used in SRM modeling and design optimization. Supervised learning algorithms, particularly feedforward neural networks, were identified as dominant in the field. The importance of data quality and size, along with effective training algorithms, was emphasized. The Levenberg-Marquardt algorithm emerged as a superior method for training neural networks, offering both speed and accuracy.

Building on this foundation, various MLAs were developed to map SRM stator and rotor pole arc angles and their dynamic performance (average torque and torque ripples). A comparative analysis of backpropagation neural networks (BPNN), general regression neural networks (GRNN), radial basis function neural networks (RBFNN), and conventional regression fitting algorithms was conducted. BPNN demonstrated remarkable accuracy in predicting new data, establishing its reliability for dynamic performance mapping. A non-conventional optimization approach utilizing BPNN was then proposed to map crucial SRM geometrical parameters and their dynamic performance. This approach provided an efficient surrogate model for the static and dynamic characteristics of the 6/14 SRM, considering the optimization of conduction angles. The training process was optimized by implementing the Levenberg-Marquardt algorithm, leading to efficient convergence and reduced network complexity.

The study also addressed the challenge of radial forces in SRMs with inner rotor configurations, which can lead to acoustic noise and vibration. This work presented a new approach utilizing a BPNN-based surrogate model developed to replace repetitive and computationally intensive simulation procedures. This surrogate model estimated the amplitudes of dominant radial force harmonic components, which were then used in multi-objective optimization to enhance overall SRM performance.

Finally, the thesis presented a novel MLA-based approach for multi-objective design optimization of SRMs, integrating two BPNN-based surrogate models with a genetic algorithm (GA) to predict new geometrical parameters. The optimization framework significantly reduced torque ripples and radial forces while slightly increasing average torque. These results were achieved with reduced computational effort compared to traditional methods, demonstrating that MLAs, particularly neural networks, offer substantial benefits in SRM modeling and optimization. This research paves the way for further exploration and application of MLAs in electric motor design, contributing to the development of more efficient and reliable electric motor designs for various modern technology and industry applications.

8.2 Future Work

The present study focused on optimizing the stator and rotor pole arc angles as the primary geometrical parameters for enhancing the performance of SRMs. However, future research endeavors could explore the optimization of additional geometrical parameters, such as pole heights and taper angles, to further refine the motor design and potentially enhance its performance. Furthermore, the proposed optimization approach can be extended to other SRM configurations and motor types, broadening its applicability and impact.

To validate the optimized design candidates and verify the simulation results, future work will include experimental verification through prototyping of the optimal design candidate. This will involve constructing the asymmetric bridge converter to drive the designed motor.

The present study focused on demonstrating the proposed optimization algorithm's capability to target and reduce specific radial force harmonic components. However, the optimization was not directly based on acoustic noise analysis. As a future endeavor, a comprehensive acoustic and vibration analysis of the machine will be conducted. This analysis will enable the identification of the critical radial force density harmonics that contribute significantly to the acoustic noise and vibration levels. Subsequently, the proposed optimization algorithm will be employed to minimize the amplitudes of these critical components, thereby mitigating the adverse effects of acoustic noise and vibration on the SRM's performance and operation.

This research focused on developing shallow neural network architectures, such as the BPNN and RBFNN, for modeling the static and dynamic torque characteristics of SRMs. While these architectures demonstrated promising results, future endeavors will explore the potential of deep learning techniques, specifically convolutional neural networks (CNNs), for further performance enhancement. CNNs have the capability to handle many input features and establish highly accurate correlations with output objectives. This enables designers to incorporate additional geometrical parameters, such as pole heights and taper angles. Additionally, CNNs will be investigated as surrogate models for predicting the dominant radial force harmonic components. The developed CNN-based surrogate models can then be integrated into a multi-objective optimization framework, simultaneously optimizing torque profile, radial force harmonics, and other performance metrics, leading to enhanced overall SRM performance.

8.3 Publications

8.3.1 Journal Papers

1. **M. Omar**, E. Sayed, M. Abdalmagid, B. Bilgin, M. H. Bakr, and A. Emadi, "Review of machine learning applications to the modeling and design optimization of switched reluctance motors," *IEEE Access*, vol. 10, pp. 130444 – 130468, Dec. 2022.
2. **M. Omar**, M. H. Bakr, and A. Emadi, "Advanced design optimization of switched reluctance motors for torque improvement using supervised learning algorithm," *IEEE Access,* vol. 11, pp. 122057-122068, Nov. 2023
3. **M. Omar**, M. Abdalmagid, M. H. Bakr, and A. Emadi, "Machine learning algorithms for a multi-objective design optimization of switched reluctance motors," *IEEE Transactions on Energy Conversion,* (under review).
4. Y. Asham, **M. Omar**, M. H. Bakr, and A. Emadi, " Design optimization of switched reluctance motors using convolutional neural networks and generative adversarial networks," *IEEE Open Journal of Industry Applications,* (under review).

8.3.2 Conference Papers

1. O. Zayed, **M. Omar**, M. Bakr, M. Narimani, A. Emadi, and B. Bilgin, "Switched reluctance motor design for an EV propulsion application," *in Proc. 47th Annu. Conf. IEEE Ind. Electron. Soc.,* Toronto, ON, Canada, Nov. 2021, pp. 1-6.

2. **M. Omar**, M. H. Bakr, and A. Emadi, “Switched reluctance motor design optimization: a framework for effective machine learning algorithm selection and evaluation,” *in Proc. IEEE Transp. Electrif. Conf. & Expo*, Rosemont, IL, USA, Jun. 2024, pp 1-6.
3. M. Hefny, A. Zaghlol, K. Vaghasiya, R. Pradhana, **M. Omar**, and A. Emadi, “Holistic thermal management system design, testing and modeling for 300 kw IGBT-based inverter for switched reluctance motor drives,” *in Proc. Therminic*, Toulouse, France, Sept. 2024.
4. **M. Omar**, Y. Asham, M. H. Bakr, and A. Emadi, " Comparative analysis of BPNN and CNN for optimizing switched reluctance motor geometry design," To be published.

References

[1] B. Bilgin, J. W. Jiang, and A. Emadi, Switched Reluctance Motor Drives: Fundamentals to Applications. Boca Raton, FL, USA: CRC Press, 2019, ISBN: 9878-1138304598.

[2] R. Vandana, and B. G. Fernandes, ‘‘Design methodology for high performance segmented rotor switched reluctance motors,” *IEEE Trans. Energy Convers.*, vol. 30, no. 1, pp. 11–21, Mar. 2015.

[3] M. Abdalmagid, E. Sayed, M. H. Bakr, and A. Emadi, "Geometry and topology optimization of switched reluctance machines: a review," *IEEE Access*, vol. 10, pp. 5141-5170, Jan. 2022.

[4] S. I. Cosman, V. I. Boanca, C. Oprea, and C. S. Martis, “Design, building and testing of a low voltage-high current drive for SRMs used for HVAC applications,” in *Proc. International Conference and Exposition on Electrical and Power Engineering (EPE)*, Iasi, Romania, Oct. 2018, pp. 58-62.

[5] H. Shin, and K. Lee, “Optimal design of a 1 kW switched reluctance generator for wind power systems using a genetic algorithm,” *IET Electr. Power Appl.*, vol. 10, no. 8, pp. 807–817, Sep. 2016.

[6] B. Bilgin, P. Magne, P. Malysz, Y. Yang, V. Pantelic, M. Preindl, A. Korobkine, W. Jiang, M. Lawford, and A. Emadi, "Making the case for electrified transportation," *IEEE Trans. Transp. Electr.,* vol. 1, no. 1, pp. 4-17, Jun. 2015.

[7] H. Zhang, W. Xu, S. Wang, Y. Huangfu, G. Wang, and J. Zhu, "Optimum design of rotor for high-speed switched reluctance motor using level set method," *IEEE Trans. Magn.*, vol. 50, no. 2, pp. 765–768, Feb. 2014.

[8] J. Liang, A. D. Callegaro, B. Bilgin, and A. Emadi, "A novel three-dimensional analytical approach for acoustic noise modeling in switched reluctance machines," *IEEE Trans. Energy Convers.*, vol. 36, no. 3, pp. 2099–2109, Sep. 2021.

[9] O. Zayed, M. Omar, M. Bakr, M. Narimani, A. Emadi, and B. Bilgin, "Switched reluctance motor design for an EV propulsion application," in *Proc. 47th Annu. Conf. IEEE Ind. Electron. Soc.*, Toronto, ON, Canada, Nov. 2021, pp. 1-6.

[10] E. Sayed, "Adjoint-based optimization of switched reluctance motors," Ph.D. dissertation, Dept. Elect. Comp. Eng., McMaster Univ., Hamilton, ON, Canada, 2019.

[11] H. Dhulipati, E. Ghosh, S. Mukundan, P. Korta, J. Tjong, and N. C. Kar, ‘‘Advanced design optimization technique for torque profile improvement in six-phase PMSM using supervised machine learning for direct drive EV,’’ *IEEE Trans. Energy Convers.,* vol. 34, no. 4, pp. 2041–2051, Dec. 2019.

[12] P. Zhang, G. Sizov, D. M. Ionel, and N. Demerdash, "Design optimization of spoke-type ferrite magnet machines by combined design of experiments and differential

evolution algorithms," in *Proc. IEEE Int. Elect. Mach. Drives Conf.*, Chicago, IL, USA, July 2013, pp. 958–964.

[13] M. Omar, E. Sayed, M. Abdalmagid, B. Bilgin, M. H. Bakr, and A. Emadi, "Review of machine learning applications to the modeling and design optimization of switched reluctance motors," *IEEE Access*, vol. 10, pp. 130444 – 130468, Dec. 2022.

[14] H. Sahraoui, H. Zeroug, and H. A. Toliyat, "Switched reluctance motor design using neural-network method with static finite-element simulation," *IEEE Trans. on Magn.*, vol. 43, no. 12, pp. 4089-4095, Dec. 2007.

[15] Z. Zhang, S. Rao, and X. Zhang, "Performance prediction of switched reluctance motor using improved generalized regression neural networks for design optimization," *Trans. on Electr. Mach. and Syst.*, vol. 2, no. 4, pp. 371-376, Dec. 2018.

[16] J. W. Jiang, B. Bilgin, and A. Emadi, "Three-phase 24/16 switched reluctance machine for a hybrid electric powertrain," *IEEE Trans. Transp. Electrif.*, vol. 3, no. 1, pp. 76-85, Mar. 2017.

[17] E. Sayed, M. Abdalmagid, G. Pietrini, N. Sa'adeh, A. D. Callegaro, C. Goldstein, and A. Emadi, "Review of electric machines in more/hybrid/turbo electric aircraft," *IEEE Trans. on Transp. Electrif.*, vol. 7, no. 4, pp. 2976-3005, Dec. 2021.

[18] J. K. NΦland, M. Leandro, J. A. Suul, and M. Molinas, "High-power machines and starter-generator topologies for more electric aircraft: a technology outlook," *IEEE Access*, vol. 8, pp. 130104–130123, July 2020.

[19] J. D. Widmer, R. Martin, and B. C. Mecrow, "Optimization of an 80-kw segmental rotor switched reluctance machine for automotive traction," *IEEE Trans. Ind. App.*, vol. 51, no. 4, pp. 2990–2999, 2015.

[20] B. Bilgin, A. Emadi, and M. Krishnamurthy, "Design considerations for switched reluctance machines with a higher number of rotor poles," *IEEE Trans. Ind. Electron.*, vol. 59, no. 10, pp. 3745– 3756, 2012.

[21] J. B. Bartolo, M. Degano, J. Espina, and C. Gerada, "Design and initial testing of a high-speed 45-kw switched reluctance drive for aerospace application," *IEEE Trans. Ind. Electron.*, vol. 64, no. 2, pp. 988–997, Feb. 2017.

[22] B. Bilgin, B. Howey, A. D. Callegaro, J. Liang, M. Kordic, J. Taylor, and A. Emadi, "Making the case for switched reluctance motors for propulsion applications," *IEEE Trans. Veh. Technol.*, vol. 69, no. 7, pp. 7172–7186, 2020.

[23] G. Watthewaduge, E. Sayed, A. Emadi, and B. Bilgin, "Electromagnetic modeling techniques for switched reluctance machines: state-of-the-art review," *IEEE Open J. Ind. Electron. Soc.*, vol. 1, pp. 218-234, 2020.

[24] S. Li, S. Zhang, T. G. Habetler, and R. G. Harley, "Modeling, design optimization, and applications of switched reluctance machines – A review," *IEEE Trans. Ind. Appl.*, vol. 55, no. 3, pp. 2660–2681, June 2019.

[25] P. Chancharoensook and M. F. Rahman, "Dynamic modeling of a four-phase 8/6 switched reluctance motor using current and torque look-up tables", *in proc. IEEE Annual Conference of the Industrial Electronics Society (IECON),* Sevilla, Spain, No. 2002, pp. 491-496.

[26] R. D. Doncker, D. W. J. Pulle, and A. Veltman, Advanced Electrical Drives: Analysis, Modeling, Control, Springer, 2011. ISBN: 9789400701816.

[27] S. Wang, B. Burton, and R. G. Harley, "Switched reluctance motor measurements and simulation models," *in proc. IEEE Africon Conference in Africa*, Gaborone, Botswana, Sep. 2004, pp. 1161-1167

[28] S. Woothipatanapan,, P. Chancharoensook, A. Jangwanitlert, "An Improved Asymmetric Half-Bridge Converter for Switched Reluctance Motor in Low-Speed Operation with Current Regulated Mode," *Journal of Power Electronics,* vol. 15, no.6, pp. 1533-1546, Nov. 2015

[29] A. L. Saleh, F. Al-Amyal, L. Számel, "Control techniques of switched reluctance motors in electric vehicle applications: A review on torque ripple reduction strategies," *AIMS Electronics and Electrical Engineering*, vol. 8, no. 1, pp. 104-145, 2024.

[30] L. Maharjan, E. Bostanci, S. Wang, E. Cosoroaba, W. Cai, F. Yi, P. Shamsi, W. Wang, L. Gu, M. Luo, N. A. Rahman, M. McDonough, C. Lin, J. Hearron, C. C. Narvaez, M. Wu, A. H. Isfahani, Y. Li, G. Rao, M. Moallem, P. T. Balsara, and B. Fahimi, "Comprehensive report on design and development of a 100-kW DSSRM," *IEEE Trans. Transp. Electrific.*, vol. 4, no. 4, pp. 835–856, Dec. 2018.

[31] C. Gan, J. Wu, Q. Sun, W. Kong, H. Li, and Y. Hu, "A review on machine topologies and control techniques for low-noise switched reluctance motors in electric vehicle applications," *IEEE Access*, vol. 6, pp. 31430–31443, May 2018.

[32] P. C. Kjaer, J. J. Gribble, and T. J. E.Miller, “Dynamic testing of switched reluctance motors for high-bandwidth actuator applications,” *IEEE/ASME Trans. Mechatronics,* vol. 2, no. 2, pp. 123–135, Jun. 1997.

[33] Z. Rahman, M. Ehsani, and K. L. Butler, “An investigation of electric motor drive characteristics for EV and HEV propulsion systems,” *Future Transp. Techno. Conf. & Exposition,* SAE 2000-01-3062, Costa Mesa, California, Aug. 2000.

[34] B. Bilgin, J. Liang, M. V. Terzic, J. Dong, R. Rodriguez, E. Trickett, and A. Emadi, “Modeling and analysis of electric motors: state-of-the-art review,” *IEEE Trans. Transp. Electrific.,* vol. 5, no. 3, pp. 602-617, Sep. 2019.

[35] Y. Duan, and D. M. Ionel, “A Review of recent developments in electrical machine design optimization methods with a permanent-magnet synchronous motor benchmark study,” *IEEE Trans. Ind. Appl.* vol. 49, no. 3, pp. 1268-1275, May 2013.

[36] J. Song, F. Dong, J. Zhao, H. Wang, Z. He, and L. Wang, “An efficient multiobjective design optimization method for a PMSLM based on an extreme learning machine,” *IEEE Trans. Ind. Electron.,* vol. 66, no. 2, pp. 1001-1011, Feb. 2019.

[37] S. R. Mousavi-Aghdam, M. R. Feyzi, N. Bianchi, and M. Morandin, “Design and analysis of a novel high-torque stator-segmented SRM,” *IEEE Trans. Ind. Electron.,* vol. 63, no. 3, pp. 1458–1466, Mar. 2015.

[38] M. J. Kamper, S. W. Rasmeni, and R. J. Wang, “Finite-element time-step simulation of the switched reluctance machine drive under single pulse mode operation,” *IEEE Trans. Magn.,* vol. 43, no. 7, pp. 3202–3208, July 2007.

[39] E. Afjei, A. Siadatan, and H. Torkaman, "Magnetic modeling, prototyping, and comparative study of a quintuple-set switched reluctance motor," *IEEE Trans. Magn.*, vol. 51, no. 8, pp. 1-7, 2015.

[40] G. Lei, C. Liu, J. Zhu, and Y. Guo, "Techniques for multilevel design optimization of permanent magnet motors," *IEEE Trans. Energy Convert.*, vol. 30, no. 4, pp. 1574–1584, Dec. 2015.

[41] O. Ustun, "Measurement and real-time modeling of inductance and flux linkage in switched reluctance motors," *IEEE Trans. Magn.*, vol. 45, no. 12, pp. 5376-5382, 2009.

[42] A. Khalil, and I. Husain, "A Fourier series generalized geometry based analytical model of switched reluctance machines," *IEEE Trans. Ind. Appl.*, vol. 43, no. 3, pp. 673–684, May/June. 2007.

[43] V. P. Vujicic, "Modeling of a switched reluctance machine based on the invertible torque function," *IEEE Trans. Magn.*, vol. 44, no. 9, pp.2186-2194, 2008.

[44] M. Yilmaz, and P. T. Krein, "Capabilities of finite element analysis and magnetic equivalent circuits for electrical machine analysis and design," in *Proc. IEEE Power Electron. Spec. Conf.*, Rhodes, Greece, Jun. 2008, pp. 4027–4033.

[45] Y. Zhang, K. Chau, J. Jiang, D. Zhang, and C. Liu, "A finite element– analytical method for electromagnetic field analysis of electric machines with free rotation," *IEEE Trans. Magn.*, vol. 42, no. 10, pp. 3392–3394, Oct. 2006.

[46] K. Hameyer, and R. Belmans, Numerical Modelling and Design of Electrical Machines and Devices. Southampton, Boston: WIT Press, vol. 1, 1999.

[47] N. Bianchi, Electrical Machine Analysis Using Finite Elements. Boca Raton, FL, USA: CRC Press, 2005.

[48] H. P. Chi, R. L. Lin, and J. F. Chen, “Simplified flux linkage model for switched reluctance motors,” *IEE Proc. Elect. Power Appl.*, vol. 152, no. 3, pp. 577–583, Mar. 2005.

[49] G. Watthewaduge, E. Sayed, A. Emadi, and B. Bilgin, "Electromagnetic modeling techniques for switched reluctance machines: state-of-the-art review," *IEEE Open J. Ind. Electron.* Soc., vol. 1, pp. 218-234, 2020.

[50] T. C. O’Connell, and P. T. Krein, “A time-harmonic three-dimensional vector boundary element model for electromechanical devices,” *IEEE Trans. Energy Convers.*, vol. 25, no. 3, pp. 606–618, Sep. 2010.

[51] D. M. Araujo, J.-L. Coulomb, O. Chadebec, and L. Rondot, “A hybrid boundary element method-reluctance network method for open boundary 3-D nonlinear problems,” *IEEE Trans. Magn.*, vol. 50, no. 2, pp. 77–80, Feb. 2014.

[52] D. Wang, D. Zhang, X. Du, and X. Wang, “Unitized design methodology of linear switched reluctance motor with segmental secondary for long rail propulsion application,” *IEEE Trans. Ind. Electron.*, vol. 65, no. 12, pp. 9884–9894, Dec. 2018.

[53] W. Uddin, T. Husain, Y. Sozer, and I. Husain, “Design methodology of a switched reluctance machine for off-road vehicle applications,” *IEEE Trans. Ind. Appl.*, vol. 52, no. 3, pp. 2138–2147, June 2016.

[54] Z. Zhihui and L. Yuren, "Numerical and analytical modeling of switched reluctance machines," *J. Comput.*, vol. 7, no. 12, pp. 3036–3043, Dec. 2012.

[55] Y. Yang and A. Emadi, "Coupled switched reluctance machine modeling and simulations," in *Proc. IEEE Conf. Exp. Transp. Electrific. Asia-Pacific (ITEC Asia-Pacific)*, Beijing, China, Sep. 2014, pp. 1–6.

[56] X. -D. Xue, K. W. E. Cheng, and S. L. Ho, "Simulation of switched reluctance motor drives using two-dimensional bicubic spline," *IEEE Trans. Energy Convers*., vol. 17, no. 4, pp. 471–477, Dec. 2002.

[57] J. M. Stephenson, and J. Corda, "Computation of torque and current in doubly salient reluctance motors from nonlinear magnetization data," in *Proc. Inst. Elect. Eng.*, vol. 126, no. 5, pp. 393–396, May 1979.

[58] W. Lu, A. Keyhani, and A. Fardoun, "Neural network-based modeling and parameter identification of switched reluctance motors," *IEEE Trans. Energy Convers*., vol. 18, no. 2, pp. 284-290, June 2003.

[59] M. Mohri, A. Rostamizadeh, and A. Talwalkar, Foundations of Machine Learning. 2nd ed., Cambridge, MA, USA: MIT Press, 2018.

[60] Christopher M. Bishop, Pattern Recognition and Machine Learning. NY, USA: Springer, 2006.

[61] R. S. Sutton, and A.G. Barto, Reinforcement Learning: An Introduction. Boston, USA: MIT Press, 1998.

[62] I. Goodfellow, Y. Bengio, and A. Courville, Deep Learning. Cambridge, MA, USA: MIT Press, 2016.

[63] M. Bakr, Nonlinear Optimization in Electrical Engineering with Applications in MATLAB. London, UK: Institution of Engineering and Technology, 2013.

[64] C. Harpham, C.W. Dawson, and M.R. Brown, "A review of genetic algorithms applied to training radial basis function networks," *Neural Comp. & App.*, pp. 193–201, Apr. 2004.

[65] Y. Cai, Y. Wang, H. Xu, S. Sun, C. Wang, and L. Sun, "Research on rotor position model for switched reluctance motor using neural network," *IEEE/ASME Trans. Mechatron.*, vol. 23, no. 6, pp. 2762-2773, Dec. 2018.

[66] Y. Cai, and C. Gao, "Nonlinear modeling of switched reluctance motor based on bp neural network," in *Proc. Third Intern. Conf. Natural Computation,* Haikou, China, Nov. 2007, pp. 232-236.

[67] T. Lachman, T.R. Mohamad, and C.H. Fong, "Nonlinear modelling of switched reluctance motors using artificial intelligence techniques" *IEE Proc. Electric Power App.*, vol. 151, no. 1, pp. 53 – 6, Jan. 2004.

[68] Z. Zhihui, and L. Yuren, "Modeling and simulation of switched reluctance machine based aircraft electric brake system by BP neural network," in *proc. 9th IEEE Conf. Ind. Electron. and App.*, Hangzhou, China, June 2014, pp. 338-341.I

[69] E. Mese, and D. A. Torrey, "An approach for sensorless position estimation for switched reluctance motors using artifical neural networks," *IEEE Trans. Power Electron.*, vol. 17, no. 1, pp. 66-75, Jan. 2002.

[70] C. Elmas, S. Sagiroglu, I. Colak, and G. Bal, “Modelling of a nonlinear switched reluctance drive based on artificial neural networks,” in *Proc. Intern. Conf. Power Electron. and Var. Speed Drives,* London, UK, Oct. 1994, pp. 7-12.

[71] S. Qi, and H. Kong, “A modeling method of SRM based on RBF neural networks,” in *proc Intern. Conf. Electron., Comm. and Control (ICECC),* Ningbo, China, Sep. 2011, pp. 44-47.

[72] F. Yang, W. Li, C. Li, and Q. Miao, “State-of-charge estimation of lithium-ion batteries based on gated recurrent neural network,” *Energy,* vol. 175, pp 66-75, May 2019.

[73] IJ Myung, "Tutorial on maximum likelihood estimation," *J. of math. Psych*., vol. 47, pp. 90-100, Feb. 2003.

[74] F. Daldaban, N. Ustkoyuncu, and K. Guney, “Phase inductance estimation for switched reluctance motor using adaptive neuro-fuzzy inference system,” *Energy Convers. and Manag.,* Vol. 47, no. 5, pp 485-493, 2006.

[75] J. Wu, X. Sun, and J. Zhu, “Accurate torque modeling with PSO-based recursive robust LSSVR for a segmented-rotor switched reluctance motor,” *CES Trans. Electric. Mach. and Sys.,* vol. 4, no. 2, pp. 96-104, June 2020.

[76] W. Ding, and D. Liang, “Modeling of a 6/4 switched reluctance motor using adaptive neural fuzzy inference system,” *IEEE Trans Magn.,* vol. 44, no. 7, pp. 1796-1804, July 2008.

[77] C. Cortes, and V. Vapnik, “Support-vector networks,” *Machine Learning,* vol. 20, pp. 273–297, 1995.

[78] M. Li, R. Guo, K. Zhang, Z. Lin, F. Yang, S. Xu, X. Chen, A. Massa, and A. Abubakar, "Machine learning in electromagnetics with applications to biomedical imaging: a review," *IEEE Anten. and Propag. Magazine*, vol. 63, no. 3, pp. 39-51, June 2021.

[79] A. Soualhi, K. Medjaher, and N. Zerhouni, "Bearing health monitoring based on Hilbert–Huang transform, support vector machine, and regression," *IEEE Trans. Instrum. and Meas.*, vol. 64, no. 1, pp. 52–62, Jan. 2015.

[80] M. Kang, J. Kim, J-M. Kim, A. C. C. Tan, E. Y. Kim, and B-K. Choi, "Reliable fault diagnosis for low-speed bearings using individually trained support vector machines with kernel discriminative feature analysis," *IEEE Trans. Power Electron.*, vol. 30, no. 5, pp. 2786– 2797, May 2015.

[81] R. Solera-Urena, A. I. Garcia-Moral, C. Pelaez-Moreno, M. Martinez- Ramon, and F. Diaz-de-Maria, "Real-time robust automatic speech recognition using compact support vector machines," *IEEE Trans. Audio Speech Lang. Process.*, vol. 20, no. 4, pp. 1347–1361, May 2012.

[82] Y.-H. Liu, H.-P. Huang, and C.-H. Weng, "Recognition of electromyographic signals using cascaded kernel learning machine," *IEEE/ASME Trans. Mechatron*., vol. 12, no. 3, pp. 253–264, June 2007.

[83] Q. Ye, Z. Han, J. Jiao, and J. Liu, "Human detection in images via piecewise linear support vector machines," *IEEE Trans. Image Process*., vol. 22, no. 2, pp. 778–789, Feb. 2013.

[84] S. Song, L. Ge, and M. Zhang, "Data-reconstruction-based modeling of SRM with few flux-linkage samples from torque-balanced measurement," *IEEE Trans. Energy Convers.*, vol. 31, no. 2, pp. 424-435, June 2016.

[85] J. A. K. Suykens, and J. Vandewalle, "Least squares support vector machine classifiers," *Neural Process. Letters*, vol. 9, no. 3, pp. 293–300, June 1999.

[86] J. Valyon, and G. Horváth, "Extended least squares LS-SVM," *Intern. J. Comput. Intell.*, vol. 3, pp. 234-242, July 2005.

[87] X. Chunli, S. Cheng, and Z. Dandan, "Parameters optimization of least squares support vector machines and its application," *J. Computers,* vol. 6, no. 9, Aug. 2011.

[88] L. Si, H. Liu, and Z. Liu, "Modeling of switched reluctance motors based on LS-SVM," *Chinese Soc. for Electr. Eng.*, vol. 27, no. 6, pp. 26-30, 2007.

[89] W. Shang, S. Zhao, and Y. Shen, "Application of LSSVM with AGA optimizing parameters to nonlinear modeling of SRM," in *proc. 3rd IEEE Conf on Ind. Electron. and App.*, Singapore, Aug. 2008, pp. 775-780.

[90] H. Likun, Y. Qingxin, and A. Jinlong, "Modeling of SRM based on XS-LSSVR optimized by GDS," *IEEE Trans. Applied Supercond.*, vol. 20, no. 3, pp. 1102-1105, June 2010.

[91] Q. Xiang, Y. Sun, and X. Ji, "Modeling inductance for bearingless switched reluctance motor based on PSO-LSSVM," in *proc. Chinese Control and Decision Conf. (CCDC)*, Mianyang, China, Aug. 2011, pp. 800-803.

[92] R. Zhong, Y. Cao, W. Hua, Y. Xu, and S. Xu, “An improved model of switched reluctance motors based on least square support vector machine,” in *proc. IEEE Intern. Symp. on Ind. Electron.,* Taipei, Taiwan, July 2013, pp. 1-6.

[93] R. Mall, and J. A. K. Suykens, "Very sparse LSSVM reductions for large-scale data," *IEEE Trans. Neural Net. and Learn. Sys.*, vol. 26, no. 5, pp. 1086-1097, May 2015.

[94] G. Si, J. Shi, Z. Guo, L. Jia, and Y. Zhang, "Reconstruct the support vectors to improve LSSVM sparseness for mill load prediction", *Math. Prob. Eng.*, vol. 2017, pp. 12, July 2017.

[95] J. A. K. Suykens, L. Lukas, and J. Vandewalle, “Sparse approximation using least squares support vector machines,” in *Proc. IEEE Int. Symp. Circiuts Sys. (ISCAS)*, Geneva, Switzerland, May 2000, vol. 2, pp. 757–760.

[96] S. Huang, G. Cao, Z. He, J. F. Pan, J. Duan, and Q. Qian, “Nonlinear modeling of the inverse force function for the planar switched reluctance motor using sparse least squares support vector machines,” *IEEE Trans. Ind. Infor*., vol. 11, no. 3, pp. 591-600, June 2015.

[97] J. E. Stephen, S. S. Kumar, and J. Jayakumar, “Nonlinear modeling of a switched reluctance motor using LSSVM – ABC,” *Acta Polytechnica Hungarica*, vol. 11, no. 6, 2014.

[98] D. Karaboga, B. Gorkemli, C. Ozturk, and N. Karaboga, “A comprehensive survey: artificial bee colony (ABC) algorithm and applications,” *Artif. Intell.* Rev. vol. 42, pp. 21–57, 2014.

[99] J. E. Stephen, S. S. Kumar, and J. Jayakumar, "Torque modeling of Switched Reluctance Motor using LSSVM-DE," *Neurocomputing*, vol. 211, pp. 117-128, 2016.

[100] J. W. Bandler Q.S. Cheng, S.A. Dakroury, A.S. Mohamed, M.H. Bakr; K. Madsen, and J. Sondergaard, "Space mapping: the state of the art," *IEEE Trans. Microwave Theory and Techniq.*, vol. 52, no. 1, pp. 337-361, Jan. 2004.

[101] J. Gong, H. Zhang, B. Zhao, D. Fu, and F. Gillon, "Proposal of a biobjective kriging adapted output space mapping technique for electromagnetic design optimization," *IEEE Trans. Magn.*, vol. 55, no. 6, pp. 1–5, June 2019.

[102] M. Li, F. Gabriel, M. Alkadri, and D. A. Lowther, "Kriging-assisted multi-objective design of permanent magnet motor for position sensorless control," *IEEE Trans. Magn.*, vol. 52, no. 3, pp. 1–4, Mar. 2016.

[103] D. F. Specht "A general regression neural network." *IEEE Trans. Neural Net.*, vol. 2, no. 6, pp.568-576, Nov. 1991.

[104] E. Sayed, P. Azer, M. Kordic, J. Reimers, B. Bilgin, M. H. Bakr, and A. Emadi, "Design of a switched reluctance motor for a pump jack application," in *proc. IEEE Electr. Power and Energy Conf. (EPEC)*, Toronto, ON, Canada, Oct. 2018, pp. 1-6.

[105] Z. Zhang, S. Rao, and X. Zhang, "Performance prediction of switched reluctance motor using improved generalized regression neural networks for design optimization," *Trans. Electr. Mach. and Sys.*, vol. 2, no. 4, pp. 371-376, Dec. 2018.

[106] Kasprzak, M., 6/14 switched reluctance machine design for household HVAC system applications, MASc thesis, Department of Mechanical Engineering, McMaster University, Hamilton, Canada, 2016.

[107] Y. Duan and D. M. Ionel, "A review of recent developments in electrical machine design optimization methods with a permanent-magnet synchronous motor benchmark study," *IEEE Trans. Ind. Appl.*, vol. 49, no. 3, pp. 1268–1275, May/Jun. 2013.

[108] B. Howey, B. Bilgin, and A. Emadi, "Design of an external-rotor direct drive e-bike switched reluctance motor," *IEEE Trans. on Vehicular Techno.*, vol. 69, no. 3, pp. 2552–2562, 2020.

[109] S. Katoch, S. S. Chauhan, and V. Kumar, "A review on genetic algorithm: past, present, and future," *Multimed. Tools Appl.*, vol. 80, pp. 8091–8126, 2021.

[110] R. Krishnan, Switched Reluctance Motor Drives Modeling, Simulation, Analysis, Design and Applications. Boca Raton, FL: CRC, 2001.

[111] M. Omar, M. H. Bakr, and A. Emadi, "Advanced design optimization of switched reluctance motors for torque improvement using supervised learning algorithm," *IEEE Access*, vol. 11, pp. 122057-122068, Nov. 2023.

[112] M. Abdalmagid, M. H. Bakr and A. Emadi, "A new technique for radial and tangential force calculation time reduction for the optimization process of SRMs," *IEEE Access*, vol. 11, pp. 66076-66093, 2023.

[113] J. Liang, A. D. Callegaro, B. Howey, B. Bilgin, J. Dong, J. Lin, and A. Emadi, ‘‘Analytical calculation of temporal and circumferential orders of radial force density harmonics in external-rotor and internal-rotor switched reluctance machines,’’ *IEEE Open J. Ind. Appl.,* vol. 2, pp. 70–81, 2021.

[114] N. Zabihi, and R. Gouws, “A review on switched reluctance machines for electric vehicles,” in *Proc. IEEE International Symposium on Industrial Electronics (ISIE),* Santa Clara, CA, June 2016, pp. 799-804.

[115] Y. Hu, C. Gan, W. Cao, J. Zhang, W. Li, and S. J. Finney, “Flexible fault tolerant topology for switched reluctance motor drives,” *IEEE Trans. Power Electron.,* vol. 31, no. 6, pp. 4654–4668, Sep. 2015.

[116] D. E. Cameron, J. H. Lang, and S. D. Umans, “The origin and reduction of acoustic noise in doubly salient variable-reluctance motors,” *IEEE Trans. Ind. Appl.,* vol. 28, no. 6, pp. 1250–1255, Dec. 1992.

[117] O. Gundogmus, M. Elamin, Y. Yasa, T. Husain, Y. Sozer, John Kutz, J. Tylenda, and R. L. Wright, "Acoustic Noise Mitigation of Switched Reluctance Machines With Windows on Stator and Rotor Poles," *IEEE Transactions on Industry Applications*, vol. 56, no. 4, pp. 3719-3730, Aug. 2020.